Bubbles on the cutting edge : direct numerical simulations of gas-liquid-solid three-phase flows

Bubbles on the Cutting Edge

Direct Numerical Simulations of Gas-Liquid-Solid Three-Phase Flows

Bubbles on the Cutting Edge

Direct Numerical Simulations of Gas-Liquid-Solid Three-Phase Flows

Dit proefschrift is goedgekeurd door de promotoren en de samenstelling van de promotiecommissie is als volgt:

voorzitter:	prof.dr.ir. J.C. Schouten	
1^e promotor:	prof.dr.ir. J.A.M. Kuipers	
copromotor(en):	dr.ir. N.G. Deen	
leden:	prof.dr. R.F. Mudde	Technische Universiteit Delft
	prof.dr. J.D.R. Harting	
	prof.dr.ir. J.G.M. Kuerten	
	prof.dr.ir. M. Van Sint Annaland	
adviseur(s):	Dr.-Ing. H. Marschall	Technische Universität Darmstad

Het onderzoek of ontwerp dat in dit proefschrift wordt beschreven is uitgevoerd in overeenstemming met de TU/e Gedragscode Wetenschapsbeoefening.

Voor mijn lieve opa

TABLE OF CONTENTS

Bubbles on the Cutting Edge,

Direct Numerical Simulations of Gas-Liquid-Solid Three-Phase Flows

Gas-liquid-solid three-phase flows are frequently encountered in chemical, petrochemical and bio-chemical processes. In many cases, gaseous reactants are converted into liquid products in the presence of a solid catalyst. The main reactor configurations for these processes are trickle bed reactors and bubble slurry columns. Although a trickle bed column enables intimate three-phase contacting and avoids the separation of the stationary catalyst, the temperature control in these reactors is difficult. Consequently, the throughput of the gas and liquid is limited. These disadvantages can be alleviated by using a bubble slurry column. In these systems, however, the catalyst is dispersed as fine particles in the product stream. Consequently, a filtration unit is needed to recover the catalyst. Besides, the pronounced coalescence impedes the overall gas-liquid mass transfer.

To overcome these restrictions due to heat transfer and mass transfer limitations, in this work a new reactor type is proposed: the micro-structured bubble column. In this new reactor, the catalyst particles are replaced by catalyst-coated static meshes made of thin wires. The wire mesh serves the purpose of cutting the coalesced bubbles into smaller bubbles thereby increasing the specific interfacial area. The interaction with the wire mesh will also enhance the interface dynamics resulting in a higher surface renewal rate. As a result of this increase in the surface renewal rate, the gas liquid mass transfer will increase exactly at the desired position, i.e. near the catalyst. Finally, there is no need for filtration equipment, because the catalyst is immobilized.

To enhance our understanding of the complex prevailing fluid-structure interactions, Multiphase Computational Fluid Dynamics are useful. In the larger scale models, i.e. the Euler-Euler and Euler-Lagrangian models, closures are needed to describe the phase interactions between for instance the wire mesh and the bubbles. To determine these three-phase closures Direct Numerical Simulations (DNS) are used. The model used in this work is based on the combination of two powerful DNS techniques for gas-liquid and fluid-solid systems.

A Volume of Fluid (VoF) method is used to capture the gas-liquid interface dynamics. This method is an interface capturing method, which is volume conservative. To improve the method, three models to account for the surface tension are implemented: the common

Continuum Surface Force (CSF) method, the height function method and the tensile force method. Furthermore, a pressure jump correction method is implemented to decrease spurious currents. Each of the surface tension models was verified and subsequently validated. The verification tests show that the surface tension is not accurately represented when the CSF method is used.

The VoF models are validated using a single rising bubble in the industrial relevant regime of the Grace diagram. Generally, the height function model is the best performing model for small bubbles, i.e. for Eötvös numbers (Eo) smaller than 1, while the tensile force method is the best performing model for large bubbles (Eo > 10). All bubbles with $1 \leq \text{Eo} \leq 10$ are accurately represented by either of these methods. Besides the validation with single bubbles, the VoF model is also validated for binary bubble interaction. Using a relatively simple system of two equally sized bubbles, the rise velocity of the trailing bubble and the bubble shapes obtained with the VoF model compare favorably well to the experimental results. Nevertheless, it should be noted that all VoF simulations showed coalescence while no coalescence occurred in the experiments. As a consequence, the VoF model can not be used to assess whether coalescence or no coalescence prevails.

To incorporate the fluid-structure interactions at the wire mesh surface, an Immersed Boundary (IB) method is used. In this work, two different IB methods are compared. First of all, the Uhlmann method enforces the no-slip condition with the aid of Lagrangian force points that are distributed over the solid surface. This model is extended to enable the calculation of neutrally buoyant objects. Moreover, a second order implicit IB method is used. In this method, the no-slip boundary condition is enforced at the level of the discretised equations using a second order (1D) polynomial fit of the fluid velocity near the particle surface. This method was extended for systems with a variable viscosity and locally high volume fractions.

Both the IB models were verified and validated and it is concluded that the first order IB method is only able to accurately calculate the drag force on particles and the velocity profile when the Lagrangian force points are placed on a computational particle that is slightly smaller than the real particle. Because there is no analytical solution to determine the right computational size of objects other than spheres, the use of the second order IB method is advised, except for freely moving particles at Reynolds numbers above 100, because these particles acquire an unphysical rotational velocity due to approximations in the calculation of the torque.

To enable the simulation of dispersed gas-liquid-solid three phase flows, the second order IB method was combined with the Front Tracking (FT) gas-liquid DNS model. This combined model is able to simulate dense gas-liquid-solid systems while avoiding artificial coalescence, due to the Lagrangian representation of the interface with a surface mesh in the FT model. With the combined FT-IB method, the effect of the void fraction and the solids volume fraction on the drag force of the 2 mm bubbles and 1 mm particles is determined, resulting in correlations for the effective drag in dispersed gas-liquid-solid three-phase flows.

xi

After the VoF and the second order IB method were validated separately, the combined model is also validated for the case of interaction of a single bubble with the simplest form of a wire mesh, i.e. a single wire. Despite of the slight overestimation of the bubble rise velocity near the wire, the bubble shape, size, trajectory and rise velocity predicted by the VOF-IB method are in very good agreement with the experimental results. After validation, this model is used to systematically study the interactions of a single bubble with a single wire. The effect of the bubble size, the physical properties, the bubble velocity and the wire diameter are assessed. It is concluded that Eo and the wire diameter are the main parameters influencing the bubble cutting for straight interactions.

In addition, the interaction of a single rising bubble with a square wire mesh is also studied with the combined VoF-IB method. Two different alignments are used: i) a bubble hitting the center of an opening in the wire mesh, and ii) a bubble hitting the intersection of two wires in the mesh. In the first alignment, bubble cutting was not observed in the simulations, while based on purely geometrical considerations cutting was expected with the smallest openings. For larger bubbles (Eo $>$ 4), the bubbles are highly deformable and squeeze themselves through the opening of the wire mesh. For cases with small bubbles and/or a small opening the bubble gets stuck underneath the mesh. When the bubble is aligned with the intersection of the wire mesh, only the biggest bubbles (Eo = 15) are cut by the mesh, while the other bubbles get stuck underneath the mesh.

Bellen op het scherpst van de snede,
Directe Numerieke Simulaties van Gas, Vloeistof en Vaste Stof Drie-Fase Stromingen

Drie fase stromingen van gas vloeistof en vaste stof worden vaak toegepast in chemische, petrochemische en biochemische processen. Doorgaans worden in dit soort stromingen gas fase reactanten omgezet in vloeibare producten met behulp van een katalysator in vaste fase. Deze processen worden voornamelijk uitgevoerd in "trickle bed" reactoren en slurry bellenkolommen. Ondanks het zeer innige contact tussen de drie fasen en de makkelijke scheiding van de katalysator en de producten in "trickle bed" reactoren, is de toepasbaarheid van deze reactoren gelimiteerd door de beheersing van de temperatuur in de reactor. Daardoor is de capaciteit van dit soort reactoren beperkt. Deze nadelen kunnen deels worden weggenomen door gebruik te maken van een slurry bellenkolom. Echter, in deze reactoren is de katalysator in de vorm van fijne deeltjes verdeeld in de productstroom. Daarom is er een extra filtratie module nodig om de katalysator terug te winnen. Daarnaast belemmert de coalescentie van bellen (het samentrekken van bellen) het globale massatransport van de gas fase naar de vloeistof fase en vice versa.

Om de beperkingen vanwege de limitaties in warmte- en massatransport te ondervangen, wordt in dit werk een nieuw type reactor voorgesteld: een micro-gestructureerde bellenkolom. In deze reactor worden de katalysator deeltjes vervangen door een statisch gaasstructuur dat bestaat uit met katalysator gecoate dunne draden. Het gaas zorgt ervoor dat de grote bellen worden opgeknipt in kleinere bellen, waardoor het specifieke contactoppervlak tussen de gas en vloeistof fasen worden vergroot. Daarnaast zorgt de interactie van de bellen met het gaas voor een verhoging van de dynamica van het grensvlak, wat zal resulteren in een hogere verversingssnelheid van het oppervlak. Doordat de verversingssneldheid wordt verhoogt, zal ook de massaoverdracht tussen de gas en vloeistof fasen worden vergroot, en wel op de gewenste positie, namelijk in de buurt van de katalysator.

Om onze kennis over de complexe heersende fluïdum-structuur interacties te vergroten kan gebruik worden gemaakt van Meerfasen "Computational Fluid Dynamics". In de Euler-Euler en Euler-Lagrange modellen, die een (industriële) kolom kunnen beschrijven, zijn sluitingscorrelaties nodig voor het beschrijven van de interacties tussen de verschillende fasen, zoals de interacties tussen het gaas en de bellen. Deze sluitingscorrelaties kunnen

worden verkregen met behulp van Directe Numerieke Simulaties (DNS). Het DNS model dat wordt gebruikt in dit werk is gebaseerd op een combinatie van twee effectieve DNS methodes voor gas-vloeistof en vaste stof-fluïdum systemen.

Om de dynamica van het gas-vloeistof grensvlak te beschrijven wordt gebruik gemaakt van een "Volume of Fluid" (VoF) methode. Deze methode volgt het grensvlak met behulp van een indicator functie en is inherent volume conservatief. Om de methode te verbeteren zijn er drie modellen voor de oppervlaktespanning toegevoegd aan het model: het gebruikelijke "Continuum Surface Force" (CSF) model, de "height function" methode en de "tensile force" methode. Tevens is er een druksprong correctie methode toegevoegd om de pseudo-stromingen te verminderen. Alle oppervlaktespanningsmodellen zijn geverifieerd en gevalideerd. Uit de verificatie tests blijkt dat de oppervlaktespanning niet goed wordt gerepresenteerd door het CSF model.

De verschillende VoF modellen zijn gevalideerd met het stijgen van enkele bellen in het industrieel relevante gebied van het Grace diagram. Doorgaans is het "height function" model het beste oppervlaktespanningsmodel voor kleine bellen, dat wil zeggen voor bellen met een Eötvös nummer (Eo) kleiner dan 1, terwijl het "tensile force" model het beste model is voor grotere bellen (Eo>10). Voor alle bellen met $1 \leq \text{Eo} \leq 10$ worden door zowel door het "height function" model als door het "tensile force" model goed gerepresenteerd. Naast de validatie met enkele bellen, is het VoF model ook gevalideerd voor de interactie tussen twee bellen. Voor een relatief simpel systeem van twee even grote bellen, komen de stijgsnelheden en de vorm van de bellen in het VoF model goed overeen met de experimenten. Desondanks, was in alle VoF simulaties spraken van coalescentie van de bellen terwijl de bellen in de experimenten niet samenvoegen. Daarom kan het VoF model niet worden gebruikt om te bepalen of bellen samenvoegen of niet.

De interactie tussen het fluïdum en de vaste structuren worden beschreven met een "Immersed Boundary" (IB) model. In dit werk worden twee verschillende IB methodes vergeleken. Ten eerste legt de IB methode van Ulhmann de no slip-randvoorwaarde op met behulp van Lagrangian marker punten die over het oppervlak van het object zijn verspreid. De methode is uitgebreid om ervoor te zorgen dat ook deeltjes met een neutraal drijfvermogen ook kunnen worden gesimuleerd. Daarnaast wordt er een tweede orde impliciete IB methode gebruikt. In deze methode wordt de no slip-randvoorwaarde opgelegd op het niveau van de gediscretiseerde Navier Stokes vergelijkingen met behulp van en tweede orde (1D) polynoom die wordt aangenomen in het fluïdum nabij het oppervlak. Deze methode is aangepast voor het gebruik van systemen met een veranderlijke viscositeit en lokaal hoge volume fracties.

Uit de validatie en verificatie tests voor beide IB modellen, is gebleken dat de eerste orde IB methode alleen de wrijvingskracht en het snelheidsprofiel nauwkeurig kan bepalen als de Lagrangian marker punten op een numeriek deeltje worden geplaatst dat kleiner is dan het werkelijke deeltje. Omdat er geen analytische oplossing is om deze numerieke grootte te bepalen voor niet-sferische objecten, is het advies om de tweede orde IB method

te gebruiken behalve bij vrij bewegende deeltje met een Reynolds getal groter dan 100, want dan verkrijgen de deeltjes een niet fysische rotatie snelheid door de aannames die zijn gedaan in de berekening van de torsie.

Om dichte zwermen van bellen en deeltjes te simuleren, is de tweede orde IB methode gecombineerd met het "Front Tracking" (FT) gas-vloeistof DNS model. Dit gecombineerde model kan dichte gecombineerde deeltjes- en bellenzwermen simuleren zonder artificiële coalescentie van de bellen door de Lagrangiaanse representatie van het gas-vloeistof grensvalk in het FT model. Met behulp van deze gecombineerde FT-IB methode is het effect van de gasfractie en de volume fractie van de deeltjes op de wrijvingskracht van de 2 mm bellen en de 1 mm deeltjes bepaald. Dit resulteerde in een correlatie voor de effectieve wrijvingskracht op de bellen en de deeltjes in drie fase stromingen.

Afgezien van de aparte validatie van het VoF model en de tweede orde IB methode, is het gecombineerde VoF-IB model ook gevalideerd voor de interactie van een enkele bel met de simpelste vorm van een gaas structuur, dat wil zeggen een enkele draad. Hoewel de stijgsnelheid van de bel in de buurt van de draad lichtelijk wordt overschat, komen de vorm, de grootte, het pad en de stijgsnelheid van de bel(len) in de VoF-IB method goed overeen met de experimentele resultaten. Vervolgens is het gecombineerde model gebruikt om systematisch de interacties tussen een enkele bel en een enkele draad te bestuderen. Daarbij zijn de effecten van de belgrootte, de fysische eigenschappen, de stijgsnelheid van de bel en de diameter van de draad onderzocht. Uit de studie is geconcludeerd dat de belangrijkste parameters voor het snijden van de bellen de grootte van de bel en de diameter van de draad zijn.

Aansluitend is de interactie tussen een enkele bel en een vierkante gaasstructuur onderzocht met de gecombineerde VoF-IB methode. Er is gebruik gemaakt van twee verschillende horizontale uitlijningen van de bel met respect tot het gaas: i) de bel is recht onder een opening in het gaas geplaatst, en ii) een bel is recht onder een kruising van twee draden geplaatst. In de eerste situatie is er in geen van de interacties sprake van splitsing van bellen, terwijl dit op basis van uitsluitend geometrische overweging wel was verwacht bij de kleinste gaasopeningen. De grote bellen (Eo > 4) zijn erg vervormbaar, waardoor ze zich door de opening van het gaas heen wringen. Voor interacties met kleine bellen en/of een kleine opening komt de bel vast te zitten onder de gaas structuur. Alleen de grootste bellen (Eo=15) die recht onder de kruising van het gaas beginnen worden opgebroken door de interactie met de gaasstructuur. Alle andere bellen blijven steken onder het gaas.

Nomenclature

Variables

a	coefficient
$\tilde{a}$	modified coefficient
A	surface area, [m^2]
b	explicit part of the Navier-Stokes equations or impact parameter
$\tilde{b}$	modified explicit part of the Navier-Stokes equations
C	coefficient
d	diameter or distance, [m]
E	bubble aspect ratio (height vs. width)
$\mathbf{f}$	force density at the Eulerian grid, [N/m^3]
F	phase fraction or Level-Set function
$\mathbf{F}$	force or force density, [N] or [N/m^3]
$\mathbf{g}$	gravitational constant, [m/s^2]
h	height, [m]
$h, \Delta x, \Delta y, \Delta z$	mesh size, [m]
I	moment of inertia, [kg/m^2]
$\mathbf{n}$	normal
n_x, n_y, n_z	number of cells in x, y, z direction
p	pressure, [Pa]
Δp	pressure jump, [Pa]
$\mathbf{r}$	position, [m]
R	radius, [m]
$\mathbf{R}$	position of the force point, [m]
s	mesh opening, [m]
S	surface area, [m^2]
t	time, [s]
Δt	time step, [s]
$\mathbf{t}$	tangent, [m]
$\mathbf{T}$	torque, [Nm]
$\mathbf{u}$	fluid velocity, [m/s]

$\mathbf{U}$	fluid velocity at a force point, [m/s]
v_∞	uniform stream velocity, [m/s]
$\mathbf{v}$	bubble or particle velocity, [m/s]
V	volume, [m^3]
ΔV_m	force point volume, [m^3]
$\mathbf{w}$	translational particle velocity, [m/s]

Greek letters

α	void fraction
Γ	surface area
δ	weighing function
ϵ	error
ζ	dimensionless distance
κ	curvature, [1/m]
μ	viscosity, [Pa $\cdot$ s]
ρ	density, [kg/m^3]
σ	surface tension coefficient, [N/m]
$\boldsymbol{\tau}$	stress tensor, [Pa]
ϕ	solids volume fraction
ψ	velocity component, [m/s]
$\boldsymbol{\omega}$	rotational particle velocity, [rotations/s]
Ω	volume

Subscripts and superscripts

b	bubble
c	central
D	drag
g	gas phase
G	gravity
IB	Immersed Boundary
l	liquid phase
m	marker, interface element or particle number
max	maximal
nb	neighboring
p	particle
Δp	pressure jump
P	hydrostatic pressure
s	solid phase

s, $s0$, $s2$	surface of the particle
w	wire
σ	surface tension
∞	single rising bubble or single falling particle in an infinite liquid

Abbreviations

ALE	Arbitrary Lagrangian-Eulerian
CFD	Computational Fluid Dynamics
CLSVoF	Coupled Level-Set and Volume of Fluid
CSS	Continuous Surface Stress
CSF	Continuum Surface Force
DNS	Direct Numerical Simulations
(E)LVIRA	(Efficient) Least squares Volume of Fluid Interface Reconstruction Algorithm
FT	Front Tracking
g	gas phase
G	Grace diagram
HF	Height Function
IB	Immersed Boundary
ICCG	Incomplete Cholesky Conjugate Gradient
l	liquid phase
LS	Level-Set
PLIC	Piecewise Linear Interface Calculation
PROST	Parabolic Reconstruction of Surface Tension
s	solid phase
T	Tomiyama
TF	Tensile Force
VoF	Volume of Fluid

Dimensionless numbers

Ca	Capillary number, $\mu_l v_{max,l}/\sigma$
Eo	Eötvös number, $g_z d_b^2 \rho_l/\sigma$
Mo	Morton number, $g_z \mu_l^4 \Delta\rho/\left(\rho_l^2 \sigma^3\right)$
Oh	Ohnesorge number, $\mu_g \sqrt{\rho_g \sigma d_b}$
Re	Reynolds number, $\rho\|\mathbf{v}\| d_b/\mu_l$

INTRODUCTION

1.1 Background and motivation

Chemical, petrochemical and bio-chemical processes often involve the contacting of gas-liquid-solid flows. In these processes, the solid phase generally acts as a catalyst, while the gas phase carries the reactants and the liquid the products (Höller et al., 2001; Jain et al., 2013; Segers, 2015).

The two main reactor configurations for these three-phase processes are trickle bed reactors and bubble slurry columns. In a trickle bed reactor, the liquid trickles over a packing (random or structured) in the presence of a co-current gas flow. The advantage of this type of three-phase reactor is the intimate contacting between the three phases and the avoidance of separation of the stationary catalyst. In spite of these advantages, the temperature control in trickle bed reactors is difficult, especially when the particles are partly dewetted because of the relatively unfavorable thermophysical properties of the (continuous) gas phase. In addition, the relative throughput of the gas and liquid is limited in comparison to other reactor configurations (Höller et al., 2001; Segers, 2015).

In a bubble slurry column, the (fine) particles are dispersed in the liquid. Although this reactor can handle high throughputs and offers excellent temperature control, pronounced bubble coalescence impedes the overall gas-liquid mass transfer. Besides, the fine catalyst particles remain in the liquid phase requiring a filtration unit to recover the catalyst (Höller et al., 2001; Segers et al., 2013; Segers, 2015).

To overcome the restrictions due to limited heat removal or low mass transfer coefficients, a new reactor type is proposed: a micro-structured bubble column. In this column,

the catalyst particles are replaced by static meshes of thin wires that are coated with the catalyst. The wires are meant to cut the coalesced bubbles into smaller bubbles, which increases the specific interfacial area. Furthermore, the interaction between the wire mesh and the bubbles will enhance the interface dynamics and therefore the surface renewal rate. Because of the higher surface renewal rate, the mass transport between the gas and liquid phase is enhanced exactly at the desired position near the catalyst. Finally, by coating the wire mesh with the catalyst, there is no need for external filtration equipment to separate the liquid product and the catalyst phase (Höller et al., 2001; Prasser et al., 2001; Ito et al., 2011; Jain et al., 2013; Segers et al., 2013; Segers, 2015). Höller et al. (2001) showed that a similar approach leads to a 10 times higher gas-liquid mass transfer coefficient compared to a bubble column without any internals.

To optimize the performance of such a micro-structured bubble column, a proper understanding of the multiphase flow phenomena is required. In view of the inherent experimental limitations to the optical access required for application of optical techniques and the intrusiveness of (optical) probes and wire mesh sensors, a Computational Fluid Dynamics (CFD) approach is followed in this study (Prasser et al., 2001; Ito et al., 2011; Roghair, 2012).

1.2   Multi-scale modeling approach

Industrial size bubble (slurry) columns are typically tens of meters tall, while the smallest bubble size is in the range of several millimeters. Due to these large differences in the length scales and the associated time scales, CFD is not able to fully resolve all relevant details for industrial size columns in spite of the recent advances in computational power. To overcome this problem, a multi-scale modeling approach is adapted, as shown in figure 1.1. In this approach, the smaller scale models provide closures for the larger scale models, ensuring accurate representation of the small scale phenomena while using relatively modest computational power (van Sint Annaland et al., 2003; Deen et al., 2004; Yang et al., 2007; Raessi et al., 2010; Roghair et al., 2011).

In the multi-scale modeling approach the largest scales are described by Euler-Euler models, as shown in figure 1.1.c. In these models, all phases are considered as continuous interpenetrating fluids. Although this model in principle is able to simulate large (slurry) bubble columns, closure relations are needed to capture the bubble-bubble, bubble-liquid, bubble-solid, liquid-solid and solid-solid interactions (Yang et al., 2007; Roghair et al., 2011).

These closure relations can partly be provided by the Euler-Lagrangian models, which are models at the intermediate scale. These models solve the volume-averaged Navier-Stokes equations for the continuous phase, while the bubbles and the solid objects are tracked individually in a Lagrangian framework, as shown in figure 1.1.b. The Euler-Lagrange models are suitable for studying large scale swarm effects and the effects of coalescence and break-up. Because the model only solves the volume-averaged Navier-Stokes equations and does not resolve the bubble dynamics, the bubble-liquid and solid-liquid interactions have
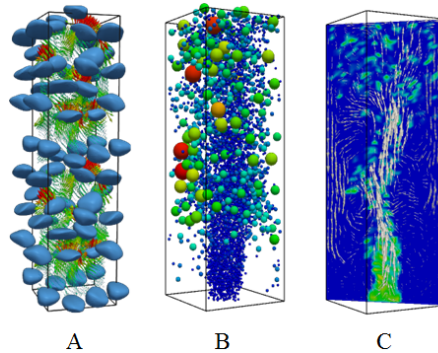
Figure 1.1: The multi-scale modeling approach for gas-liquid flow (Roghair et al., 2011). Figure A shows a simulation using Direct Numerical Simulations, figure B a simulation with an Euler-Lagrangian model and figure C a simulation with an Euler-Euler model.

to be included via closure correlations, e.g. the drag and lift correlations (Deen et al., 2004; Yang et al., 2007; Roghair et al., 2011).

At the smallest scale Direct Numerical Simulations (DNS) can be used to generate these closures. In DNS, all details of the flow field are fully resolved, i.e. the governing equations are solved without any rigorous a priori assumptions or simplifications. Although this leads to a very accurate description of the flow field, the simulation size is limited to $O(10^2)$ bubbles due to the high computational costs (Deen et al., 2004; Yang et al., 2007; Roghair et al., 2011).

In this work, the understanding of three-phase flows will be expanded using DNS. Several authors developed three-phase DNS methods starting from the widely available two-phase DNS methods. Li et al. (2001) used a combined Euler-Lagrangian and DNS approach to capture the three-phase flows. However, this model still requires closures for the solid-liquid interactions, because the particles are taken into account as Lagrangian point particles. Ge and Fan (2006) and Jain et al. (2012) used a combination of a front capturing technique, which reconstructs the gas-liquid interface instead of directly tracking the interface, with an Immersed Boundary method to obtain a DNS method for three-phase flows. The advantage in these methods is the inherent ability of simulating the coalescence and break-up of the bubbles, but this might also lead to non-physical coalescence of the bubbles (bubbles merge as soon as their interfaces enter the same computational grid cell). To overcome these problems, Deen et al. (2009) combined a front tracking technique with an Immersed Boundary method. The disadvantage of this method however is that the coalescence and break-up of bubbles has to be included via a sub-grid model.

In this work, closures will be developed to subsequently improve the higher order models, like the Euler-Lagrange models, using a three-phase DNS model. Previously obtained closures focused on two phase flows, which will now be expanded through interactions due to the presence of a third phase (Roghair et al., 2011, 2013a; Tang et al., 2014, 2015). The

main focus is to determine how the micro-structuring influences the hydrodynamics and bubble size in bubble columns. Jain et al. (2013) proposed a basic geometrical closure to determine the size of bubbles after being cut by a wire mesh. In this work, this first closure will be improved using detailed information obtained from DNS. Moreover, the three-phase simulations will be used to determine the effect of particles on the drag force on bubbles and vice versa in three phase flows.

1.3   Thesis outline

To study the effect of the wire mesh on the hydrodynamics in a bubble column, a three-phase DNS method is developed. This method is created by combining a gas-liquid DNS model and a fluid-solid DNS model. To determine the most appropriate numerical models, different gas-liquid and fluid-solid models are respectively compared in chapters 2 and 3. In these chapters, all models are also verified and validated.

Although the gas-liquid models are already validated for the rise of single bubbles in a quiescent liquid in chapter 2, the models should also be able to accurately capture the interaction between the bubbles. Therefore, the gas-liquid model is validated for these interactions in chapter 4.

In chapter 5, a three-phase DNS model is used to model the interactions of bubbles and particles in a three-phase swarm. In this chapter, correlations are obtained for the effective drag force acting on both the bubbles and the particles.

Chapters 6 and 7 describe the bubble cutting due to wire meshes. In chapter 6, the interactions with the simplest form of a wire mesh, a single wire, are validated. Subsequently, the effects of different physical parameters, e.g. the bubble size and the wire diameter, on the bubble cutting using a single wire are determined. Finally, in chapter 7 the effect of square wire meshes on the cutting of the bubbles will be determined.

The last chapter, chapter 8, provides preliminary results on bubble cutting with wire meshes, along with recommendations for future work.

Gas-Liquid Direct Numerical Simulation Models

2.1 Introduction

The flow of two immiscible fluids can be resolved with several different Direct Numerical Simulation (DNS) models. These models can be divided into two classes: moving grid methods and fixed grid methods. In the first class, the grid is attached to the interface, which enables a good calculation of the surface properties. Although the description of the surface properties is challenging in the fixed grid methods, the use of a stationary (Eulerian) fixed grid enables the handling of strong topological changes (Scardovelli and Zaleski, 1999; van Sint Annaland et al., 2005; Roghair et al., 2011). Because highly deformed interfaces occur frequently, fixed grid methods are used in this study.

The main fixed grid methods are the Front Tracking (FT) method, the Volume of Fluid (VoF) method and the Level-Set (LS) method (Son, 2003; Albadawi et al., 2013). The essential difference between these models is the interface treatment. Only the Front Tracking method tracks the interface between the two phases explicitly by using a Lagrangian grid that represents the gas-liquid interface. Using this Lagrangian grid, the shape and the position of the interface is exactly known. Therefore, the calculation of the surface properties is accurate and relatively easy without the need of a highly refined grid. Besides, the use of a Lagrangian grid prevents numerical diffusion of the interface. However, there are three major disadvantages of the Front Tracking method. First of all, the interface tracking is complex, especially when bubble break-up or coalescence is considered. Furthermore,

topological changes of the interface will result in the need for restructuring of the interface markers to ensure an accurate description of the interface. Doing this in a volume conserving manner is cumbersome. Third, the mapping from the Eulerian grid to the Lagrangian grid and vice versa will lead to mass conservation problems (Chang et al., 1996; Shin and Juric, 2002; van Sint Annaland et al., 2005; Kwakkel et al., 2012).

In both the VoF method and the LS method, the interface is captured rather than tracked. In the LS method, the interface is captured using a Level-Set function, F, that describes the distance from the interface that is positive in one fluid and negative in the other fluid. The interface is advected with the local velocity using equation 2.1.

$$\frac{DF}{Dt} = \frac{\partial F}{\partial t} + \mathbf{u} \cdot \nabla F = 0 \tag{2.1}$$

The advantage of using a smooth function to capture the interface is the accurate description of the interface and thus the surface properties, like the interface normal, the curvature and the surface tension. However, due to the advection with the locally mapped velocity according to equation 2.1, the Level-Set function will no longer act as a distance function after advection, which will lead to problems in the mass conservation for highly deformed surfaces. Furthermore, because all bubbles automatically merge when they are close, the obtained bubble coalescence might be unphysical (Gerlach et al., 2006; Popinet, 2009; Albadawi et al., 2013).

In the VoF method, a color function is used for tracking the bubble volumes. The color function indicates the amount of liquid present in a certain cell. The interface between the two liquids can be reconstructed from this color function. Using the reconstructed interface, the phase fraction can be advected with equation 2.1, while conserving the volume of the liquid (and hence also the volume of the gas). However, due to the reconstruction of the interface, a non-smooth interface is obtained, which may lead to difficulties in the calculation of the surface properties. Furthermore, when two bubbles are within a distance less than one computational cell from each other, the bubbles will automatically coalesce (Lafaurie et al., 1994; van Sint Annaland et al., 2005; Jafari et al., 2007).

Due to the complementary advantages of the different DNS models, both the FT model and the VoF model are used to study the bubble behavior. This chapter describes the main characteristics of both the models. In the next sections, the surface tension calculation and the interface tracking of the FT model and the VoF model are explained separately. Subsequently, the model implementation is verified using standard verification tests for gas-liquid models. Finally, the model is also validated against experimental data.

2.2   Governing equations

Because the only difference between the FT model and the VoF model is the interface treatment, the governing equations of the two models are the same. In this section, the main

characteristics will be discussed. The models are based on the FT model of Roghair et al. (2013a) and the VoF model of van Sint Annaland et al. (2005).

In both the FT and the VoF model, the continuity equation (equation 2.2) and the Navier-Stokes equations (equation 2.3) are solved assuming incompressible flow.

$$\nabla \cdot \mathbf{u} = 0 \tag{2.2}$$

$$\rho \frac{\partial \mathbf{u}}{\partial t} = -\nabla p - \rho \nabla \cdot (\mathbf{u}\mathbf{u}) - \nabla \cdot \boldsymbol{\tau} + \rho \mathbf{g} + \mathbf{F}_\sigma \tag{2.3}$$

Because the velocity is continuous even across the interface, a one-field approximation can be used to solve the velocity in the entire domain. To take into account the surface tension at the interface, an extra force density, $\mathbf{F}_\sigma$, appears in equation 2.3. The calculation of this force density depends on the used model and will be discussed in the next sections.

In both models, a mismatch may arise in the discretisation of the surface tension and the pressure field, which can be decreased if the calculation of the surface tension and the pressure field are coupled. This can either be done by introducing the surface tension in the continuity equation (Renardy and Renardy, 2002; Francois et al., 2006) or by introducing an extra pressure force density at the interface in the Navier-Stokes equations (Dijkhuizen et al., 2010b). Because the surface tension model is implemented as a force density, we choose the second approach.

$$\mathbf{F}_{\Delta p, m} = A_m \frac{\sum_i \mathbf{F}_{\sigma,i} \cdot \mathbf{n}_i}{\sum_i A_i} \tag{2.4}$$

The pressure jump correction is calculated with equation 2.4 separately for each bubble. The summation in equation 2.4 is performed over all the markers of a single bubble in the FT model, while in the VoF model the summation is over all reconstructed interface elements of a single bubble, including the interface elements which are created by the smoothing operation. The overall pressure jump is distributed to the interface elements weighted by the area of the interface element, A_m, as depicted in equation 2.4. The extra force density ($\mathbf{F}_{\Delta p, m}$) is subtracted from the force density representing the surface tension.

The velocity, which is calculated in a staggered-grid configuration, is solved using a projection-correction method. In this method, an approximation of the new velocity field is calculated with equation 2.3. All terms in this equation are solved explicitly except for the diffusion term, which is treated semi-implicitly. The implicit part of the diffusion term is chosen such that it only depends on the velocity component that is solved, whereas the remaining explicit terms are relatively small. The convective term is discretised using a second order flux-delimited Barton scheme, while the discretisation of the diffusion term is done with the second order central difference scheme. The estimation of the velocity
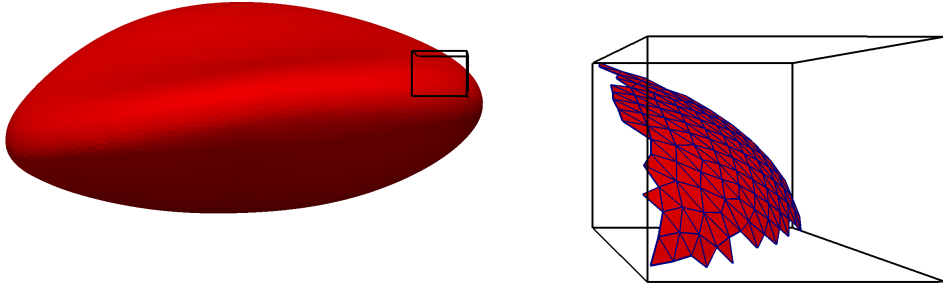
Figure 2.1: Lagrangian representation of a bubble. The figure on the right shows an enlargement of the surface mesh.

is corrected to meet the continuity equation (equation 2.2). Both the implicit part of the projection step and the correction step are solved using a block ICCG matrix solver. The solver has been parallelised using OpenMP.

After the calculation of the velocity field, the new phase fraction in each cell can be determined. Because this advection is different for the FT and VoF model, this part of the code will be discussed separately in the following sections. From the obtained phase fractions, the new density and viscosity can be determined according to equation 2.5 and 2.6 by linear and harmonic averaging respectively.

$$\rho = F\rho_1 + (1 - F)\rho_2 \tag{2.5}$$

$$\frac{\rho}{\mu} = F\frac{\rho_1}{\mu_1} + (1 - F)\frac{\rho_2}{\mu_2} \tag{2.6}$$

2.3 Front Tracking model

2.3.1 Surface tension modeling

As discussed previously, the Front Tracking method explicitly tracks the interface of the bubbles with a Lagrangian mesh, which is shown in figure 2.1. The triangular markers are directly used for the calculation of the force density representing the surface tension. If we consider a single marker m, then each of the neighboring markers i exert a tensile force that can be calculated using equation 2.7.

$$\mathbf{F}_{\sigma,(i,m)} = \sigma \left(\mathbf{t}_{i,m} \times \mathbf{n}_{\text{edge}} \right) \tag{2.7}$$

In this equation, $\mathbf{t}_{i,m}$ is the shared tangent of marker i and m and $\mathbf{n}_{edge}$ the normal of the tangent between markers i and m.

$$\mathbf{n}_{\text{edge}} = \frac{1}{2}(\mathbf{n}_i + \mathbf{n}_m) \tag{2.8}$$

Summing over all three edges of marker m the surface tension on a marker can be determined, as shown in equation 2.9. Because the net tensile force over an enclosed surface is zero, the calculation of the surface tension only contains the normals on the neighboring marker i. The calculated force is distributed to the Eulerian grid from the center of the marker using mass-weighting (Deen et al., 2004).

$$\mathbf{F}_{\sigma,m} = \frac{1}{2}\sigma \sum_{i=1}^{3} \left(\mathbf{t}_{i,m} \times \mathbf{n}_i + \mathbf{t}_{i,m} \times \mathbf{n}_m \right) = \frac{1}{2}\sigma \sum_{i=1}^{3} \left(\mathbf{t}_{i,m} \times \mathbf{n}_i \right) \tag{2.9}$$

2.3.2 Bubble advection

To advect the bubble, the Lagrangian mesh has to be advected with the local velocity. The local velocity at each marker point of the Lagrangian mesh can be determined using a piecewise cubic spline interpolation of the velocity field determined on the Eulerian grid. When the local velocity at the marker points is known, the marker points are individually moved using fourth order Runga-Kutta time stepping.

Due to the advection of the individual marker points, the bubble changes both its position and shape. However, the separate advection of the marker points causes the distance between the marker points to change, which can lead to a decrease in the quality of the interface mesh. To improve the quality of the mesh after advection, a remeshing procedure is introduced. This procedure includes four different elementary remeshing operations. First of all, if the distance between two connected markers is too large, edge splitting is applied, which is the introduction of a new marker point. Secondly, when two marker points are too close, the two points are merged to a single point, which is called edge collapsing. Furthermore, swapping the central edge of two markers can also improve the quality of the mesh. Finally, the entire Lagrangian mesh is smoothed. A detailed description of each of these operations is given by Roghair (2012).

The separate movement of all the marker points and the remeshing operations cause small volume changes per time step, which lead to a significant volume loss over the course of a simulation, due to the large number of time steps in a simulation. To overcome these numerical volume losses, the method of Kuprat et al. (2001) has been implemented in the smoothing procedure, which locally restores volume losses. However, volume losses due to the advection of the marker points are not corrected yet. Therefore, the overall volume loss will be compensated by adding the lost volume over the entire interface. This procedure might cause unphysical overlap between the bubbles. Therefore, marker points that are close to another bubble or wall are excluded from this operation.
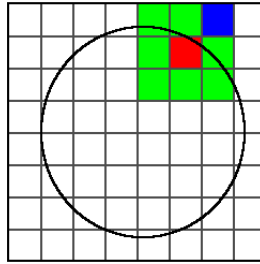
Figure 2.2: A schematic representation of the compass method. The red cell is the cell that resides in the bubble. When the compass method is applied all the green cells are also selected to reside within the bubble, while the blue cell is excluded.

2.3.3   Calculation of the phase fraction

Because the gas-liquid interface is directly tracked, the phase fraction should be calculated separately. Often, the phase fraction is determined by solving a Poisson equation (Unverdi and Tryggvason, 1992). However, this will lead to smearing of the phase fraction, numerical overshoots and undershoots and will increase the computational time. Therefore, a less demanding divergence theorem algorithm is used to calculate the local phase fractions from the position of the markers. This algorithm is only efficient when a marker triangle resides in a single cell. Consequently, all triangles that reside in multiple cells are split into multiple triangles that all reside in a single cell. Details of this algorithm can be found in the work of Dijkhuizen et al. (2010b) and Roghair (2012).

2.4   Volume of Fluid model

As discussed before, the Volume of Fluid (VoF) method does not directly track the bubble interface, but rather the bubble (or liquid) volume. Consequently the bubble tracking, the calculation of surface tension and the bubble advection in this model are all different from the calculations in the FT. In this section, these elements are discussed.

2.4.1   Bubble tracking

To accurately apply the pressure jump correction, the pressure jump of each bubble should be determined separately. Because the VoF method only tracks the color function, a separate bubble tracking method has to be implemented to track the bubbles. Suppose we know a single point within the bubble, indicated by the red cell in figure 2.2, we can determine if the surrounding cells contain any gas. If they contain gas, the green cells in figure 2.2, the cells are considered to be part of the bubble. While the blue cell, which does not contain any gas, is not considered to be part of the bubble. This check is repeated for all green cells, until the number of cells within the bubble does not change anymore.

The selected starting point for this procedure is the center of mass of the bubble, because this point is almost always inside the bubble. However, for wobbling, spherical cap, skirted and dimpled ellipsoidal bubbles, the center of mass of the bubble does not necessarily have to be inside the bubble. The starting point of the calculation is then moved in the opposite direction of the outward pointing normal, starting from the last known interface at the bubble center of mass.

Besides the selection of the starting point, three extra cases should be considered. First of all, consider two bubbles that have their interface in two adjoining cells. These bubbles will automatically merge due to the bubble tracking operation, which is clearly not desired. To decrease the chance of numerical merging of bubbles, the bubbles can only move when the angle between the surfaces is less than 90 degrees. Secondly, a cell cannot be part of multiple bubbles. When a cell is already part of another bubble, the bubbles automatically merge. Finally, when a bubble breaks up, the center of mass will only be in one of the daughter bubbles. Therefore only one of the bubbles will be tracked. To ensure that all the bubbles in the domain are tracked, the bounding box of the bubble will be searched for new bubbles in cases that the bubble size decreases more than 0.001%.

2.4.2 Surface tension modeling

Because the VoF model does not directly track the interface, the calculation of surface properties, like the surface tension, is difficult and a lot of research has been devoted to these properties. The surface tension can be introduced into the model via two approaches: as a divergence of the stress tensor or as a force density (Lafaurie et al., 1994; Jafari et al., 2007). When the surface tension is introduced as a stress tensor, this is called the Continuous Surface Stress (CSS) model. In this model, the effects of the interface appear as an extra capillary pressure tensor (Lafaurie et al., 1994; Renardy and Renardy, 2002; Jafari et al., 2007). However, the implementation of the surface tension via the stress tensor is less accurate then the implementation via a force density (Meier et al., 2002; Albert et al., 2012).

Hence, the most common surface tension model in the VoF model implements the surface tension as a force density. This Continuum Surface Force (CSF) method of Brackbill et al. (1992) calculates the force density, $\mathbf{F}_\sigma$, using equation 2.10:

$$\mathbf{F}_\sigma = \sigma \kappa \mathbf{n} \qquad\qquad (2.10)$$

In this equation, σ is the surface tension coefficient, κ is the curvature of the interface and $\mathbf{n}$ is the normal at the interface. The normal and the curvature are calculated by respectively calculating the first order and second order spatial derivative of the color function (equation 2.11 and 2.12).

$$\mathbf{n} = \frac{\nabla F}{|\nabla F|} \qquad\qquad (2.11)$$

$$\kappa = -(\nabla \cdot \mathbf{n}) \tag{2.12}$$

To ensure that the surface tension only depends on the gradient in the color function and not on the value of the surface tension, equation 2.10 is multiplied with a function $g = \tilde{F}/ < F >$, in which $\tilde{F}$ is the value of the color function in the interface cell and $< F >$ the value of the color function at the interface. When the phase fraction is used as the color function, the function is equal to $g = 2F$. Using this definition the implemented surface tension is calculated with equation 2.13.

$$\mathbf{F}_\sigma = 2F\sigma\kappa\mathbf{n} \tag{2.13}$$

However, the phase fraction acts as a step function across the interface. Therefore, standard discretisation schemes cannot calculate the normal and the curvature accurately. This problem is overcome by smoothing the phase fraction around the interface with the polynomial expression of Deen et al. (2004). When a smoothing width of two grid cells is applied, the interface is effectively enlarged to a three grid cell thick interface, leading to numerical diffusion of the interface (Renardy and Renardy, 2002; Gerlach et al., 2006).

Although the introduction of smoothing solves the numerical problems of the CSF model, the curvature calculation, which is the main problem of the CSF, is not improved (Afkhami and Bussmann, 2009). The calculation of the curvature can be improved by a more accurate representation of the interface. This can be done using a least square method to fit the interface with a linear or a parabolic interface, as is done by the PROST-algorithm of Renardy and Renardy (2002) and the (E)LVIRA method of Pilliod Jr. and Puckett (2004) respectively. Rider and Kothe (1998) reconstruct the interface geometrically, using complicated surface integrals and an iterative procedure. Although these methods ensure a more accurate estimation of the curvature, the procedure to reconstruct the interface reduces the computational speed considerably (Son, 2003; Gerlach et al., 2006).

The curvature estimation can also be improved by combining the VoF model with the Level-Set method (CLSVoF). In this method, the phase fraction is calculated with the VoF method to ensure mass conservation, while the smooth LS function is used to accurately calculate the surface properties (Son, 2003; Gerlach et al., 2006; Albadawi et al., 2013). However, the implementation of the interface reconstruction in the CLSVoF model is still a problem, because the interface reconstruction has to be accurate for both the advection of the color function and the re-initialization of the LS function (Son, 2003).

Finally, the curvature approximation can also be improved using the height function model of Gerrits (2001). This model only changes the curvature calculation as compared to the CSF model of Brackbill et al. (1992), which means that the surface force and the normal are still calculated with equation 2.10 and 2.11, respectively. The only difference with the CSF calculation is that instead of the smoothed phase fraction the actual (non-smoothed)

phase fraction is used in the calculation of the normal (Gerrits, 2001; Cummins et al., 2005; Francois et al., 2006).

The curvature is calculated by the determination of the surface height, h. The height is obtained by the summation of the phase fraction in the direction of the largest component of the surface normal vector, which is performed on a 7x3x3 stencil around each interface cell. For instance, the normal component in a cell is largest in the z-direction. In this case, the height in each cell can be calculated with equation 2.14.

$$h(i, j, k) = \sum_{k-3}^{k+3} F(i, j, k) \Delta z \qquad (2.14)$$

From the local variations of the height, the curvature of the interface cell can be calculated with equation 2.15 (Gerrits, 2001; Cummins et al., 2005; Francois et al., 2006).

$$\kappa = \frac{\partial}{\partial x} \left(\frac{\frac{\partial h}{\partial x}}{\sqrt{1 + (\frac{\partial h}{\partial x})^2 + (\frac{\partial h}{\partial y})^2}} \right) + \frac{\partial}{\partial y} \left(\frac{\frac{\partial h}{\partial y}}{\sqrt{1 + (\frac{\partial h}{\partial x})^2 + (\frac{\partial h}{\partial y})^2}} \right) \qquad (2.15)$$

When equation 2.10 is used to calculate the surface tension, a force per unit surface area is calculated, while a force density is needed in the calculation of the Navier-Stokes equations. Therefore, the calculated force is multiplied by the area of the interface and divided by the volume of the cell.

The advantage of the implementation of the height function is the elimination of the smoothing of the color function. Moreover, the spurious currents in the model are reduced compared to the CSF model and the accuracy of the surface tension model is increased to O(h^2) (Gerrits, 2001; Cummins et al., 2005; Francois et al., 2006; Popinet, 2009). The implementation of the height function is based on a large stencil. This leads to a rapid decrease of the accuracy of the model when the distance between two interface cells is less than four grid cells in the direction of the largest normal. This situation can occur in the case of wobbling, spherical cap, skirted and dimpled bubbles.

Even though the improvement of the curvature calculation increases the accuracy of the VoF model, the use of a different kind of surface tension model might be even more effective. Currently, in the FT model a totally different model is used: the tensile force method of Tryggvason et al. (2001). This method was explained in detail in section 2.3. Summarizing, in this model the surface tension is calculated by summing all the tensile forces that the neighboring markers exert on the marker of interest. The calculation of this force is straightforward in the FT model because each of the edges of the interface marker is connected to a neighboring marker (Tryggvason et al., 2001; Shin and Juric, 2002; Dijkhuizen et al., 2010b).

Although the interface is not as well defined in the VoF model, the tensile force method can also be applied using the reconstructed PLIC (Piecewise Linear Interface Calculation) interfaces, that are used in calculating the advection of the color function. Due to the use of the reconstructed surface, there are a few differences in the implementation of the tensile force method for the VoF model as compared to the FT model. First of all, the reconstructed interface is described on basis of five different general shapes of the interfaces, which have three to six edges (see figure 2.3.a). Therefore, the summation of all edges should depend on the PLIC case of this interface cell, which changes equation 2.9 to:

$$\mathbf{F}_{\sigma,m} = \frac{1}{2}\sigma \sum_{i=1}^{n} (\mathbf{t}_{i,m} \times \mathbf{n}_i) \qquad (2.16)$$

In this equation m is the interface element of choice, i the neighboring interface elements and n the number of edges that depends on the PLIC reconstruction case of interface element m. Furthermore, there is no inherent connectivity between the different neighboring interface elements in the interface reconstruction. As a consequence, a certain neighboring cell i of cell m might not contain any gas, while the interface of cell m has an edge in the cell face connecting cell i and m. This will lead to no tensile force at this edge, because the normal in cell i is not defined. To the best of our knowledge, the use of the tensile force model in VoF has not been reported before.

In the used VoF model, three different surface tension models have been implemented: the CSF model, the height function model and the tensile force model. The CSF model is chosen because it is the most often used surface tension model. The height function model is the most often used improvement of the CSF model and therefore a good comparison for the new tensile force method.

2.4.3   Bubble advection

The bubble advection in the VoF model is slightly different from the FT method, because the exact location of the interface is not known. To enable an accurate advection of the bubble, the Piecewise Linear Interface Calculation (PLIC) algorithm is implemented in the code. In the PLIC algorithm, the interface of the bubble is represented as a flat plane using the normal and the phase fraction in the cell. For a 3D-simulation, 64 different cases are necessary to represent all different planes. By interchanging co-ordinate directions, changing of direction, and interchanging the phases, the 64 cases can be reduced to five cases, which are shown in figure 2.3.a. All these cases satisfy the following inequality:

$$\mathbf{n}_1 < \mathbf{n}_2 < \mathbf{n}_3 \qquad (2.17)$$

where n_i is the normal component in the three transformed co-ordinate directions. Using
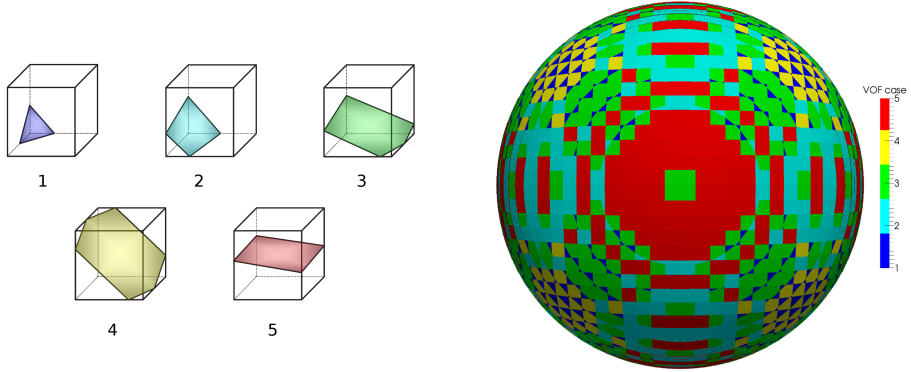
Figure 2.3: The five generic interface cases of the Piecewise Linear Interface Calculation in figure a. In figure b, a bubble is reconstructed using these 5 generic cases.

the five generic cases, all bubbles can be visualized as shown in figure 2.3.b. All bubbles depicted in this thesis are visualized in this way. The linear planes can be used to determine the fractional amount of liquid that is advected trough the cell phase using equation 2.1. This geometrical advection method is similar to the method of Youngs (1982), which has been adopted for the use of 3D domain.

2.5 Verification results

The implementation of the models was verified using three different tests. The implementations of the surface tension model, the advection scheme and the interaction between the momentum equations and the surface tension model are tested. Each test was performed for both the VoF model and FT model, using all available surface tension models.

2.5.1 Stationary bubble test

The implementation of the surface tension model was verified using a stationary bubble test. In this test, a spherical bubble is placed in a zero-gravity field. When the force balance on the bubble is solved analytically, the Laplace pressure is obtained:

$$\Delta p = \frac{4\sigma}{d} \tag{2.18}$$

The pressure jump across the interface, Δp, depends on the surface tension, σ, and the diameter of the bubble, d.

The test is performed for a box of five times the bubble diameter in all co-ordinate directions. The bubble is placed in the middle of the domain. The test is performed with air bubbles in two different fluids (σ equal to 0.073 N/m and 0.1 N/m). All the simulations are performed with 20 grid cells across the bubble diameter. Table 2.1 shows the deviation of

the pressure jump from the analytical solution. Furthermore, the intensity of the spurious currents in the simulation is characterized by the Capillary number, equation 2.19.

$$\text{Ca} = \frac{\mu_l \mathbf{v}_{max,l}}{\sigma} \tag{2.19}$$

The error in the pressure jump is smallest for the FT model, as expected. For the VoF model, the CSF surface tension model shows the smallest difference for the cases with a relatively high surface tension coefficient and large diameters (cases 3-5). However, when the surface tension coefficient increases or the bubble diameter decreases, the tensile force method determines the pressure jump over the interface more accurately than the other models. The obtained pressure jump is closer to the analytical value than the results obtained by the 3D CSF VoF methods (Brackbill et al., 1992; Meier et al., 2002; van Sint Annaland et al., 2005; Albadawi et al., 2013), while the results for the tensile force method and the height function model are comparable to the results obtained using 3D CLSVoF (Albadawi et al., 2013), 3D height function VoF (Lin et al., 2012), 3D FT (Dijkhuizen et al., 2010b) and the 2D CSF methods of Gerlach et al. (2006). Only the 2D PROST resulted in a pressure jump that is much closer to the analytical pressure jump, but there are no results available for the 3D PROST model (Gerlach et al., 2006).

Besides the error in the Laplace pressure and the capillary number, the table also shows the Ohnesorge number, equation 2.20.

$$\text{Oh} = \frac{\mu_g}{\sqrt{\rho_g \sigma d_b}} \tag{2.20}$$

Both the Ohnesorge number and the capillary number show no correlation with the deviation with respect to the Laplace pressure, which might be caused by the non-stationary nature of the pressure. However, the capillary number shows that the spurious currents in the VoF model are largest when the CSF model is used. Although the spurious currents are reduced the most using the height function model ($O(10^2 - 10^3)$ compared to $O(10^1 - 10^2)$ for the tensile force method), the calculated pressure is constantly increasing with time. While in the tensile force method the calculated pressure has a sinusoidal shape around the Laplace pressure.

2.5.2   Standard advection test

In the standard advection test, the implementation of the advection scheme in the model is verified. In this test, a spherical bubble is placed in a rotational velocity field according to equation 2.21.

$$\mathbf{u}\left(x, y, z\right) = \left(0, -\frac{2}{n_y \Delta y} \sin^2\left(\pi y\right) \sin\left(\pi z\right) \cos\left(\pi z\right), \frac{2}{n_z \Delta z} \sin^2\left(\pi z\right) \sin\left(\pi y\right) \cos\left(\pi y\right)\right)$$
$$\tag{2.21}$$

Table 2.1: The error, ϵ, in the Laplace pressure for the VoF model, using the CSF surface tension model (CSF), the height function surface tension model (HF) and the tensile force surface tension model (TF), and the FT model after 1000 time steps.

Case	d mm	σ N/m	$\Delta p_{analytical}$ Pa	Oh	Ca_{CSF}	ϵ_{CSF} %	Ca_{HF}	ϵ_{HF} %	Ca_{TF}	ϵ_{TF} %	Ca_{FT}	ϵ_{FT}
1	2.0	0.10	200.0	$2.2\cdot10^{-2}$	$1.8\cdot10^{-3}$	0.81	$3.9\cdot10^{-5}$	0.59	$1.4\cdot10^{-3}$	1.10	$2.7\cdot10^{-3}$	0.01
2	4.0	0.10	100.0	$1.6\cdot10^{-2}$	$2.8\cdot10^{-3}$	0.49	$4.7\cdot10^{-5}$	0.52	$1.5\cdot10^{-3}$	0.28	$5.2\cdot10^{-3}$	0.01
3	6.0	0.10	66.7	$1.3\cdot10^{-2}$	$3.2\cdot10^{-3}$	1.05	$8.8\cdot10^{-5}$	0.49	$1.8\cdot10^{-3}$	0.27	$2.9\cdot10^{-2}$	0.01
4	8.0	0.10	50.0	$1.1\cdot10^{-2}$	$2.8\cdot10^{-1}$	0.19	$8.9\cdot10^{-5}$	0.47	$2.4\cdot10^{-3}$	0.24	$7.8\cdot10^{-3}$	0.01
5	10	0.10	40.0	$1.0\cdot10^{-2}$	$4.5\cdot10^{-2}$	0.13	$6.9\cdot10^{-5}$	0.46	$1.2\cdot10^{-2}$	0.05	$7.0\cdot10^{-3}$	0.01
6	4.0	0.073	73.0	$9.4\cdot10^{-4}$	$3.7\cdot10^{-3}$	11.00	$1.7\cdot10^{-5}$	1.68	$3.5\cdot10^{-4}$	1.20	$4.6\cdot10^{-4}$	0.01
7	6.0	0.073	48.7	$7.7\cdot10^{-4}$	$1.2\cdot10^{-3}$	10.45	$3.1\cdot10^{-4}$	1.17	$3.0\cdot10^{-4}$	0.69	$4.0\cdot10^{-4}$	0.01
8	8.0	0.073	36.5	$6.6\cdot10^{-4}$	$2.2\cdot10^{-3}$	7.32	$2.2\cdot10^{-5}$	0.84	$2.7\cdot10^{-4}$	0.32	$4.0\cdot10^{-4}$	0.01
9	10	0.073	29.2	$6.0\cdot10^{-4}$	$4.7\cdot10^{-3}$	4.14	$1.6\cdot10^{-5}$	0.68	$2.2\cdot10^{-4}$	0.62	$3.6\cdot10^{-4}$	0.01

Table 2.2: The simulation settings for the standard advection test.

Property	Value	Unit
Domain size (nx,ny,nz)	$(120, 120, 120)$	grid cells
Grid size (Δx, Δy & Δz)	$0.005...0.015$	m
Time step	$1 \cdot 10^{-3}$	s
Courant criterion	$0.33...0.04$	-

The bubble, with a diameter of $\frac{1}{4}$ of the domain, is placed at $(\frac{1}{2}, \frac{1}{2}, \frac{3}{4})$ of the domain. When the front of the bubble has completed a single rotation, the direction of the velocity field is reversed. If the advection method is working properly, the bubble should return to its original position and shape. The difference between the original and the final state of the bubble is quantified by two errors: the mass error (equation 2.22) and the geometrical error (equation 2.23).

$$E_m = \frac{\sum_{i,j,k}(1 - F^{i,j,k})^{\text{end}} - \sum_{i,j,k}(1 - F^{i,j,k})^{\text{initial}}}{\sum_{i,j,k}(1 - F^{i,j,k})^{\text{initial}}} \tag{2.22}$$

$$E_g = \frac{\sum_{i,j,k}|(1 - F^{i,j,k})^{\text{end}} - (1 - F^{i,j,k})^{\text{initial}}|}{\sum_{i,j,k}(1 - F^{i,j,k})^{\text{initial}}} \tag{2.23}$$

The simulation settings for this test are shown in Table 2.2.

As expected, all surface tension models for the VoF method give the same results for the standard advection test, because the advection scheme is not changed when a different surface tension model is used. The mass error in all the VoF models and the FT model is respectively $\sim 10^{-9}$ and $\sim 10^{-13}$, which is negligible. The geometrical errors (see figure 2.4) obtained in these simulations are similar to the results obtain by the FT model of van Sint Annaland et al. (2006) and other VoF models (Rider and Kothe, 1998; Aulisa et al., 2003; van Sint Annaland et al., 2005). Although the geometrical error can be further reduced by refining the grid, we only present the results for a bubble with 30 grid cells per diameter, because this is the smallest grid used for simulations of moving bubbles.

2.5.3 Oscillating bubble test

Besides the implementation of the surface tension and the bubble advection, the interchange between the surface tension and the momentum equations is checked with the oscillating bubble test. In this test, a non-spherical bubble is placed in a zero-gravity field. The bubble has the same diameter in the x- and y-direction, while it is slightly elongated in the z-direction. At the beginning of the simulation the bubble is released and starts to oscillate
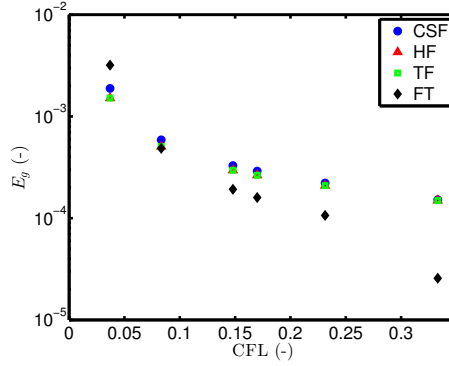
Figure 2.4: Geometrical error of the standard advection test for all models with respect to the Courant-Friedrichs-Lewy (CFL) number. The geometrical error is calculated with equation 2.23.

Table 2.3: The simulation settings for the oscillating bubble test.

Property	Value	Unit
Domain size (nx,ny,nz)	$(120, 120, 120)$	grid cells
Grid size (Δx, Δy & Δz)	$6.67 \cdot 10^{-4}$	m
Bubble diameter	$(0.04, 0.04, 0.02)$	m
Bubble placement	$\left(\frac{1}{2}, \frac{1}{2}, \frac{1}{2}\right)$	
Time step	$1 \cdot 10^{-4}$	s
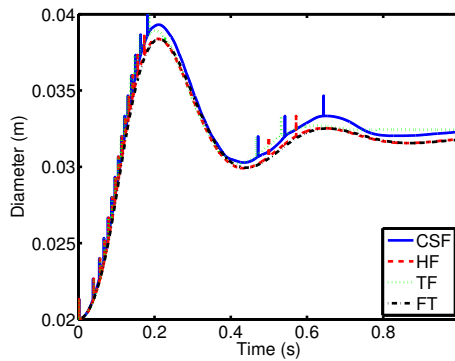
Figure 2.5: The results for the oscillating bubble test. The bubble diameter in the vertical direction is shown for the FT model and the VoF model with the CSF model, the height function model and the tensile force method.

until it reaches its equilibrium spherical shape. For small deformations, this problem can be solved analytically (Lamb, 1932). The FT model shows a very good agreement with the analytical solution of Lamb (1932) for small deformations (Roghair et al., 2011). However, these small deformations are not well captured in the VoF model, due to use of the generic 5 interfaces in the interface reconstruction. Consequently a larger deformation is used to verify the VoF models using the same settings as van Sint Annaland et al. (2006), which are given in table 2.3.

The results of this test are shown in Figure 2.5. The CSF model performs worst of the surface tension models, while the height function model is the best performing model. The tensile force model only improves the results slightly compared to the CSF model. There are no reports of the oscillating bubble test for VoF models in literature. Furthermore, all the VoF models show minor oscillations in the main trend, that are caused by the diameter calculation, which depends on the interface reconstruction.

2.6   Validation results

Besides verifying the code, the code is also validated with experimental results for single rising bubbles. Grace determined the size and terminal rise velocity for single freely rising bubbles. The results of these experiments are combined in the well known "Grace diagram", figure 2.6 (Grace, 1973; Grace et al., 1976; Clift et al., 1978). Because the graphical Grace diagram is only partly reported as correlations (Grace et al., 1976), Tomiyama (1998) developed correlations for pure liquids matching the Grace diagram in the wobbling, ellipsoidal, spherical cap and skirted bubble regimes. However, the correlations of Tomiyama (1998) differ largely from the Grace diagram for spherical and dimpled ellipsoidal-cap bubbles.

The Grace diagram is often used for the validation of gas-liquid DNS models, as shown in figure 2.6. All the authors observe a good comparison between the Grace diagram and the experimental results. Although the combined results span the industrial relevant area of the Grace diagram, there are only a few models that have been used to simulate the entire industrial relevant area. In this work, the code is validated with 33 single bubble simulations, which are depicted by the numbered dots in figure 2.7. Because the FT code has been validated by Dijkhuizen et al. (2010a) before, the validation was only performed for all the surface tension models included in the VoF model. All simulations are performed starting with a single stationary spherical bubble. The simulation settings are given in table 2.4. Furthermore, on all domain boundaries free-slip boundary conditions are applied and the window shifting principle is applied to keep the bubble at its initial position (at $(\frac{1}{2}, \frac{1}{2}, \frac{2}{3})$ of the domain) (Deen et al., 2004).

Figure 2.7 shows, besides the used settings for the single bubble simulations and the expected dimensionless terminal rise velocity, the obtained and expected shape of the bubbles. The obtained bubble shape is visualized using the interface segments created with the PLIC-advection algorithm. First of all, the obtained bubble shapes are compared. All the models are able to predict the shape of ellipsoidal and dimpled bubbles accurately.
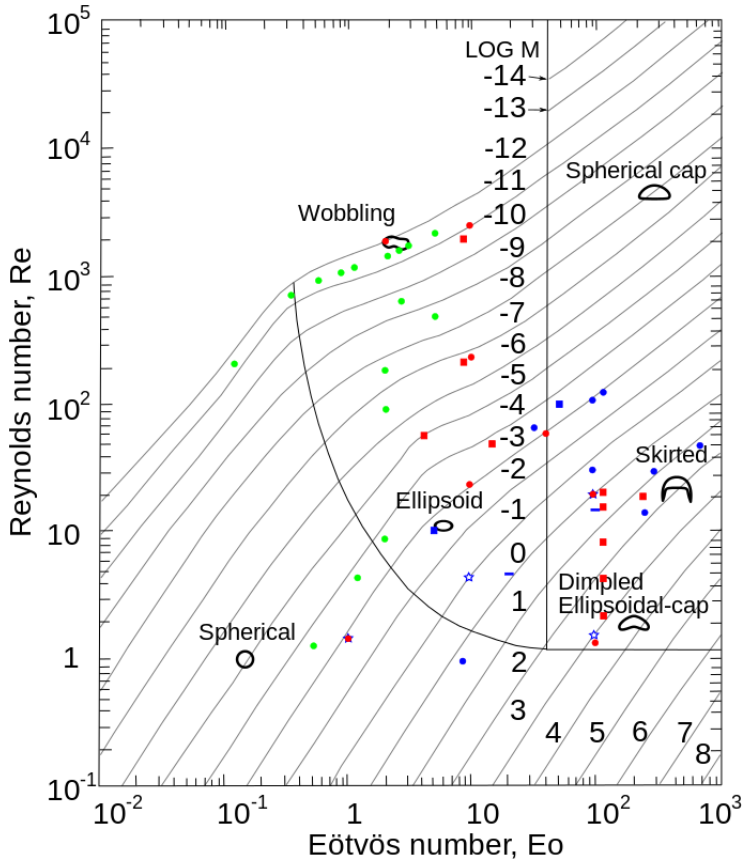
Figure 2.6: The Grace diagram showing the terminal rise velocity and bubble shape of single rising bubbles in a initial quiescent liquid as a function of the Eötvös and Morton number. 3D single bubble simulation already performed for the FT ●(blue: Hua and Lou (2006), red: van Sint Annaland et al. (2006) and green: Roghair et al. (2013b)), Level-Set ■ (red: Nagrath et al. (2005) and blue: Yu and Fan (2008)), Lattice Boltzmann − (Kurtoglu and Lin, 2006) and VoF ★ (van Sint Annaland et al., 2005; Lin et al., 2012). All authors show good comparison with the Grace diagram of Grace et al. (1976).
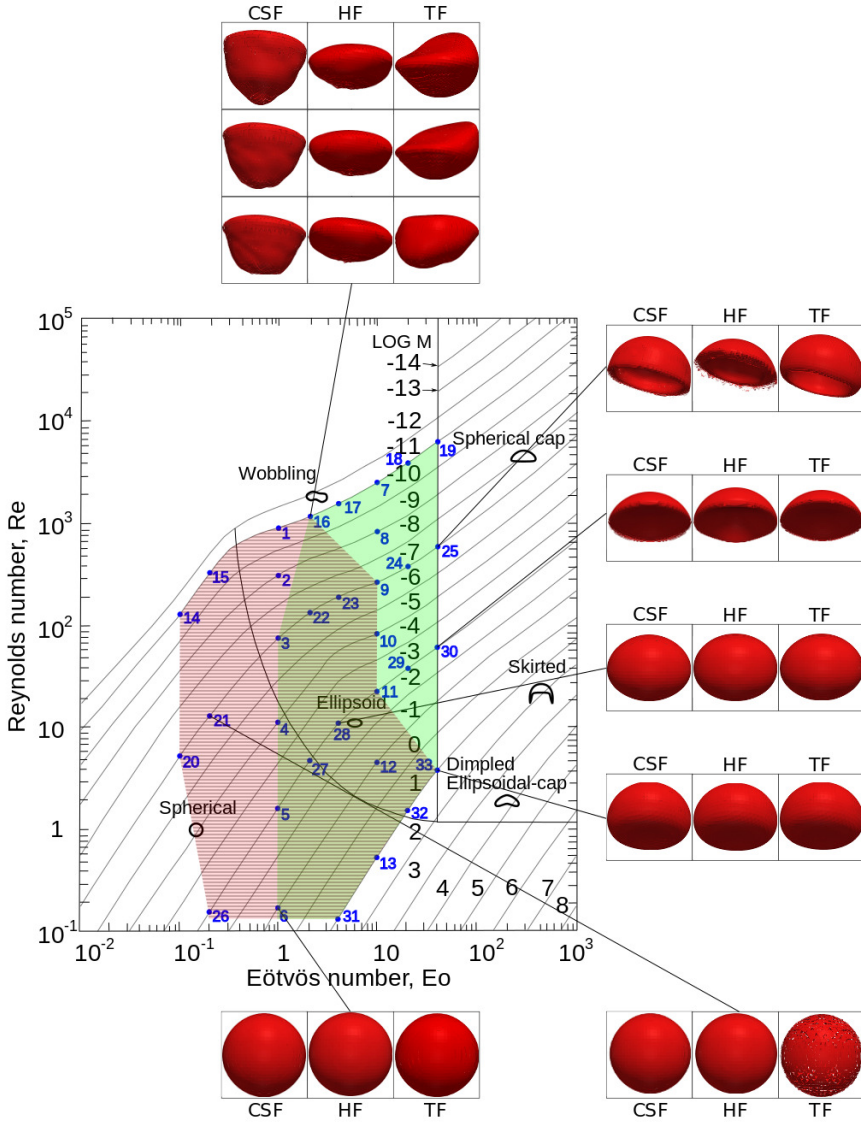
Figure 2.7: The single bubble simulations performed for validating the VoF model. The figure also shows the shape of the bubbles at terminal rise velocity for cases 6, 16, 21, 25, 28, 30 and 33. The red striped area depicts the region in which the height function model performs best. In the green area the tensile force model is the best performing model.

Table 2.4: The simulation settings for the single bubble simulations depicted by the numbers in Figure 2.7.

Property	Value	Unit
Bubble diameter	1.0...5.5	mm
Bubble diameter	30	grid cells
Initial bubble shape	spherical	
Domain size	$(150, 150, 150)$	grid cells
Initial bubble position	$(75, 75, 100)$	grid cells
Grid size Δx, Δy & Δz	0.033...0.18	m
Time step	$1 \cdot 10^{-7}$ ... $1 \cdot 10^{-5}$	s
Eo	0.1...40	-
log Mo	-11...1	-

Comparing the cases of spherical bubbles (case 6 and 21), both the CSF model and the height function model show a good approximation of the bubble shape both for low and high Eötvös numbers (Eo). However, the tensile force method shows a large difference in the representation of the bubble surface; connectivity between the interface segments is lost for case 21. This behavior was observed for all bubbles with Eo < 1. The reason can be found looking at the stationary bubble test of simulations with Eo < 1 and Eo > 1 (case 26 and 31). Although Eo is different for these cases, the Reynolds numbers of these cases are similar. The stationary bubble test of case 26 has 10 times higher error in the pressure jump. Furthermore, the spurious currents are larger in case 26 with respect to case 31, respectively 10^{-4} m/s and 10^{-12} m/s. These increased spurious currents will lead to a deterioration of the connectivity and thus a less accurate calculation of the surface tension in the cases in which Eo < 1.

For the case of a wobbling bubble (case 16), three (uncorrelated) screen shots are shown in figure 2.7. Comparing the three surface tension models with each other, there is a large difference between the predicted shape of the bubbles, which is possible for a wobbling bubble. Nevertheless, the CSF and height function model show almost no change in shape over time. Only the tensile force method shows clear (realistic) shape changes during the simulation. The tensile force method thus predicts the shape deformation of the bubble most accurately for wobbling bubbles.

Finally, there are also some differences in the representation of the spherical cap bubbles (case 25). Both the CSF model and the height function model show a very thin skirt, which is shedding in the simulation. The bubble size will thus decrease during the simulation, which reduces Eo. Only the tensile force method shows the spherical cap bubble shape as reported (Grace, 1973; Grace et al., 1976). The skirt of the tensile force methods are about 1 grid cell wide. Consequently the representation of the bubble shape will increase when the resolution is increased. However, the bubble rise velocity is not expected to change with

this increase in resolution.

Besides the shape, the terminal rise velocity of the bubbles was also determined and the results for all bubbles are listed in table 2.5. The results for the different surface tension models are compared to the experimental results of Grace et al. (1976) and the correlation for pure liquids of Tomiyama (1998), equation 2.24.

$$C_D = \frac{4d_b(\rho_l - \rho_g)g}{3\rho_l \mathbf{v}_{b,z}^2} = max \left\langle min \left[\frac{16}{\mathrm{Re}} \left(1 + 0.15\mathrm{Re}^{0.687} \right), \frac{48}{\mathrm{Re}} \right], \frac{8}{3} \frac{\mathrm{Eo}}{\mathrm{Eo} + 4} \right\rangle \quad (2.24)$$

The obtained Reynolds numbers are calculated on basis of the time averaged rise velocity. The simulations were stopped when the moving average of the bubble velocity is within 0.5 % of the final value for at least 0.2 s. To eliminate start-up effects the first 0.1 to 0.2 s are not included in the average.

The results for simulations with the tensile force method for Eo < 1 are not shown in the table, because the model has problems with the connectivity of the interface elements. This results in a zero bubble rise velocity. The table also shows that either the height function model or the tensile force method are performing better or similar compared to the CSF model of Brackbill et al. (1992). From the table and the shown bubble shapes, the best performing model for each case can be determine, which are represented in figure 2.7. In figure 2.7, three regions are observed. In the region Eo < 1 the best performing model is the height function model, because the tensile force method has a problem with the connectivity between the interface segments in this region. While in the region with Eo > 10 the tensile force method is the best performing model, which can be explained by the relatively large stencil needed in calculation of the height. Therefore, the height function model will have a decreased accuracy when two interfaces of the same bubble are within 4 grid cells, which occurs especially for dimpled and spherical cap bubbles. In the region $1 \leq \mathrm{Eo} \leq 10$, the height function model and the tensile force method perform similarly.

Although the Eötvös number has a large effect on the accuracy of the surface tension models, the effect of the Morton number, Mo, is much smaller. Figure 2.7 shows that there are deviations from the main trends in the accuracy only at very high Mo (log Mo ≥ 1) and low Mo (log Mo < −7). At high Mo, the height function model is also able to accurately simulate bubbles with Eo > 10. While at low Mo, the accuracy of both models is decreased. Therefore, the height function model can only be used when Eo ≤ 2 and the tensile force method when Eo ≥ 2.

2.7   Conclusions

In this chapter, the main characteristics of the FT and VoF model were discussed. The existing VoF model was extended with two new surface tension models: the height function method and the tensile force model. Furthermore, a pressure jump correction model was implemented to eliminate the errors which arise due to mismatches in discretisation of the surface tension and the pressure.

Table 2.5: All the simulated Reynolds numbers using the CSF model, the height function model (HF) and the tensile force method (TF) compared to the experimental results as obtained from the Grace diagram (Grace et al., 1976) (G) and the correlation of Tomiyama (1998) (T).

case	Eo	$log(\mathrm{Mo})$	G	T	CSF	HF	TF
1	1	-11	$9.3\cdot10^2$	$8.8\cdot10^2$	$9.7\cdot10^2$	$9.7\cdot10^2$	$7.1\cdot10^2$
2	1	-9	$3.2\cdot10^2$	$2.8\cdot10^2$	$3.5\cdot10^2$	$3.2\cdot10^2$	$3.4\cdot10^2$
3	1	-7	$8.0\cdot10^1$	$8.9\cdot10^1$	$8.1\cdot10^1$	$7.9\cdot10^1$	$8.0\cdot10^1$
4	1	-5	$1.3\cdot10^1$	$2.8\cdot10^1$	$1.5\cdot10^1$	$1.4\cdot10^1$	$1.5\cdot10^1$
5	1	-3	1.8	8.9	2.0	2.0	2.0
6	1	-1	$1.8\cdot10^{-1}$	2.8	$2.2\cdot10^{-1}$	$2.1\cdot10^{-1}$	$1.9\cdot10^{-1}$
7	10	-11	$2.8\cdot10^3$	$2.6\cdot10^3$	$2.2\cdot10^3$	-	$2.3\cdot10^3$
8	10	-9	$9.0\cdot10^2$	$8.3\cdot10^2$	-	$7.3\cdot10^2$	$7.4\cdot10^2$
9	10	-7	$2.9\cdot10^2$	$2.6\cdot10^2$	-	$2.3\cdot10^2$	$2.3\cdot10^2$
10	10	-5	$9.0\cdot10^1$	$8.3\cdot10^1$	$8.0\cdot10^1$	$7.8\cdot10^1$	$8.1\cdot10^1$
11	10	-3	$2.4\cdot10^1$	$2.6\cdot10^1$	$2.3\cdot10^1$	$2.3\cdot10^1$	$2.2\cdot10^1$
12	10	-1	5.0	8.3	4.8	4.9	4.9
13	10	1	$6.0\cdot10^{-1}$	2.6	$6.6\cdot10^{-1}$	$6.6\cdot10^{-1}$	$6.6\cdot10^{-1}$
14	0.1	-11	$1.4\cdot10^2$	$4.5\cdot10^2$	$2.6\cdot10^2$	$2.5\cdot10^2$	–
15	0.2	-11	$3.8\cdot10^2$	$5.4\cdot10^2$	$4.3\cdot10^2$	$4.4\cdot10^2$	–
16	2	-11	$1.2\cdot10^3$	$1.2\cdot10^3$	$1.1\cdot10^3$	$1.3\cdot10^3$	$1.3\cdot10^3$
17	4	-11	$1.7\cdot10^3$	$1.6\cdot10^3$	$1.6\cdot10^3$	-	$1.7\cdot10^3$
18	20	-11	$4.1\cdot10^3$	$4.1\cdot10^3$	$3.8\cdot10^3$	$3.7\cdot10^3$	$3.7\cdot10^3$
19	40	-11	$7.0\cdot10^3$	$6.6\cdot10^3$	$5.8\cdot10^3$	$5.9\cdot10^3$	$5.8\cdot10^3$
20	0.1	-7	4.6	$4.5\cdot10^1$	5.8	5.5	–
21	0.2	-7	$1.4\cdot10^1$	$5.4\cdot10^1$	$1.4\cdot10^1$	$1.4\cdot10^1$	–
22	2	-7	$1.4\cdot10^2$	$1.2\cdot10^2$	$1.3\cdot10^2$	$1.3\cdot10^2$	$1.3\cdot10^2$
23	4	-7	$2.1\cdot10^2$	$1.6\cdot10^2$	-	$1.9\cdot10^2$	$1.9\cdot10^2$
24	20	-7	$4.0\cdot10^2$	$4.1\cdot10^2$	$3.8\cdot10^2$	$3.7\cdot10^2$	$3.8\cdot10^2$
25	40	-7	$7.2\cdot10^2$	$6.6\cdot10^2$	$5.9\cdot10^2$	$5.9\cdot10^2$	$5.7\cdot10^2$
26	0.2	-3	$1.6\cdot10^{-1}$	5.4	$2.0\cdot10^{-1}$	$1.9\cdot10^{-1}$	–
27	2	-3	4.9	$1.2\cdot10^1$	5.0	4.9	5.1
28	4	-3	$1.1\cdot10^1$	$1.6\cdot10^1$	$1.1\cdot10^1$	$1.1\cdot10^1$	$1.1\cdot10^1$
29	20	-3	$3.9\cdot10^1$	$4.1\cdot10^1$	$3.5\cdot10^1$	$3.5\cdot10^1$	$3.6\cdot10^1$
30	40	-3	$6.5\cdot10^1$	$6.6\cdot10^1$	$6.0\cdot10^1$	$5.9\cdot10^1$	$6.0\cdot10^1$
31	4	1	$1.4\cdot10^{-1}$	1.6	$1.7\cdot10^{-1}$	$1.7\cdot10^{-1}$	$1.7\cdot10^{-1}$
32	20	1	1.6	4.1	10.2	1.6	1.6
33	40	1	3.0	6.6	3.7	3.7	3.8

The implemented surface tension models for the VoF model were verified and compared with the FT model. The verification results show that the CSF model of Brackbill et al. (1992) is not able to calculate the surface tension accurately. The height function model and the tensile force method perform similar as the FT model.

The VoF model was also validated using 33 different cases in the industrially relevant region of the Grace diagram (Grace, 1973; Grace et al., 1976). Generally, the height function model is the best performing model in the region with $Eo < 1$ and the tensile force method is the best performing model in the region with $Eo > 10$. In the region $1 \leq Eo \leq 10$, the height function and the tensile force method perform equally well.

Fluid-Solid Direct Numerical Simulation Models

3.1 Introduction

To describe the interaction between bodies immersed in a fluid, several powerful Direct Numerical Simulation (DNS) models have become available in the last decade. Similar to the gas-liquid DNS models, fluid-solid models can be divided in body conforming grid models and fixed grid models (Deen and Kuipers, 2014). In the first class of models, the grid conforms with the shape of the solid object, which enables a straightforward application of the no-slip boundary condition at the surface of the solid body. To enable the calculation of the flow in the domain all the governing equations need to be transformed to incorporate the grid geometry in the discrete representation of the equations. An example of a body conforming grid method is the Arbitrary Lagrangian-Eulerian (ALE) technique. In this technique, a moving unstructured finite element mesh is employed, which is refined around the particles (Hu et al., 1992; Hu, 1996; Deen et al., 2012). The advantage of this method is the easy implementation of the no-slip boundary condition at the particle surface. However, the creation of a body conforming grid is a complicated procedure particularly for non-spherical particles and dense arrays of particles. Moreover, if the particle moves, the grid needs to be remeshed every time step (Mittal and Iaccarino, 2005; Uhlmann, 2005).

Chesshire and Henshaw (1990) and Henshaw and Schwendeman (2003) improved these type of methods by combining the body conforming grids for every particle and a fixed Eulerian grid in the overset grid method. The information between the grids is exchanged

by interpolation. The combination of the two grids enables an accurate calculation of the flow around the objects, while a coarse Eulerian grid can be used for the background flow. As a consequence significant savings in computational time can be achieved. However, the implementation of the interpolation between the grids is complex. Furthermore, when the particles come close to each other, the interpolation procedures become complicated. (Deen et al., 2012). Because moving particles are used in this work, a fixed grid method is chosen to model the fluid-solid interactions.

A popular fixed grid method is the Immersed Boundary (IB) method, because the method combines a flexible implementation for either static or moving particles with a simple and efficient fixed grid solver (Peskin, 2002; Mittal and Iaccarino, 2005; Deen and Kuipers, 2013, 2014; Deen et al., 2014). There are two main classes of IB methods: the continuous force method and the direct force method. The continuous force method was developed by Peskin (1977). In this method, two sets of Lagrangian markers are used to track the motion of the solid body and to the fluid motion in the direct vicinity of the solid body. The difference in the positions of the markerpoints is used to evaluate the interaction force. This interaction force is distributed to the Eulerian grid using a Dirac function and is implemented as an explicit source term in the Navier-Stokes equations. Because of the explicit nature of the source term, the method has constraints regarding stability (Peskin, 2002; Mittal and Iaccarino, 2005; Uhlmann, 2005; Deen et al., 2012; Kempe and Fröhlich, 2012; Deen and Kuipers, 2013; Deen et al., 2014).

In the direct forcing methods, the no-slip boundary condition is implemented at the Lagrangian force points at the particle surface. This enables a sharp representation of the solid boundaries and prevents stability issues. However, the implementation of the movement of the solid body is slightly more complex and the interpolation between the Eulerian and the Lagrangian grid can lead to force oscillations (Mittal and Iaccarino, 2005; Deen et al., 2012; Kempe and Fröhlich, 2012; Deen and Kuipers, 2013; Deen et al., 2014). More information on the different kinds of direct forcing IB methods can be found in Mittal and Iaccarino (2005).

A new direct forcing method is the second order implicit IB method of Deen et al. (2012). The advantage of this method in comparison with the other direct forcing methods is that this method uses a second order fit to incorporate the no-slip boundary condition at the fluid-solid interface. In other methods either lower order linear fits or higher order multidimensional fits are used, which lead respectively to a lower accuracy or a larger stencil (Deen et al., 2014).

Uhlmann (2005) combined the advantages of both the continuous force and the direct force IB methods, by using the interchange of information between the grids from the former and the local calculation of the fluid-solid interaction force from the latter. In the Uhlmann method, the presence of the solid boundary is represented as a source term in the Navier-Stokes equations. To calculate the source term, force points are placed on the surface of the object. The source term is calculated for all these force points and distributed to the Eulerian mesh using a delta function (Deen et al., 2012; Kempe and Fröhlich, 2012).

Although the fluid inside the particle is freely moving, Uhlmann (2005) enforces a rigid body motion inside the particle to advect the particles to their new positions. Due to the rigid body motion assumption inside the particle, the method of Uhlmann (2005) only works properly for cases where the density of the body is larger than that of the surrounding fluid. Stability issues arise when the ratio between the density of the object and the density of the fluid is smaller than 1.2 (Kempe and Fröhlich, 2012). Therefore, Kempe and Fröhlich (2012) removed the rigid body motion assumption for the calculation of the motion of the particles.

Several alternative DNS methods for the simulation of immersed objects have been developed that are different from the body conforming methods and the described IB method. Kajishima and Takiguchi (2002) used a very simple method to simulate an immersed body. For all cells inside the solid body, the rigid body motion is enforced. The fluid and object velocity are nicely connected by the use of a combined velocity that is weighted according to the solids fraction inside a cell. The method is efficient, but strongly grid dependent. Moreover, the velocity is not divergence free around the solid object (Uhlmann, 2005).

The method of Zhang and Prosperetti (2005) is a semi-analytical method, which applies the Stokes flow approximation in the vicinity of the particle. The analytical solution is coupled to the solution of the full Navier-Stokes equations using an iterative procedure. The method attains a relative high accuracy at low resolutions. However, the analytical solutions based on spherical harmonics, which is used to represent the Stokes flow near the particle, can only be used for relatively simple geometrical shapes (Uhlmann, 2005; Deen et al., 2012, 2014).

The Distributed Lagrangian Multiplier/Fictitious Domain method, which was developed by Glowinski et al. (2001), introduces the solid body motion of the immersed objects via Lagrangian multipliers in the combined momentum equations. The coupling between the phases is fully implicit and is therefore solved in an iterative manner (Uhlmann, 2005; Deen et al., 2012, 2014).

Finally, the Lattice Boltzmann method can be used to solve the interactions between immersed objects and the fluid. As opposed to the previously discussed methods, the method solves the approximate Boltzmann equations on a lattice, enforcing the no-slip condition via the so-called "bounce-back" rule. This method is especially attractive for simulating many immersed objects, because there is no remeshing required. However, the introduction of the "bounce-back" rule results in a step-wise representation of the interface of the object. Besides, when the object is moving, its representation changes over time (Feng and Michaelides, 2005; Deen et al., 2012, 2014). To improve the interface representation, Feng and Michaelides (2005) combined the Lattice Boltzmann method with the direct forcing IB method.

In this thesis, two different fluid-solid Direct Numerical Simulation models are compared: the modified Uhlmann method of Kempe and Fröhlich (2012), which will be called the first order explicit IB method, and the second order implicit IB method of Deen et al. (2012). This chapter will start with the governing equations of the models. Subsequently,

the fluid-solid coupling and the advection of the objects for both methods is described. The verification and validation of both methods is presented in the following sections.

3.2   Governing equations

Although there are differences between the implementation of the fluid-solid coupling and the calculation of the particle advection for the first order explicit IB method and the second order implicit IB method, the governing equations of the two models are the same. Accordingly, this section will discuss the main characteristics of both models. The first order IB method is based on the implementation of Kempe and Fröhlich (2012), while the second order IB method is based on the implementation of Deen et al. (2012).

In both IB methods, the continuity equation, equation 3.1, and the Navier-Stokes equations, equation 3.2, are solved for incompressible flow with non-constant viscosity.

$$\nabla \cdot \mathbf{u} = 0 \tag{3.1}$$

$$\rho \frac{\partial \mathbf{u}}{\partial t} = -\nabla p - \rho \nabla \cdot (\mathbf{u}\mathbf{u}) - \nabla \cdot \boldsymbol{\tau} + \rho \mathbf{g} \tag{3.2}$$

The no-slip boundary condition at the solid surface is introduced in these equations via the fluid-solid interactions, which differs for both models and will therefore be discussed in the following sections.

The velocity field is calculated using a projection-correction method. In the projection step, a prediction of the velocity field is calculated from the Navier-Stokes equations. Except for the diffusion term, all terms in the Navier-Stokes equations are calculated explicitly. The diffusion term is treated semi-implicitly, choosing the implicit part such that all velocity components can be calculated separately whereas the remaining finite parts are treated explicitly. The diffusion term is discretised using a second order central difference scheme, while the discretisation of the convective terms is performed with a second order flux-delimited Barton scheme. Subsequently, the approximated velocity field is corrected to satisfy the continuity equation. The implicit part of the Navier-Stokes equations and the correction step are calculated with a ICCG block matrix solver, which has been parallelised with OpenMP.

When the new velocity field is known, the velocity of the object is updated using Newton's equation of motion. The velocity of object m consists of a translational velocity, $\mathbf{w}_m$, and a rotational velocity, $\boldsymbol{\omega}_m$, as shown in equation 3.3.

$$\mathbf{v}_m = \mathbf{w}_m + \boldsymbol{\omega}_m \times (\mathbf{r}_m - \mathbf{r}_{i,j,k}) \tag{3.3}$$

In this equation, $(\mathbf{r}_m - \mathbf{r}_{i,j,k})$ is the distance between a certain point in the object $\mathbf{r}_{i,j,k}$ and the center of mass of the object $\mathbf{r}_m$. After the new velocities of all objects have been
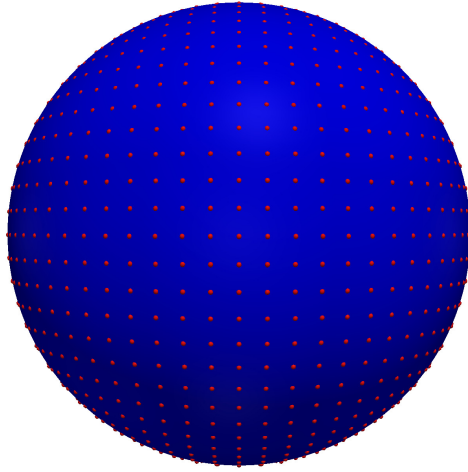
Figure 3.1: Lagrangian representation of a particle in the first order explicit Immersed Boundary method. The red dots on the surface of the particle represent the force points on the particle.

obtained, they are moved to their new positions using an explicit Euler scheme. The inter-particle and the particle-wall interactions, that occur during the movement, are handled with a hard sphere model of Hoomans et al. (1996). Because the only freely moving particles in this work will be spherical particles, the discussions on the particle advection in the next sections will focus on spherical particles.

3.3   First order explicit Immersed Boundary method

In this section, the implementation of the fluid-solid interaction and the advection of particles is discussed for the first order explicit IB method.

3.3.1   The fluid-solid interaction

In the first order explicit IB method, the fluid-solid interaction is taken into account via a source term in the Navier-Stokes equations. To determine the force density needed in the Navier-Stokes equations, discrete force points are placed on the surface of the immersed object, as illustrated for a spherical particle in figure 3.1.

The force density at each force point is determined with an iterative procedure. First of all, the velocity field is approximated by solving the Navier-Stokes equations without any source term. The velocity at the force point, $\mathbf{U}_n$, can be determined by interpolation from

the Eulerian velocity field:

$$\mathbf{U}_n = \sum_i \sum_j \sum_k \delta \left(\frac{\mathbf{r}_i - \mathbf{R}_i}{h} \right) \delta \left(\frac{\mathbf{r}_j - \mathbf{R}_j}{h} \right) \delta \left(\frac{\mathbf{r}_k - \mathbf{R}_k}{h} \right) \mathbf{u}_{i,j,k} \qquad (3.4)$$

where, δ is the weighting function of Deen et al. (2004) and h the average grid size. The capital letters in the function represent the values at the force points while the lower case symbols represent the values at the Eulerian grid points. Using the difference between the interpolated velocity $\mathbf{U}_n$ and the velocity of the force point $\mathbf{v}_m$ calculated with equation 3.3, a first estimate of the force density at the force point is computed from:

$$\mathbf{F}_{IB,n} = \mathbf{F}_{IB,n} + \frac{\rho_f}{\Delta t} \left(\mathbf{v}_m - \mathbf{U}_n \right) \qquad (3.5)$$

Subsequently, the local force density, $F_{IB,n}$, is mapped to the Eulerian grid by:

$$\mathbf{f}_{IB,(i,j,k)} = \sum_m \delta \left(\frac{\mathbf{r}_i - \mathbf{R}_i}{h} \right) \delta \left(\frac{\mathbf{r}_j - \mathbf{R}_j}{h} \right) \delta \left(\frac{\mathbf{r}_k - \mathbf{R}_k}{h} \right) \mathbf{F}_{IB,n} \frac{\Delta V_m}{h^3} \qquad (3.6)$$

This equation also uses the weighting function of Deen et al. (2004). The calculated force density is corrected for the volume associated with the force point, equation 3.7.

$$\Delta V_m = \frac{\pi}{3} h^3 (3(\frac{d}{h})^2 + 1) \qquad (3.7)$$

This estimate of the IB source term is used to calculate a new velocity field at the Eulerian grid. This procedure is repeated until the average difference of the interpolated velocity and the velocity according to equation 3.3 is within a preset margin or when a maximum number of iterations is reached.

Because of the finite size of the mapping function stencil used to map the force density to the surrounding Eulerian grid cells, the object appears to be slightly larger to the fluid than the specified diameter on which the force points are placed. Especially at high volume fraction of the particles this leads to a substantial overestimation of the drag force, because in these cases the drag force has a strong non-linear dependence on the particle size. To resolve the slight increase in the particle diameter, the force points are placed on a computational particle that has a slightly smaller size than the real particle. The difference between the diameters of the real particle and the computational particle is tuned using the method of Ladd (1994), which ensures that the drag force matches analytical results that are available for low-Reynolds number cases. Because there are no analytical results at higher Reynolds numbers, high particle fractions nor for objects other than spherical particles, the application of this method for the latter cases is questionable. For these cases, the effective particle diameter is set equal to the real diameter (Tang et al., 2014).

3.3.2 Particle advection

When the velocity field of the fluid is known, the new velocity of the objects can be determined using Newtonian equations of motion. For spherical particle m the conservation laws for linear and angular momentum are respectively given by:

$$V_m \rho_m \frac{d\mathbf{w}_m}{dt} = \rho_f \oint_{\Gamma_m} (\boldsymbol{\tau} \cdot \mathbf{n}) dS + V_m (\rho_m - \rho_f) \mathbf{g} \tag{3.8}$$

$$I_m \frac{d\boldsymbol{\omega}_m}{dt} = \rho_f \oint_{\Gamma_m} (\mathbf{r}_{i,j,k} - \mathbf{r}_m) \times (\boldsymbol{\tau} \cdot \mathbf{n}) dS \tag{3.9}$$

where Γ_m is the surface of particle m, ρ_f is the density of the surrounding fluid, and $\mathbf{r}_m$ is the center of mass of the particle. The first terms on the right hand side of both equations represent respectively the forces and torque acting on the particle. The second term on the right hand side of the linear momentum equation is the buoyancy force. The moment of inertia of the particle, I_m, is given by:

$$I_m = \frac{1}{10} V_m \rho_i d_m^2 \tag{3.10}$$

Because the numerical evaluation of the surface integral in equations 3.8 and 3.9 is numerically difficult, Uhlmann (2005) applied Cauchy's stress principle to rewrite the equations. In this approach, the new particle velocity can be calculated with the applied immersed boundary force density, which includes the gravitational force acting on the particle. Nonetheless, the gravitational force acting on the particle should be corrected for the gravitational force on the internal fluid, which was included in the calculation of the flow field.

$$V_m \rho_m \frac{d\mathbf{w}_m}{dt} = \frac{d}{dt} \int_{\Omega_m} \rho_f \mathbf{u} dV - \rho_f \int_{\Omega_m} \mathbf{f}_{IB} dV + V_m (\rho_m - \rho_{if}) \mathbf{g} \tag{3.11}$$

$$I_m \frac{d\boldsymbol{\omega}_m}{dt} = \frac{d}{dt} \int_{\Omega_m} \rho_f (\mathbf{r}_{i,j,k} - \mathbf{r}_m) \times \mathbf{u} dV - \rho_f \int_{\Omega_m} (\mathbf{r}_{i,j,k} - \mathbf{r}_m) \times \mathbf{f}_{IB} dV \tag{3.12}$$

Uhlmann (2005) assumed a solid body force inside the particle to remove the time derivative from the equation. However, this assumption leads to numerical instabilities when the density ratio of the particle and the fluid is less than 1.2. To overcome these problems, Kempe and Fröhlich (2012) numerically evaluated the same time derivative using second order midpoint quadrature rules as given by equations 3.13 and 3.14.

$$\int_{\Omega_m} \rho_f \mathbf{u} dV = \sum_i \sum_j \sum_k \mathbf{u} V_{i,j,k} \phi_{i,j,k} \tag{3.13}$$

$$\int_{\Omega_m} \rho_f(\mathbf{r}_{i,j,k} - \mathbf{r}_m) \times \mathbf{u} dV = \sum_i \sum_j \sum_k (\mathbf{r}_{i,j,k} - \mathbf{r}_m) \times \mathbf{u} V_{i,j,k} \phi_{i,j,k} \tag{3.14}$$

In these equations, $\phi_{i,j,k}$ is the solids volume fraction in a cell, which is calculated by employing a signed distance level-set function (Kempe and Fröhlich, 2012). The time derivative is calculated using a simple forward Euler scheme.

3.4 Second order implicit Immersed Boundary method

3.4.1 The fluid-solid interaction

Because the second order implicit IB method is a direct forcing method, the implementation of the no-slip boundary condition is implicitly introduced in the Navier-Stokes equations. After discretisation, the Navier-Stokes equations can be written in the following compact form, which is the same for each velocity component ψ.

$$a_c \psi_c + \sum_{nb} a_{nb} \psi_{nb} = b_c \tag{3.15}$$

This equation expresses the velocity component of a node inside the fluid, ψ_c, as a function of the same velocity component of the neighboring nodes, ψ_{nb}, and the explicit terms, b. Because the equation is only valid for nodes outside the solid objects, it should be checked for each node whether it resides inside a particle. This should be done in such a way that the staggered configuration of the nodes for each velocity component is taken into account.

Considering a node in the fluid that has a neighboring node inside a particle, as shown in the top of figure 3.2, the no-slip boundary should be applied in the neighboring cell. To apply the no-slip boundary, a second order (1D) fit of the velocity component is considered. Using this fit, the velocity inside the particle, ψ_0, can be expressed as a function of the velocity at the objects surface, ψ_s, the velocity of the central cell, ψ_1, and the velocity component in the next cell, ψ_2:

$$\psi_0 = -\frac{2\zeta_s}{(1 - \zeta_s)}\psi_1 + \frac{\zeta_s}{(2 - \zeta_s)}\psi_2 + \frac{2}{(1 - \zeta_s)(2 - \zeta_s)}\psi_s \tag{3.16}$$

In this equation, ζ_s is the dimensionless distance between the grid point of the velocity component and the intersection of the grid line and the particle surface (see figure 3.2). For simple immersed objects (particles, cylinders and thin sheets), the determination of the intersection between the grid line and the particle surface can be determined analytically. Using equation 3.16, the coefficients of the central and neighboring cells are modified according to equations 3.17 to 3.20.
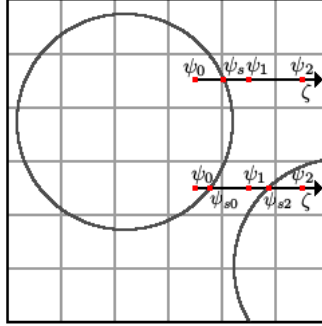
$$\tilde{a}_0 = 0 \tag{3.17}$$

Figure 3.2: The incorporation of the no-slip boundary in the second order implicit Immersed Boundary method. The incorporation of each velocity component, ψ, is different, because of the staggered grid. The top implementation is for a single particle, while the bottom accounts for two close particles.

$$\tilde{a}_1 = \tilde{a}_c = a_1 - \frac{2\zeta_s}{(1 - \zeta_s)} a_0 \tag{3.18}$$

$$\tilde{a}_2 = a_2 + \frac{\zeta_s}{(2 - \zeta_s)} a_0 \tag{3.19}$$

$$\tilde{b}_1 = \tilde{b}_c = b_1 - \frac{2\psi_s}{(1 - \zeta_s)(2 - \zeta_s)} a_0 \tag{3.20}$$

The second order fit becomes singular as $(1 - \zeta_s)$ approaches 0. For cases where the dimensionless distance to the surface ζ_s is larger than 0.9999, a first order fit is used, which is given by:

$$\psi_0 = -\frac{\zeta_s}{(2 - \zeta_s)} \psi_2 + \frac{2}{(2 - \zeta_s)} \psi_s \tag{3.21}$$

To ensure a complete implementation of the no-slip boundary condition, the above mentioned procedure should be performed for all the nodes surrounding an immersed object, for all velocity components.

A special treatment is followed for a central cell that is surrounded by two neighbors in the same direction that are inside an immersed object, as shown in the bottom of figure 3.2.

If the procedure described is followed, the first treated neighboring cell will end up with a non-zero coefficient in the matrix. To prevent this from happening, another second order fit was derived taking into account the velocity of both particles, which is given by equation 3.22.

$$\psi_0 = - \frac{\zeta_{s0}^2 \zeta_{s2} - \zeta_{s0} \zeta_{s2}^2}{\zeta_{s0}(1 - \zeta_{s0}[1 - \zeta_{s2}]) - \zeta_{s2}(1 - \zeta_{s2}[1 - \zeta_{s0}])} \psi_1$$
$$+ \frac{\zeta_{s2}^2 - \zeta_{s2}}{\zeta_{s0}(1 - \zeta_{s0}[1 - \zeta_{s2}]) - \zeta_{s2}(1 - \zeta_{s2}[1 - \zeta_{s0}])} \psi_{s0} \qquad (3.22)$$
$$+ \frac{\zeta_{s0}^2 - \zeta_{s0}}{\zeta_{s0}(1 - \zeta_{s0}[1 - \zeta_{s2}]) - \zeta_{s2}(1 - \zeta_{s2}[1 - \zeta_{s0}])} \psi_{s2}$$

This equation becomes singular when one of the two surfaces coincide with the central grid point. To remove the singularity, a first order approximation of the velocity is performed when one of the surfaces is closer than $0.0001 \Delta x$ from the central point. The first order approximation of the velocity is given by:

$$\psi_0 = \frac{\zeta_{s2}}{(\zeta_{s2} - \zeta_{s0})} \psi_{s0} - \frac{\zeta_{s0}}{(\zeta_{s2} - \zeta_{s0})} \psi_{s2} \qquad (3.23)$$

3.4.2 Particle advection

To enable the movement of particles, Newton's second law is also implemented for the second order implicit IB method. Because the immersed boundary force density is unknown for this method, the simplification of Uhlmann (2005) cannot be used in this method. For this method the second law of Newton is reformulated only slightly to equation 3.24 and 3.25

$$V_m \rho_m \frac{d\mathbf{w}_m}{dt} = \rho_f \oint_{\Gamma_m} (\boldsymbol{\tau} \cdot \mathbf{n} + p\mathbf{n})dS \qquad (3.24)$$

$$I_m \frac{d\boldsymbol{\omega}_m}{dt} = \rho_f \oint_{\Gamma_m} (\mathbf{r}_{i,j,k} - \mathbf{r}_m) \times (\boldsymbol{\tau} \cdot \mathbf{n})dS \qquad (3.25)$$

Subsequently, the evaluation of the drag and the torque acting on a particle will be evaluated. The viscous drag in the x-direction can (as an example) be obtained from equation 3.26.

$$-F_{d,\mu,x} = \sum_s 2\mu \frac{\partial \mathbf{u}_x}{\partial x} \mathbf{n}_x A + \mu \left(\frac{\partial \mathbf{u}_x}{\partial y} + \frac{\partial \mathbf{u}_y}{\partial x} \right) \mathbf{n}_y A + \mu \left(\frac{\partial \mathbf{u}_x}{\partial z} + \frac{\partial \mathbf{u}_z}{\partial x} \right) \mathbf{n}_z A \quad (3.26)$$

The expressions for the force components in the y and z-directions are analogous. The local partial derivatives at the surface of the particle can be calculated using the second order fits, which are used to enforce the no-slip boundary condition. The spatial derivative of a certain velocity component $\frac{\partial \psi}{\partial \zeta}$, is calculated with equation 3.27, for those cases where there is no other particle in the same direction, ζ.

$$\frac{\partial \psi}{\partial \zeta}\bigg|_{\zeta=\zeta_s} = \frac{2 - \zeta_s}{(1 - \zeta_s)}\psi_1 - \frac{1 - \zeta_s}{(2 - \zeta_s)}\psi_2 - \frac{3 - 2\zeta_s}{(1 - \zeta_s)(2 - \zeta_s)}\psi_s \tag{3.27}$$

Because the equation is singular when $\zeta_s = 1$, the first order fit is also used in the determination of the local velocity derivatives:

$$\frac{\partial \psi}{\partial \zeta}\bigg|_{\zeta=\zeta_s} = \frac{1}{(2 - \zeta_s)}\psi_2 - \frac{1}{(2 - \zeta_s)}\psi_s \tag{3.28}$$

Both the second order and first order fit change when a central cell has two neighbors in the same direction that are inside an immersed object. In such a case, the calculation of the derivatives changes to respectively equations 3.29 and 3.30.

$$\frac{\partial \psi}{\partial \zeta}\bigg|_{\zeta=\zeta_s} = \frac{(\zeta_s) - \zeta_{s2})^2}{\zeta_{s0}(1 - \zeta_{s0}[1 - \zeta_{s2}]) - \zeta_{s2}(1 - \zeta_{s2}[1 - \zeta_{s0}])}\psi_1$$
$$- \frac{1 - 2\zeta_{s0} + 2\zeta_{s0}\zeta_{s2} - \zeta_{s2}^2)}{\zeta_{s0}(1 - \zeta_{s0}[1 - \zeta_{s2}]) - \zeta_{s2}(1 - \zeta_{s2}[1 - \zeta_{s0}])}\psi_{s0} \tag{3.29}$$
$$- \frac{1 + 2\zeta_{s0} - 3\zeta_{s0}^2}{\zeta_{s0}(1 - \zeta_{s0}[1 - \zeta_{s2}]) - \zeta_{s2}(1 - \zeta_{s2}[1 - \zeta_{s0}])}\psi_{s2}$$

$$\frac{\partial \psi}{\partial \zeta}\bigg|_{\zeta=\zeta_s} = -\frac{1}{(\zeta_{s2} - \zeta_{s0})}\psi_{s0} + \frac{1}{(\zeta_{s2} - \zeta_{s0})}\psi_{s2} \tag{3.30}$$

The only unknown in equation 3.26 is the surface area. Because the evaluation of the actual surface area is involved, the projected surface, $\mathbf{n}_i A$, is used. For all derivatives in the same direction as the projected surface, i.e. the first, second and fourth derivative in equation 3.26, the projected surface is estimated to be equal to the projected area of the grid cell. For instance: the projected area used for the first derivative is $\Delta y \Delta z$. For the other derivatives, the projected area is estimated using a tangent plane at the surface, as illustrated in figure 3.3. When a constant normal is assumed over the total area, the projected surface can be calculated from the projected surface in the direction of the normal according to equation 3.31.

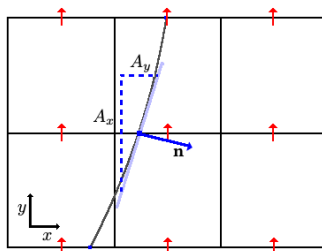$$A_y = A_x \frac{\mathbf{n}_y}{\mathbf{n}_x} \tag{3.31}$$

Figure 3.3: The calculation of the projected surface for all transpose terms in the viscous drag calculation. The area is estimated from the tangent plane as shown by the blue lines in the figure.

Due to the use of the projected area, there can be over- and underestimations of the projected area depending on the positioning of the particle with respect to the grid. In addition, the projected area of the transpose components of the drag force is less accurate due to the assumed constant normal for the plane.

In addition to the viscous drag, the form drag is required in the equation of motion of the particles. The latter can be computed in two different ways: the form drag can be determined via a surface integral or as a volume integral over particle m, as given in equation 3.32.

$$\mathbf{F}_{d,form} = - \oint_{\Gamma_m} p\mathbf{n}dS = - \iiint_{\Omega_m} \nabla p dV \tag{3.32}$$

To calculate the surface integral, the pressure at the surface of the particle is determined via linear extrapolation of the pressure at the fluid nodes near the surface. For the volume integral, the pressure gradient for all nodes inside the particle are calculated using a standard second order central differencing scheme.

Although these integrals both yield the form drag, the actual calculated values may differ. These differences are caused by the linear extrapolation of the pressure. Besides, the methods will only coincide when a closed surface is considered. Due to the applied discretisation in the drag calculation, numerically the surface is not always closed. Due to possible differences between the methods, both methods will be considered in this chapter.

3.5 Verification results

To verify the implementation of both IB methods, two different tests have been performed. The tests are designed to check the implementation of the no-slip boundary condition and the implementation of the drag force. Both tests are performed at creeping flow conditions for which exact analytical results are available.

3.5.1   Stokes flow test

To test the implementation of the drag force, a static single sphere is placed in an infinite domain subject to cross flow. The uniform free stream velocity, v_∞, is chosen such that Stokes flow is ensured (Re ≤ 0.1). For this test case, the velocity profile, the pressure field and the drag force can be derived analytically in spherical coordinates (r,θ,ϕ) (Bird et al., 2007):

$$\mathbf{v}_r = v_\infty \left[1 - \frac{3}{2} \frac{d_p}{2r} + \frac{1}{2} \left(\frac{d_p}{2r} \right)^3 \right] \cos(\theta) \tag{3.33}$$

$$\mathbf{v}_\theta = v_\infty \left[-1 + \frac{3}{4} \frac{d_p}{2r} + \frac{1}{4} \left(\frac{d_p}{2r} \right)^3 \right] \sin(\theta) \tag{3.34}$$

$$\mathbf{v}_\phi = 0 \tag{3.35}$$

$$p = \frac{3}{2} \frac{2\mu v_\infty}{d_p} \left(\frac{d_p}{2r} \right)^2 \cos(\theta) \tag{3.36}$$

$$\mathbf{F}_{d,z} = 3\pi \mu d_p v_\infty \tag{3.37}$$

For this test, the velocity profile and pressure field are initiated and kept at their analytical values using an uniform velocity of $1.0 \cdot 10^{-4}$ m/s. The resulting drag on the 1 mm particles is compared to the analytical drag of equation 3.37. Because the velocity field is imposed, this test can only be performed for the second order implicit IB method. The absolute error in the numerical result for different grid resolutions is shown in figure 3.4.

The figure shows that even with a relatively low number of grid cells in the radial direction of a particle, i.e. $R_p/\Delta x < 6$, the drag force is calculated within 1.0 % accuracy. In addition, the error in the simulated drag force not only depends on the number of grid cells within the particle but also on the placement of the particle boundaries with respect to the grid, which explains the scatter in the data. Finally, it can be concluded that the drag force calculated using the surface integral for the form drag is in general more accurate than the calculation with the volume integral. Nevertheless, the difference between the simulated results using both methods becomes smaller with an increase in the number of grid cells in a diameter.
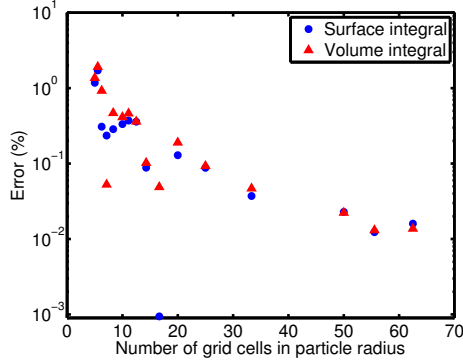
Figure 3.4: Stokes flow around a sphere in an infinite liquid. The figure shows the absolute error between the analytical solution, equation 3.37, and the numerically calculated drag. The results are obtained for the second order IB methods.

Table 3.1: The simulation settings for a diluted array of spheres subjected to fluid flow in the Stokes regime. The computational grid is a cubic domain.

Property	Value	Unit
Solid fractions	0.01...0.002	
Computational grid	74...128	
Grid size	$5.0 \cdot 10^{-5}$	m
Time step	$6.6 \cdot 10^{-4}$	s
Effective particle diameter	$1.0 \cdot 10^{-3}$	m
Computational particle diameter	$9.7 \cdot 10^{-4}$	m
Gas density	1.0	kg/m^3
Gas viscosity	$1.0 \cdot 10^{-5}$	Pas
Inlet velocity	$1.0 \cdot 10^{-3}$	m/s

Subsequently we compare our simulation results with data of Hasimoto (1959), who derived an analytical solution for a particle in a static simple cubic array of spheres subject to Stokes flow. The dimensionless drag force is given by:

$$\frac{F_d}{3\pi\mu d_p v_\infty} = \frac{1}{1 - 1.7601\phi^{\frac{1}{3}} + \phi - 1.5593\phi^2} \tag{3.38}$$

To study this system, simulations were performed for a periodic domain containing exactly one particle. The settings of the simulations are shown in table 3.1. Keeping the particle diameter fixed, the solids volume fraction is changed by varying the size of the periodic domain. To simulate the simple cubic array of spheres, the boundary conditions at
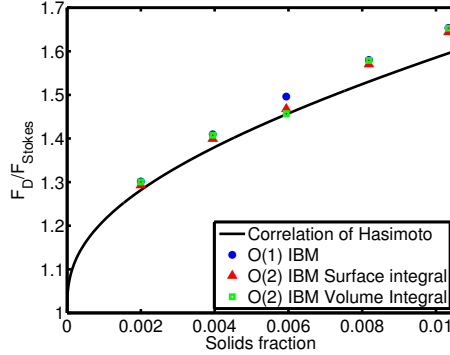
Figure 3.5: Stokes flow around a sphere in a simple cubic particle array. The figure shows the calculated drag normalized by the analytical Stokes drag, equation 3.37. The line in the figure corresponds to the analytical results of Hasimoto (1959), equation 3.38.

the side walls are set to free slip boundary conditions. The results of this test are shown in figure 3.5. The figure shows that the trend in the results is similar to the trend given by the correlation of Hasimoto (1959). The small differences (4%) between the results of Hasimoto (1959) and our numerical results can be explained by the fact that in the simulations only periodicity in the lateral directions perpendicular to the main flow direction was assumed.

Figure 3.5 shows that the results for the first order explicit IB method and the second order implicit IB methods are similar, except for the case with a solids volume fraction of 0.006. The second order IB method performs better for this case because of the relative positioning of the particle with respect to the grid. Furthermore, it should be noted that an effective particle diameter is used in the first order IB method.

3.5.2 Flow around a rotating sphere

Besides the implementation of the drag force, the implementation of the torque should be verified, which is done by placing a rotating particle in an infinite medium. The rotational velocity of the particle is set sufficiently low to achieve Stokes flow conditions ($1.0 \cdot 10^{-5}$ rotations/s). The velocity field and the exerted torque on the 1 mm particle can be derived analytically in spherical coordinates and are given respectively by (Bird et al., 2007):

$$\mathbf{v}_\phi = \omega \frac{d_p}{2} \left(\frac{d_p}{2r} \right)^2 \sin\theta \tag{3.39}$$

$$\mathbf{T}_{d,z} = \pi \mu \omega d_p^3 \tag{3.40}$$

Similar to the test for a single static particle in Stokes flow, both the velocity field and the rotational velocity of the particle are implemented in the model. The torque computed
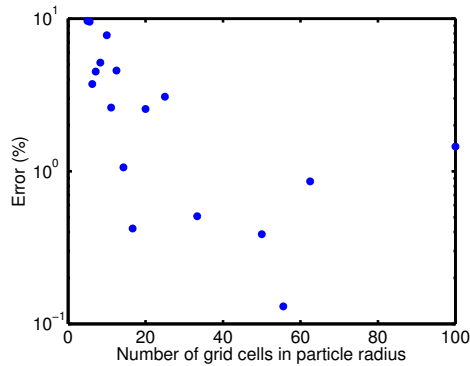
Figure 3.6: Flow around a rotating sphere in an infinite liquid. The figure shows the absolute error between the analytical solution, equation 3.40, and the numerically calculated torque. The results are calculated for the second order IB method.

numerically is compared to the torque obtained from the analytical expression in equation 3.40. The absolute error between the analytical solution and the numerical result is shown in figure 3.6. The results are only shown for the second order IB methods, because the torque cannot be calculated when both the rotational velocity and the velocity field are specified in the first order IB method. Note that in this case the calculated torque is not influenced by the chosen method for the form drag.

The figure clearly shows that the error in the calculated torque is up to 10%. The error only decreases below 1% when $d_p/\Delta x > 80$, which is unfeasible for most simulations. The error is probably caused by the errors in the approximation of the area in equation 3.26. The largest error is made in the transpose terms of the calculation, in which the area is estimated using a tangent plane. When the calculation is performed with the expression for constant viscosity all transpose terms can be neglected. This will probably reduce the errors in the calculation of the torque.

3.6 Validation results

Besides the verification of the method, all models are also validated using experimental results from literature. The tests are performed at much higher flow rates, for denser systems, and for non-static systems as well as cylindrical particles.

3.6.1 Static particle test

First of all, the implementation of the drag force at higher Reynolds numbers is tested. In this test, a static particle in an infinite medium is subjected to a flow at Re = 100. The simulation settings are shown in table 3.2.

Table 3.2: The simulation settings for a sphere in flowing medium with Re = 100.

Property	Value	Unit
Computational grid (nx,ny,nz)	$(160, 160, 180)$	grid cells
Particle positions	$(80, 80, 40)$	grid cells
Grid size	$5.0 \cdot 10^{-5}$	m
Time step	$1.0 \cdot 10^{-5}$	s
Particle diameter	$1.0 \cdot 10^{-3}$	m
Fluid density	$1.0 \cdot 10^{2}$	kg/m^3
Fluid viscosity	$1.0 \cdot 10^{-5}$	Pa s
Inlet velocity	0.01	m/s

The computed drag force is used to determine the drag coefficient according to equation 3.41.

$$C_d = \frac{F_d}{\frac{1}{2}\rho v_\infty^2 A} = \frac{F_d}{\frac{1}{2}\rho v_\infty^2 \frac{1}{4}\pi d_p^2} \tag{3.41}$$

The drag coefficients obtained using the different methods are listed in table 3.3 together with reported literature results. The first order IB method shows a good comparison with the results reported by Beetstra et al. (2007) and Deen et al. (2009), which are using a Lattice Boltzmann method and the method of Uhlmann (2005), respectively. However, the resulting drag is an overestimation of the experimentally obtained drag coefficient (Clift et al., 1978; White, 1974).

Both versions of the second order IB method are in good agreement with the experimental results and the recent numerical results using the Uhlmann method (Clift et al., 1978; White, 1974; Tang et al., 2014). The second order IB method using the surface integral is performing slightly better as expected from the results in the previous section.

3.6.2 Static particle array

For many practical applications involving fluid-solid interactions, like fluidized beds and bubble slurry columns, the solids volume fraction is much higher than in the dilute limit, as used in the previous tests. Zick and Homsy (1982) determined the drag force acting on a sphere in a dense simple cubic array. The drag force obtained using the Boundary Integral method is fitted to obtain a correlation for the drag in densely packed simple cubic arrays at low Reynolds numbers (Deen et al., 2009).

The settings for the simulation are shown in table 3.4. For these simulations, the drag force acting on the central sphere in the array is determined, the results of which are listed in table 3.5. The results of both the first order and the second order IB methods show a better comparison with the Boundary integral method than the Uhlmann method of Deen et al. (2009), which is still within the error margin of the fit. The deviation of the second

Table 3.3: The results of the simulation of a stationary particle at Re $= 100$.

	Drag coefficient
Clift et al. (1978)	1.191
White (1974)	1.185
Zhang and Prosperetti (2005)	1.09
Beetstra et al. (2007)	1.267
Deen et al. (2009)	1.271
Tang et al. (2014)	1.178
O(1) Immersed Boundary method	1.264
O(2) Immersed Boundary method with surface integral	1.175
O(2) Immersed Boundary method with volume integral	1.186

Table 3.4: The simulation settings for a densely packed array of static spheres.

Property	Value	Unit
Computational grid (nx,ny,nz)	$(160, 160, 160)$	grid cells
Total number of spheres	125	
Solid volume fraction (ϕ)	0.382	
Grid size	$1.0 \cdot 10^{-3}$	m
Time step	$1.0 \cdot 10^{-5}$	s
Particle diameter	$2.88 \cdot 10^{-2}$	m
Effective diameter	$2.83 \cdot 10^{-2}$	m
Fluid density	$1.0 \cdot 10^{2}$	kg/m^3
Fluid viscosity	$5.0 \cdot 10^{-2}$	Pa s
Inlet velocity	$5.0 \cdot 10^{-3}$	m/s

order IB method using the surface integral is slightly larger than both the other methods, which is probably because of the linear extrapolation of the pressure to the particle surface.

3.6.3 Falling particle test

To determine if the update of the particle velocity and the particle position is implemented correctly, four different simulations of a settling particle have been performed with the different IB methods. In the first three simulations the terminal settling velocity is determined. The terminal velocities are compared with the experimental results of Mordant and Pinton (2000). The simulation settings of these simulations and the results are summarized in table 3.6. In addition, on all domain boundaries free-slip boundary conditions are applied and the window shifting principle is applied to keep the particle at its initial position (Deen et al., 2004).

Although the obtained terminal velocities are slightly lower at high Reynolds numbers

Table 3.5: The results for the dimensionless drag for the central particle in an array. The drag of the central particle is divided by the Stokes drag.

	Dimensionless drag
Boundary integral method of Zick and Homsy (1982)	19.16
The Ulhmann method of Deen et al. (2009)	19.9
O(1) Immersed Boundary method	19.41
O(2) Immersed Boundary method with surface integral	19.51
O(2) Immersed Boundary method with volume integral	19.02

(table 3.6), the results of the first order IB method are in good comparison with the experimental results and the correlations of Clift et al., Schiller and Nauman and Lapple (Mordant and Pinton, 2000; Clift et al., 1978). The lower velocity is probably caused by the confinement of the wake in the simulation domain, which prevents a full development of the wake and thus influences the resulting velocity profile.

The second order IB method is able to predict the terminal velocity at low Reynolds numbers accurately. However, at high Reynolds numbers the terminal velocities differ, especially when the volume integral is used to calculate the form drag. The low values of the terminal settling velocity are due to horizontal movement of the particle. The horizontal movement originates from the Magnus lift forces (Rubinow and Keller, 1961) that arise as a consequence of the development of a rotational velocity of the particle. The (unexpected) rotational velocity is a result of numerical errors in the evaluated torque (see previous section).

To enable a comparison between the experimental results and the simulations, table 3.6 also shows the results before the onset of rotation. Comparing these results with the experimental results, the simulation results are within the error margin of the experimental data. Therefore, it can be concluded that the second order method is able to accurately predict the terminal velocity of particles with a Reynolds number above 100 when the time of free flight is less then 0.1 s.

Besides the terminal rise velocity, the velocity profile and the particle position can be compared. ten Cate et al. (2002) reported a good agreement between experimental results and Lattice Boltzmann simulation results. In this case, the IB methods are used to simulate one of the cases of ten Cate et al. (2002). The simulation settings are shown in table 3.7.

The results of the simulations are compared with the experimental results in figure 3.7. The first order IB method underestimates the velocity of the particle slightly. This is probably caused by the large effective particle diameter related to the forcing in this method. However, the results are comparable to the results obtained using the modified Uhlmann method (Kempe and Fröhlich, 2012) and the combined Lattice Boltzmann IB method of Feng and Michaelides (2005). Although the results of both the second order IB method slightly

Table 3.6: The parameters used for the settling sphere cases. The experimental results for the terminal velocity, v_t, are taken from Mordant and Pinton (2000). Furthermore, terminal velocities according to correlations of Clift and Gauvin, Schiller and Nauman and Lapple are calculated, see Clift et al. (1978). The results shown in parentheses are the results before the particle obtained a horizontal velocity.

Case	1	2	3
Computational grid (nx,ny,nz)	(140, 140, 180)	(120, 120, 220)	(120, 120, 260)
Particle positions	(70, 70, 40)	(60, 60, 40)	(60, 60, 40)
Grid size (m)	$2.5 \cdot 10^{-5}$	$4.0 \cdot 10^{-5}$	$5.0 \cdot 10^{-5}$
Time step (s)	$1.0 \cdot 10^{-5}$	$1.0 \cdot 10^{-5}$	$1.0 \cdot 10^{-5}$
Particle diameter (m)	$5.0 \cdot 10^{-4}$	$8.0 \cdot 10^{-4}$	$1.0 \cdot 10^{-3}$
Computational particle diameter (m)	$4.86 \cdot 10^{-4}$	$7.78 \cdot 10^{-4}$	$9.73 \cdot 10^{-4}$
$\mathbf{g}$ (m/s^2)	$(0, 0, -9.81)$	$(0, 0, -9.81)$	$(0, 0, -9.81)$
Liquid density (kg/m^3)	1000	1000	1000
Liquid viscosity (Pa s)	$9.0 \cdot 10^{-4}$	$9.0 \cdot 10^{-4}$	$9.1 \cdot 10^{-4}$
Particle density (kg/m^3)	2560	7710	7850
Experimental v_t (m/s)	-0.074	-0.316	-0.383
v_t using the correlation of Clift et al. (m/s)	-0.076	-0.325	-0.393
v_t using the correlation of Schiller and Nauman (m/s)	-0.078	-0.316	-0.387
v_t using the correlation of Lapple (m/s)	-0.080	-0.315	-0.383
v_t of Uhlmann (2005) (m/s)	-0.074	-0.318	
v_t using first order IB method (m/s)	-0.075	-0.309	-0.370
v_t using second order IB method with surface integral (m/s)	-0.077	$-0.322(-0.326)$	$-0.381(-0.390)$
v_t using second order IB method with volume integral (m/s)	-0.077	$-0.289(-0.326)$	$-0.353(-0.389)$

Table 3.7: The simulation of a settling sphere of ten Cate et al. (2002).

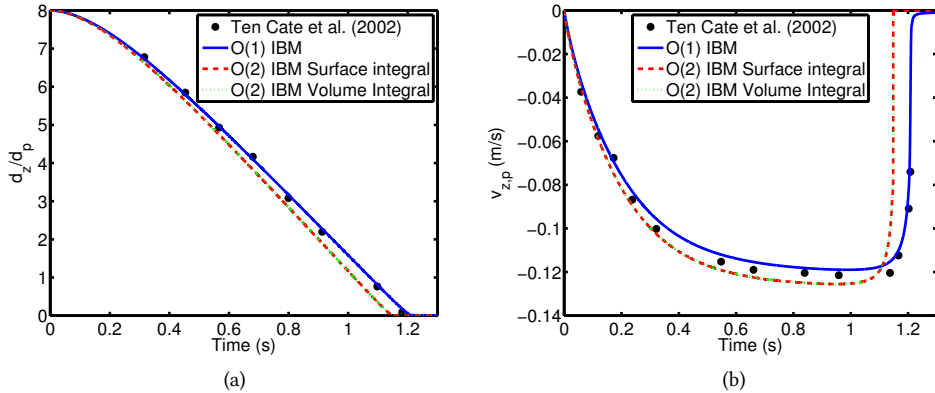| Property	Value	Unit
Computational grid (nx,ny,nz)	$(214, 214, 214)$	grid cells
Particle positions	$(107, 107, 170)$	grid cells
Grid size	$7.5 \cdot 10^{-4}$	m
Time step	$1.0 \cdot 10^{-4}$	s
Particle diameter	$1.5 \cdot 10^{-2}$	m
g	$(0, 0, -9.81)$	m/s^2
Fluid density	$9.6 \cdot 10^2$	kg/m^3
Fluid viscosity	$5.8 \cdot 10^{-2}$	Pa s
Particle density	$1.12 \cdot 10^3$	kg/m^3

Figure 3.7: The settling of a particle of ten Cate et al. (2002). Figure a shows the position of the bottom of the particle divided by the particle diameter, while figure b shows the velocity profile.

overestimate the particle velocity, they are a closer match to the experimental work than the first order IB method. Nevertheless, the Lattice Boltzmann method of ten Cate et al. (2002) has an even closer match with the experimental results. It should however be noted that ten Cate et al. (2002) uses an effective diameter for the particles, which has been calculated using the analytical solution of Hasimoto (1959).

3.6.4 Flow around a semi-infinite cylinder

To enable the simulation of a wire mesh, the methods should be able to accurately simulate cylinders. The implementation of the cylinders is checked using the experimental data of Nishioka and Sato (1974). In the experiments, the drag exerted on a static semi-infinite
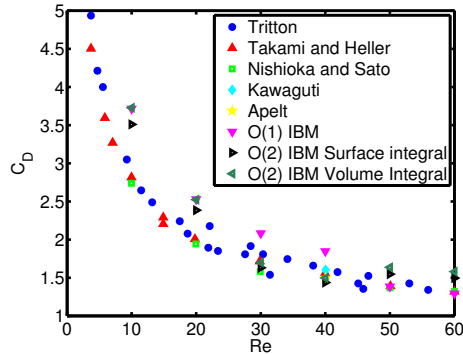
Figure 3.8: Simulation data compared to the experimental data of Nishioka and Sato (1974).

cylinder was determined at several Reynolds numbers. To simulate these experiments, a infinite cylinder was created by using periodic boundary conditions in the axial direction of the cylinder. For the lateral domain boundaries, a free slip boundary was used. The remaining simulation settings are given in table 3.8.

The results of these simulations are shown in figure 3.8. The figure shows a good agreement of the drag coefficient with the experimental results of Nishioka and Sato (1974) and Tritton (1959) and the numerical results of Takami and Keller (1969), Kawaguti (1953) and Apelt (1958). The first order IB method is not as accurate at lower Reynolds numbers (Re $\leq$ 40). Furthermore, all models show deviations at Re = 10, which is probably caused by a too small distance between the inlet and the position of the cylinder. At low Reynolds numbers, the fluid flow is distorted by the introduction of the cylinder even before the flow reaches the cylinder (Clift et al., 1978).

3.7   Conclusions

In this chapter, the main characteristics of the first order explicit IB method and the second order implicit IB method were presented. The existing Uhlmann method was extended to enable the calculation of neutrally buoyant particles using the method of Kempe and Fröhlich (2012). Moreover, the second order implicit IB method has been extended for systems with a variable viscosity and for systems with high solids volume fractions.

The implemented models have been verified and validated. The verification tests show that both the first order IB method and the second order IB method are able to calculate the drag force accurately. However, the verification of the torque showed that an error of 1-10% is obtained when less than 80 grid cells in the diameter of the particle are used. The problem can probably be resolved by a more accurate calculation of the area used in equation 3.26.

The validation results showed that the first order IB method is able to accurately calculate the drag on dense particle arrays. However, this method overestimates the drag

Table 3.8: Simulation settings for a cylinder subject to cross flow.

	Re = 10	Re = 20	Re = 30	Re = 40	Re = 50	Re = 60
Computational grid	$(3, 400, 500)$	$(3, 400, 500)$	$(3, 400, 500)$	$(3, 400, 500)$	$(3, 400, 500)$	$(3, 400, 500)$
Particle positions	$(1.5, 200, 330)$	$(1.5, 200, 330)$	$(1.5, 200, 330)$	$(1.5, 200, 330)$	$(1.5, 200, 330)$	$(1.5, 200, 330)$
Grid size (m)	$1.005 \cdot 10^{-4}$	$1.005 \cdot 10^{-4}$	$2.015 \cdot 10^{-4}$	$2.015 \cdot 10^{-4}$	$1.005 \cdot 10^{-4}$	$1.005 \cdot 10^{-4}$
Time step (s)	$1.00 \cdot 10^{-5}$	$1.00 \cdot 10^{-5}$	$1.00 \cdot 10^{-5}$	$1.00 \cdot 10^{-5}$	$1.00 \cdot 10^{-5}$	$1.00 \cdot 10^{-5}$
Cylinder diameter (m)	$2.01 \cdot 10^{-3}$	$2.01 \cdot 10^{-3}$	$4.03 \cdot 10^{-3}$	$4.03 \cdot 10^{-3}$	$2.01 \cdot 10^{-3}$	$2.01 \cdot 10^{-3}$
Cylinder density (kg/m^3)	$2.00 \cdot 10^3$	$2.00 \cdot 10^3$	$2.00 \cdot 10^3$	$2.00 \cdot 10^3$	$2.00 \cdot 10^3$	$2.00 \cdot 10^3$
Fluid density (kg/m^3)	1.00	1.00	1.00	1.00	1.00	1.00
Fluid viscosity (Pa s)	$1.63 \cdot 10^{-5}$	$1.50 \cdot 10^{-5}$	$1.52 \cdot 10^{-5}$	$1.52 \cdot 10^{-5}$	$1.50 \cdot 10^{-5}$	$1.50 \cdot 10^{-5}$
Inlet velocity (m/s)	$8.10 \cdot 10^{-2}$	$1.49 \cdot 10^{-1}$	$1.13 \cdot 10^{-1}$	$1.51 \cdot 10^{-1}$	$3.73 \cdot 10^{-1}$	$4.48 \cdot 10^{-1}$

force on particles with Re $\geq$ 100. At low Reynolds numbers, the overestimation can be compensated by the use of an effective diameter that is smaller than the real particle size. However, at high solids volume fractions, for cases other than Stokes flow and in cases of non-spherical objects, the application of an effective diameter is questionable, because there are no analytical results to determine the effective diameter in these cases.

Furthermore, the validation cases also show that in principle the determination of the form drag using the surface integral is more accurate than using the volume integral. However, when the solids volume fraction is high, the form drag is overestimated using the surface integral. This is probably caused by the linear extrapolation of the drag near the surface in this method, which performs worse in case the distance between the particle surfaces becomes small.

Both second order IB methods introduce a rotational velocity for the falling particle tests at high Reynolds numbers (Re $\geq$ 100). This rotational velocity is acquired due to accumulation of the error in the torque calculation. The results show that the rotation of the particle leads to an unexpected horizontal velocity, related to a Magnus lift force.

Concluding, the first order IB method is only able to accurately calculate the drag force on particles and the velocity profile when the Lagrangian force points are placed on a computational particle diameter, which is slightly smaller than the real particle diameter. For objects other than spheres, there is no analytical solution to enable the determination of the computational size of the objects. Therefore, the use of the second order IB method is advised, except for freely moving particles at Reynolds numbers above 100, because the particles acquire an unphysical rotational velocity because of errors in the calculation of the torque. The second order IB method can be improved by improving the calculation of the torque and the drag force by improving the area determination.

VALIDATION OF BUBBLE-BUBBLE INTERACTIONS

4.1 Introduction

The gas-liquid interfacial area in a bubble column can be increased by introducing micro-structuring in the form of a wire mesh. Such a wire mesh serves the purpose of cutting large bubbles into smaller pieces. After a bubble is cut, the resulting bubbles may interact, which could lead to coalescence just after they have left the mesh. This will reduce the efficiency of the bubble cutting. The efficacy of the wire mesh can be studied numerically using direct numerical simulations (DNS). If we were to predict the bubble cutting efficiency, a reliable prediction of bubble-bubble interaction is essential. Although the Volume of Fluid (VoF) model was validated for a single rising bubble in chapter 2, the bubble-bubble interactions have not been validated for this model. Since the simplest form of bubble-bubble interactions is that for two equally sized bubbles, this is chosen as a test case to validate the VoF model in this chapter.

The last decades, the interaction of two equally sized bubbles has been extensively studied. Both experimentally and numerically, it was shown that the leading bubble is almost unaffected by the trailing bubble, while the velocity of the trailing bubble increases as it approaches the leading bubble. This acceleration of the trailing bubble is probably caused by the wake generated by the leading bubble (Yuan and Prosperetti, 1994; Ruzicka, 2000; Ramírez-Muñoz et al., 2011; Yu et al., 2011). Nevertheless, when the bubbles have a very small separation distance, the velocity of the leading bubble is also increased. This velocity increase is lower than the differences obtained for the trailing bubble (Yu et al., 2011).

Besides the velocity of the bubbles, the trajectories of the bubbles were also studied.
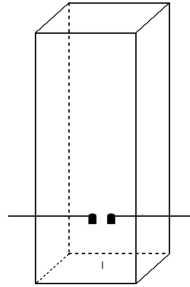
Figure 4.1: A schematic overview of the set-up. The images are taken in the direction of the view.

Harper (1997), Yuan and Prosperetti (1994) and Yu et al. (2011) reported that there exists a certain equilibrium distance between the bubbles, where the distance between the bubbles remains constant. This distance depends on the bubble Reynolds number and the Morton number. The equilibrium occurs due to the competitive effects of the low pressure between the bubbles and the vorticity generated by the leading bubble. However, Yu et al. (2011) also showed that there always was attraction between the bubbles at moderate Reynolds numbers (Re $\geq$ 49.6). Furthermore, the bubbles, which are initially in an oblique configuration, are moving into the wake of the leading bubble, resulting in a vertical alignment of the bubble (Yu et al., 2011).

This chapter describes the validation of the VoF-model for the bubble-bubble interactions. The details of the bubble coalescence/separation will not be addressed here, because the VoF model will automatically lead to merging bubbles, once the bubbles are less then one computational cell apart from each other. Therefore, the resulting coalescence does not necessarily have to be physical. Hence, with the VoF model we can only validate the bubble-bubble interaction up to the point of coalescence of the bubbles. This chapter starts with the explanation of the experimental set-up and the simulation approach. Subsequently, the experimental and simulation results will be presented and discussed.

4.2   Experimental set-up

To study the interaction between two bubbles, experiments are performed in a square glass column of 0.2 m diameter and 1.2 m height. Clift et al. (1978) showed that bubbles are moving freely, without influences from the confining walls, provided that the ratio of the bubble diameter to the column diameter is less than 0.1. In this work, we satisfy this condition, because the bubbles have a equivalent diameter of 7.25 mm, leading to a diameter ratio of 0.04. At the bottom of the column, two spoon-shaped caps are installed. The caps are cylinders with a diameter of 10 mm and are moveable in the horizontal direction (figure 4.1).

Table 4.1: The average liquid properties of the water-glycerol mixture used in the experiments.

Property	Value	Unit
ρ_l	$1.187 \cdot 10^3$	$\mathrm{kg/m^3}$
μ_l	$4.980 \cdot 10^{-2}$	$\mathrm{Pa \cdot s}$
σ	$6.680 \cdot 10^{-2}$	$\mathrm{N/m}$

The column is filled with a mixture of deminiralised water and glycerol. The mixture was stirred using continuous air flow for three weeks. The average properties of the liquid are shown in table 4.1. The properties are averaged over 10 separate measurements during the course of the experiments. The viscosity was measured with a Brookfield DV-E viscometer at room temperature and the surface tension was measured at room temperature using K20 EasyDyne digital of Krüsse with the Wilhelmy plate method.

To create 7.25 mm bubbles, a volume of 0.2 mL was injected into the column, using a 0.5 mL syringe. Because injection of this volume of gas usually leads to several bubbles, that are caught in the cap, a settling time of half an hour is taken to ensure that they coalesced to a single bubble.

To create oblique bubble interaction, the caps are placed next to each other. Next, the caps are slowly turned to release the gas volume keeping its initial velocity close to zero. For the cases of vertically in-line bubble-bubble interaction, the second cap is moved beneath the leading bubble, as soon as the first bubble has left. We note that this is done slowly, not to disturb the velocity field appreciably.

The velocity and the trajectory of the bubbles were determined with a high speed camera (Imager Pro HS CMOS camera with a resolution of 1280 × 1024 pixels). The images are recorded at a frequency of 350 Hz using back lighting, which is only switched on during the imaging to reduce any heating of the liquid while illuminating the column. The back of the column is covered with white plastic to diffuse the light. In total 32 experiments were performed for both oblique and in-line interactions.

4.3 Simulation set-up

Direct Numerical Simulations (DNS) are performed using the Volume of Fluid (VoF) method detailed in chapter 2. Here, only the main features of this method will be given. The continuity equation, equation 4.1, and the Navier-Stokes equation, equation 4.2, are solved on a fixed (Eulerian) grid assuming incompressible flow.

$$\nabla \cdot \mathbf{u} = 0 \tag{4.1}$$

$$\rho\frac{\partial\mathbf{u}}{\partial t} = -\nabla p - \rho\nabla\cdot(\mathbf{uu}) - \nabla\cdot\boldsymbol{\tau} + \rho\mathbf{g} + \mathbf{F}_\sigma \tag{4.2}$$

These equations provide a one-field approximation, assuming that the velocity field is continuous over the gas-liquid interface. Surface tension is taken into account in the form of a force density that acts in the vicinity of the gas-liquid interface. This force density is calculated using the Continuum Surface Force (CSF) method of Brackbill et al. (1992), represented by equation 4.3.

$$\mathbf{F}_\sigma = \sigma\kappa\mathbf{n} \tag{4.3}$$

The interface normal $\mathbf{n}$ and the curvature, κ, are respectively calculated from the first and second derivative of the phase fraction. Because the color function is a step function across the interface, these derivatives cannot directly be calculated with the standard discretisation schemes. The phase fractions are first smoothed using the method described in van Sint Annaland et al. (2005). In this chapter, no pressure jump correction was applied.

The velocity field is calculated on a staggered grid using a projection-correction method. In this method, the new velocity field is first estimated by solving the Navier-Stokes equations, equation 2.3, explicitly, except for the diffusion term, which is evaluated semi-implicitly. The implicit term of the diffusion term is chosen such that all components of the velocity field can be calculated separately whereas the remaining part is treated explicitly. The diffusion term is discretised with the second order central difference scheme, while the convective term is discretised with a second order flux-delimited Barton scheme. After the tentative velocity is obtained, it is corrected by solving a Poisson pressure equation, which enforces the continuity. Both the tentative velocity field and the pressure field are obtained by solving the associated matrix equations using the ICCG method.

When the velocity field is known, the new phase fraction can be determined using the Piecewise Linear Interface Calculation (PLIC) scheme of Youngs (1982). In this advection scheme, the interface is represented by one of the five generic cases. The color function is governed by equation 4.4 and is solved with a pseudo Lagrangian geometrical advection scheme to maintain sharp interfaces.

$$\frac{DF}{Dt} = \frac{\partial F}{\partial t} + \mathbf{u}\cdot\nabla F = 0 \tag{4.4}$$

When the new phase fraction is known in each cell, the new density and viscosity can be determined by linear averaging and harmonic averaging, respectively, using the value of the color function as a weighting factor.
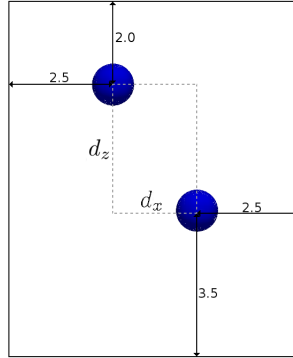
Figure 4.2: Positioning of the bubbles in the computational domain. The numbers indicate the distances between the bubble center of mass and the domain boundaries, normalized by the equivalent bubble diameter.

Table 4.2: Simulation settings and physical properties.

Property	Value	Unit
Domain size (nx,ny,nz)	$(150...240, 150, 225...375)$	grid cells
Grid size (Δx, Δy & Δz)	$2.42 \cdot 10^{-4}$	m
Time step	$1 \cdot 10^{-5}$	s
d_b	$7.250 \cdot 10^{-3}$	m
ρ_l	$1.187 \cdot 10^3$	kg/m^3
μ_l	$4.980 \cdot 10^{-2}$	Pa$\cdot$s
ρ_g	1.25	kg/m^3
μ_g	$1.8 \cdot 10^{-5}$	Pa$\cdot$s
σ	$6.680 \cdot 10^{-2}$	N/m

In total 11 different VoF simulations were performed. To enable a detailed comparison with the experimental data, the liquid properties and the bubble size were set equal to their experimental counterparts. At all domain boundaries free slip boundary conditions are applied. To ensure that the bubble rise is not affected by the size of the computational domain, the bubbles are positioned at a appreciable distance from the domain boundaries, as illustrated in figure 4.2. The distance between the bubbles ranged from 0 to 3 bubble diameters in the horizontal direction and 0 to 7 bubble diameters in the vertical direction. To ensure that the bubbles do not move out of the domain, window shifting is applied with respect to the leading bubble. As a result the position of the leading bubble remains unchanged with respect to the domain boundaries during the course of the simulation (Deen et al., 2004).

4.4 Effect of the bubble-bubble interaction on the velocity

First of all, the effects of the bubble-bubble interaction on the bubble velocity was studied. Similar to results reported in literature, the trailing bubble has no effect on the velocity of the leading bubble except when the bubbles get very close. This was found both experimentally and numerically (Yu et al., 2011). In contrast, the velocity of the trailing bubble increases considerably compared to the velocity of an isolated bubble in both the experiments and the simulations. This increase is caused by shielding of the trailing bubble by the wake of the leading bubble, which decreases the drag force (Yuan and Prosperetti, 1994; Ramírez-Muñoz et al., 2011; Yu et al., 2011). The increase of the velocity is larger as the bubbles are closer to each other, which is similar to the results of Ramírez-Muñoz et al. (2011) and Yu et al. (2011).
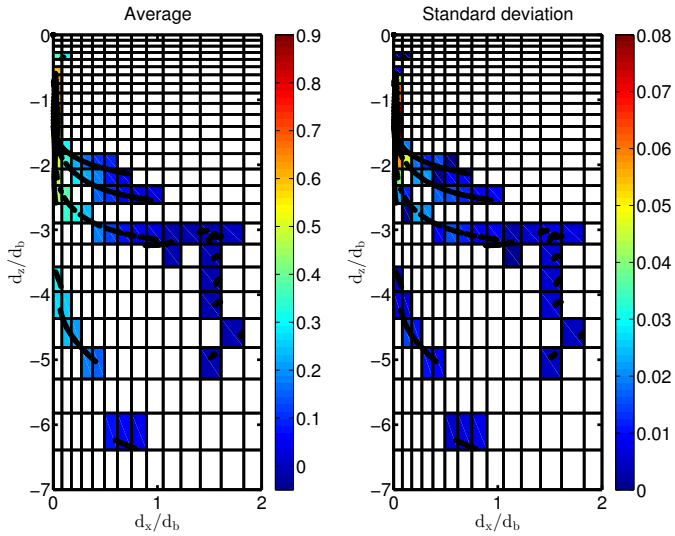
The experimental and simulation results are shown in figure 4.3.a and 4.3.b, respectively. The black dots in the figure show the trajectory of the bubbles. The trajectories in figure 4.3.a show that all the trailing bubbles move into the wake of the leading bubbles. Identical behavior is obtained in the simulations as shown in figure 4.3.b. Furthermore, both the experimental and the simulation results show that the vertical interaction is stronger than the horizontal interaction; the bubble-bubble interaction extends for at least seven equivalent bubble diameters in the vertical direction, while the leading bubble only influences the trailing bubble 1.5 equivalent bubble diameters in the horizontal direction. This is similar to the observations reported by Kitagawa et al. (2004).

To quantitatively study the effect of the bubble-bubble interaction on the rise velocity, the relative velocity difference between the leading and the trailing bubble is determined using equation 4.5.

$$\mathbf{v}_{z,rel} = \frac{\mathbf{v}_{z,\text{trailing}} - \mathbf{v}_{z,\text{leading}}}{\mathbf{v}_{z,\text{leading}}} \tag{4.5}$$

The relative velocity difference between the leading and the trailing bubble is used, because the single bubble Reynolds number obtained experimentally and numerically differ only slightly, i.e. Re = 32.9 and Re = 31.0 respectively. This difference is similar to the deviations reported in chapter 2. These differences are probably caused by the presence of contaminants in the experiments, which is not represented in the VoF model.

The colors in the left parts of figure 4.3 show the average relative velocity difference, while the right parts show the standard deviation. When the experimental results are compared with the simulation results, it can be seen that larger standard deviations prevail in the experiments. The large standard deviation can be caused by experimental errors. First of all, there is an uncertainty of 0.005 mL in the injected gas volume, which can lead to somewhat different bubble sizes and hence different rise velocities. Furthermore, the quiescent liquid state may be disturbed too much if the caps are turned too fast. Finally, the
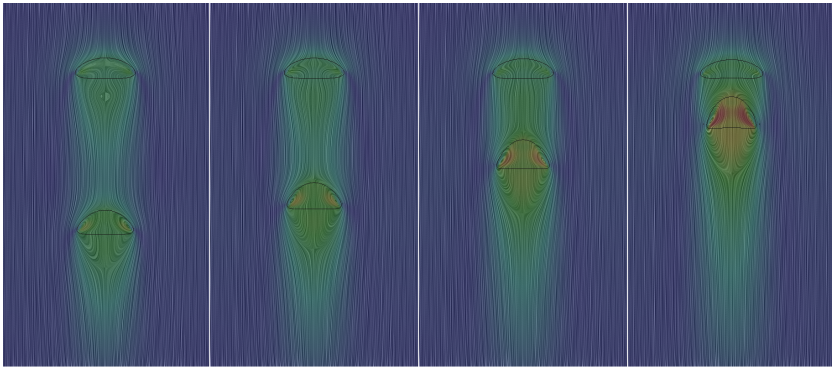
(a) Experimental results
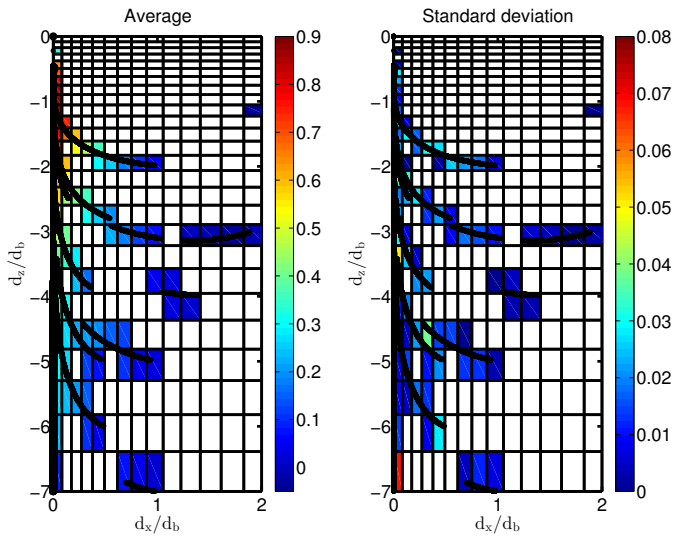

(b) Simulation results

Figure 4.3: The relative difference between the rise velocity of the leading and the trailing bubble, $\mathbf{v}_{z,rel}$. The colors in the left figures indicate the average value, while the colors in the right figures show the standard deviation. The black points indicate the trajectories of the bubbles.

(a) In-line bubble interaction
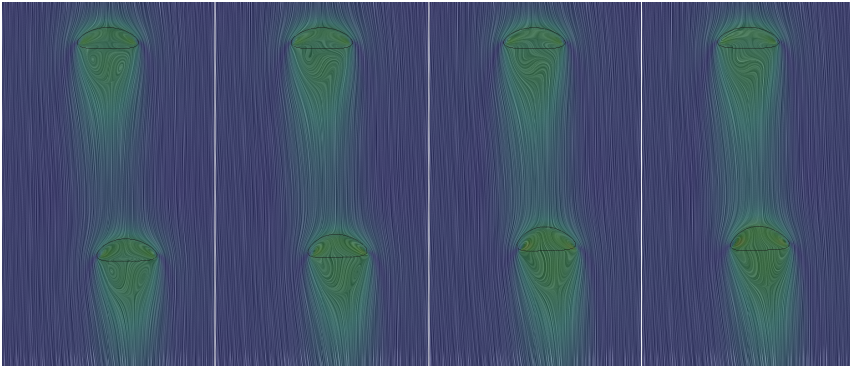
(b) Oblique bubble interaction
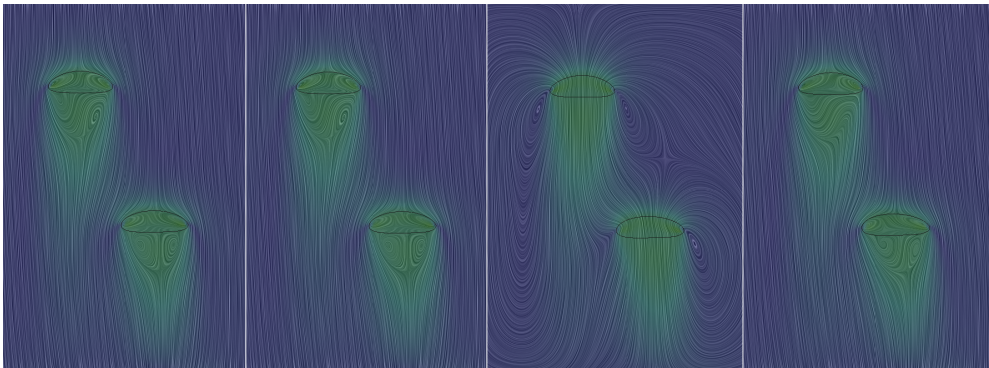
(c) Oblique bubble interaction

Figure 4.4: The velocity profile evaluation of one in-line and two oblique interactions. The coloring of the image indicates the magnitude of the velocity ranging from 0 to 0.5 m/s in all images. The black line indicate the contour of the bubble in this slice of the domain.

image recognition of the bubbles is difficult, especially when the bubbles are close to each other.

With respect to the relative bubble velocity difference, it can be seen that the experimental results are consistently lower than the simulation results. However, the difference between the experiments and the simulations is within the standard deviation. Therefore, it is concluded that the VoF model is able to capture the effect of bubble-bubble interactions on the bubble velocity. Furthermore, the trajectory of the trailing bubble with respect to the leading bubble is accurately captured by the VoF model.

One of the advantages of using DNS to determine the bubble-bubble interaction is that the stream lines in both the liquid and gas phase can be obtained accurately. In figure 4.4, the flow streamlines for an in-line interaction and two oblique interactions are shown. For a single rising bubble, symmetric streamlines are obtained around the vertical axis. Two vortexes are present inside the bubble and one vortex behind the bubble (Clift et al., 1978). When bubble interaction is vertical, the velocity profiles around both bubbles are influenced. The vortexes behind the leading bubble decrease as the second bubble gets closer. Eventually, the velocity profile around the trailing bubble effects the shape of the leading bubble, while squeezing out the liquid layer in between the bubbles.

For all oblique interactions shown in figure 4.3, the trailing bubble moves in the direction of the middle of the wake. This same behavior is also visible in the oblique interactions in figure 4.4. In contrast to the in-line interaction, the oblique interaction between the bubbles also changes the symmetry of the vortexes inside the bubble; the vortexes are shifted toward the other bubble. Furthermore, the streamlines around the bubbles indicate that the trailing bubble moves toward the center of the wake of the leading bubble, because the vortex trailing the first bubble induces a horizontal velocity on the bubble.

In the first two snapshots of figure 4.4.c, the trailing bubble is moving slower than the leading bubble. The streamlines show that the trailing bubble is affected by the downward moving liquid around the leading bubble. However, the trailing bubble is still moving toward the center of the wake. In the third and fourth snapshot, the trailing bubble has entered the wake of the bubble and therefore starts moving toward the first bubble. The rest of the trajectory is similar to the trajectory of the bubble in figure 4.4.b and is not shown here.

4.5 Effect of the bubble-bubble interaction on the bubble shape

Besides the trajectory of the bubbles and the bubble velocity, the shape of the bubbles can also be determined in both the experiments and the simulations. The shape of the bubbles can be quantified by the aspect ratio, E. This parameter quantifies the deviation from the spherical shape ($E = 1$), and is defined as:

$$E = \frac{d_{\max,z}}{\sqrt{d_{\max,x} d_{\max,y}}} \tag{4.6}$$

In the experiments, only one of the horizontal components of the diameter is known. For the other horizontal direction, the diameter is assumed equal to the known horizontal component. In the simulations, the diameters are determined using the PLIC interface reconstruction of each bubble. Once the aspect ratio of both the leading and the trailing bubble is known, the relative difference in aspect ratio was calculated with equation 4.7.
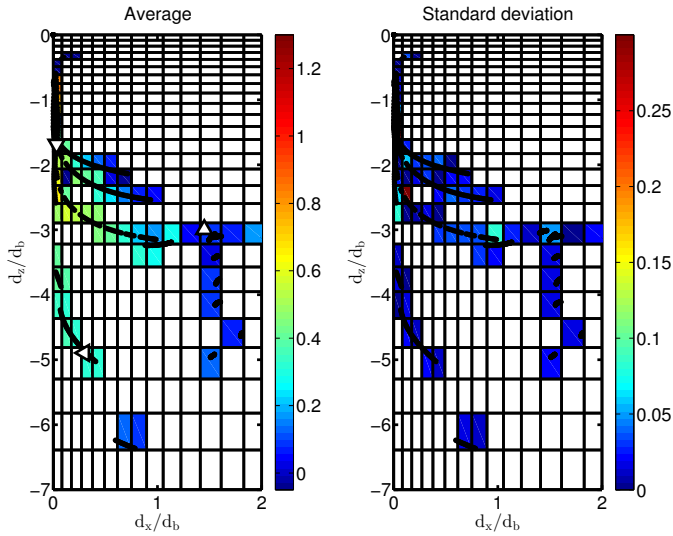
$$E_{rel} = \frac{E_{\text{trailing}} - E_{\text{leading}}}{E_{\text{leading}}} \qquad (4.7)$$

The relative difference in aspect ratio is calculated to compare results obtained with slightly different liquid and gas properties, due to small differences in the experimental conditions. Furthermore, a small amount of contaminants is present in the experiments, which might lead to additional differences with the simulations.

The experimental results are shown in figure 4.5.a. The left figure shows that the aspect ratio of the trailing bubble is much larger than the aspect ratio of the leading bubble, when the trailing bubble enters the wake of the leading bubble. The trailing bubble is thus elongated in the vertical direction when it enters the wake of the leading bubble. However, the right figure shows that the standard deviation of the difference in aspect ratio is considerable for the experimental results. This is caused by problems in the bubble recognition, because the determination of the exact position of the gas-liquid interface is difficult in these experiments.

The simulation results presented in figure 4.5.b also show an increase of the aspect ratio of the trailing bubble in the wake of the leading bubble. However, the standard deviations of the data are much smaller in these cases as shown in the right figure. Only when the bubbles are close to each other the standard deviation is substantially larger. This is probably caused by a very fast change in bubble shape when the bubbles are in close proximity.

Although the numerically determined aspect ratio considerably exceeds the experimentally obtained aspect ratio, the simulation results are within the standard deviation of the experimental results. Because the aspect ratio only takes into account the maximum diameter in each direction and given the large standard deviations of the experimental data, we also compared the changes in bubble shape qualitatively. Figure 4.6 shows three snapshots of the experimental and the corresponding simulation results. Comparing the top row with the bottom row reveals that the bubble shapes in the simulations are similar to the experimental results. Any of the remaining small differences might be caused by small differences in the physical properties, a small amount of contaminants in the experiments and a small difference in the relative position of the two bubbles. As a consequence, it is concluded that the VoF model accurately determines the effect on the bubble-bubble interaction with respect to the bubble shape.

(a) Experimental results
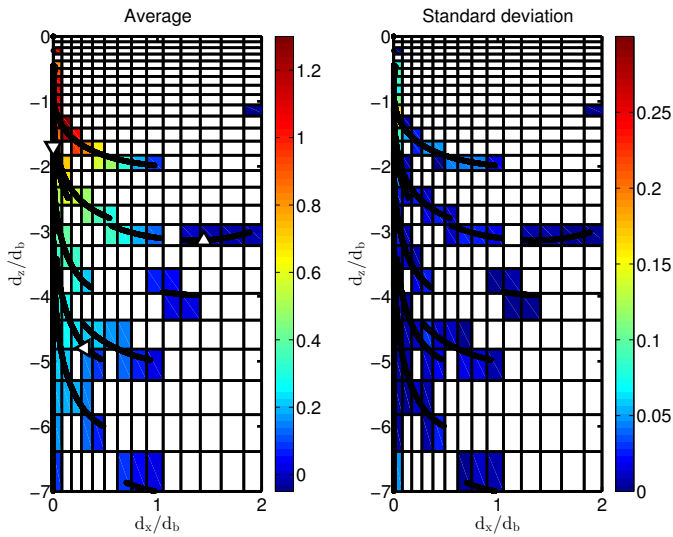
(b) Simulation results

Figure 4.5: The relative difference between aspect ratio of the leading and the trailing bubble. The colors in the left figures indicate the average value, while the colors in the right figure show the standard deviation. The black points indicate the trajectories of the bubbles. The three triangles correspond to the three snapshots in figure 4.6.

(a) ▽   (b) ◁   (c) △

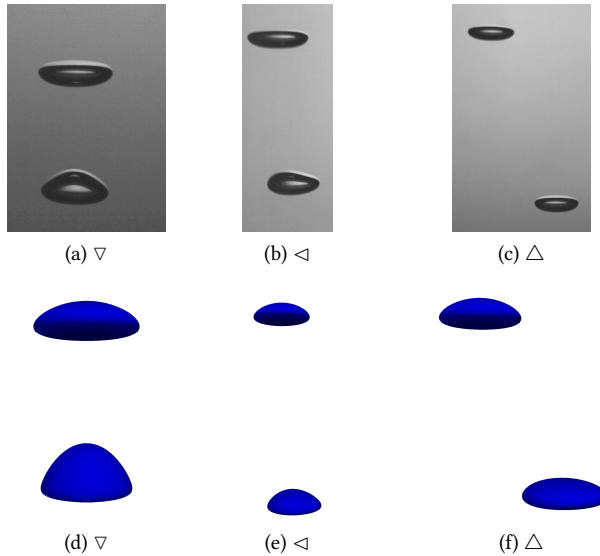(d) ▽   (e) ◁   (f) △

Figure 4.6: The shape of the bubbles at three different relative positions. The triangles correspond to the positions in figure 4.5. The top row are experimental results and the bottom row are the simulation results at almost the same position.

4.6   Conclusions

In this chapter, bubble-bubble interaction simulated with the VoF model was shown to favorably compare to the experimentally observed bubble-bubble interaction. The bubble-bubble interactions were studied using a relative simple system of two equally sized bubbles. The simulated relative velocity difference between the leading and trailing bubble for the VoF model compares well to the relative velocity difference observed in the experiments. Furthermore, the bubble shape obtained from the VoF simulations agrees well with the experimental results. Therefore, it is concluded that the VoF model is able to accurately capture the process of bubble-bubble interaction. Nevertheless, it should be noted that all VoF simulations showed coalescence while no coalescence was obtained in the experiments. As a consequence, the coalescence of bubbles cannot be studied with the current model.

The experimental and simulation results contain small differences, which can be decreased by both improving the experiments and the simulations. The current experimental results can be improved by decreasing the amount of contamination in the glycerol-water mixture. In this way, more "clean" experiments can be performed that reduce the influence of contaminants on the rigidity of the bubble surface and hence will increase the ability of bubbles to coalesce. The contaminants in the fluid arise due to the high solubility of hydrophilic contaminants in the glycerol-water mixture and the hygroscopic nature of glyc-

erol. Because a mixing time of three weeks is used, the amount of contaminants will be substantial, it is therefore advised to decrease the mixing time of the glycerol-water mixture. Furthermore, automation of the bubble injection or the use of a more accurate syringe will decrease the error in the bubble size. Finally, the experimental results can be improved when the bubble recognition is performed more accurate.

Although the current VoF model uses the CSF model of Brackbill et al. (1992) to model the surface tension at the gas-liquid interface, the verification results in chapter 2 show that the CSF model is not able to calculate the surface tension accurately. The single bubble simulations in chapter 2 demonstrated that the use of both the height function model and the tensile force method can more accurately predict the bubble shape and the bubble rise velocity. Hence, it is expected that the simulation results in the current chapter can also be improved by using either of these models.

Finally, the VoF model is not able to accurately capture the bouncing of bubbles, because the bubbles will automatically merge when two bubbles are less than one grid cell apart. To introduce bouncing in the simulations a different model should be used, which is inherently mass conservative and tracks the gas-liquid interface directly. This can be achieved by combining the VoF model with the Front Tracking model (Torres and Brackbill, 2000; Walker et al., 2013).

5

The effect of particles on the hydrodynamics of a bubbly flow

5.1 Introduction

Due to the increase in the oil prices, the interest in Fischer-Tropsch process for synthetic fuels and methanol synthesis has increased in recent years. The Fischer-Tropsch process is mostly performed in slurry bubble columns. To improve the design and scale-up of gas-to-liquid processes, better understanding of the hydrodynamics and the complex three-phase interactions is required (Kantarci et al., 2005; Wang et al., 2007; Yang et al., 2007).

The introduction of particles in a bubble column is known to decrease bubble sizes in the column and to reduce the void fraction. Furthermore, the rise velocity of bubbles is decreased when the solids volume fraction is increased (Kantarci et al., 2005; Wang et al., 2007; Hooshyar et al., 2013). Hooshyar et al. (2013) determined that for neutrally buoyant particles the mechanism of this decrease depends on the Stokes relaxation time of the particles. When the relaxation time is relatively small, the particles only influence the velocity via an increase of the apparent viscosity. Although larger particles also influence the apparent viscosity of the fluid, the decrease in the bubble velocity is mainly caused by the collisions of the particles with the bubbles.

In this chapter, Direct Numerical Simulations (DNS) will be used to study the effect of the particles on gas-liquid-solid hydrodynamics. The effect of the particles will be condensed in the form of drag correlations for both the particles and the bubbles. To enable the study of dense bubbly swarms, the Front Tracking (FT) method is used, because it does not suffer

from artificial coalescence. This prevents unphysical merging of the bubbles and ensures a constant bubble size, which is beneficial for the derivation of the drag coefficient of the bubbles. The particles are simulated with the second order implicit Immersed Boundary (IB) method of Deen et al. (2012). This method was chosen, because the method does not require an effective particle diameter. Although the method showed some problems with the freely moving particles at high Reynolds numbers, it is expected that the disturbance of the bubbles and the frequent collisions with both particles and bubbles will diminish the effect of any unphysical rotation.

This chapter starts with an explanation of the applied numerical method. Subsequently, the simulation settings will be discussed whereafter the effect of the void fraction and the solids volume fraction on the drag coefficient of the bubbles and the particles will be presented and discussed.

5.2 Numerical method

The numerical method is a based on the FT method of Roghair et al. (2013a) and the second order IB method of Deen et al. (2012), detailed in chapter 2 and 3, respectively. In this chapter, only a brief discussion of the models will be given, particularly focusing on the combination of both methods. The combined FT-IB model solves the continuity equation, equation 5.1, and the Navier-Stokes equations, equation 5.2, assuming incompressible flow.

$$\nabla \cdot \mathbf{u} = 0 \tag{5.1}$$

$$\rho \frac{\partial \mathbf{u}}{\partial t} = -\nabla p - \rho \nabla \cdot (\mathbf{u}\mathbf{u}) - \nabla \cdot \boldsymbol{\tau} + \rho \mathbf{g} + \mathbf{F}_\sigma \tag{5.2}$$

The Navier-Stokes equations are solved using a one-field approximation, because the velocity field is continuous across the gas-liquid interface. To take into account the surface tension at the gas-liquid interface, an extra force density, $\mathbf{F}_\sigma$, is introduced near the interface. This force density is calculated using triangular markers, that represent the gas-liquid interface. The tensile force of each marker, m, is calculated with equation 5.3, in which $\mathbf{t}_{mi}$ is the shared tangent of marker m and neighboring marker i, whereas $\mathbf{n}$ is the normal of the marker.

$$\mathbf{F}_{\sigma,m} = \frac{1}{2}\sigma \sum_{i=1}^{3} (\mathbf{t}_{i,m} \times \mathbf{n}_i) \tag{5.3}$$

The tensile force of a marker is mapped to the surrounding Eulerian cells using a mass-weighting function. Because there is a possibility of a mismatch between the discretisation of the surface tension and the pressure field, the calculation of the pressure field and the

surface tension are coupled, by adding an extra pressure force density at the gas-liquid interface in the Navier-Stokes equations (see chapter 2) (Renardy and Renardy, 2002; Francois et al., 2006; Dijkhuizen et al., 2010b).

The no-slip boundary condition at the particle surface is accounted for at the level of the discretised Navier-Stokes equations, where each velocity component at a certain node in the fluid, ψ_c, can be described as a function of the velocity components of the neighboring nodes, ψ_{nb}, with equation 5.4.

$$a_c \psi_c + \sum_{nb} a_{nb} \psi_{nb} = b_c \tag{5.4}$$

where the coefficients a_{nb} indicate the dependence of the velocity at node c with respect to the velocities of the neighboring nodes, nb. When one of the neighboring nodes is located inside a particle, the no-slip boundary condition is applied by fitting a second order (1D) polynomial. The fit expresses the local velocity profile in terms of the velocity at the particle surface and the two velocity values just outside the particle. Subsequently, the node inside the particle is eliminated from equation 5.4 and the coefficients of the two velocity values involved in the polynomial fit are adapted.

Using the same approach, a similar function is obtained for nodes that are neighbored by nodes inside two particles in close proximity. Because both equations are singular when the particle surface is close to the central cell, a linear fit is used when the distance between the surface and the central point is less than 0.0001 times the grid size.

The velocity field given by equation 5.2 is solved on a staggered grid using a projection-correction method. In the projection step, all terms in this equation are treated explicitly except for the diffusion term, which is treated semi-implicitly. The implicit part of the diffusion term is chosen such that it only depends on the velocity component that is solved, whereas the remaining (small) terms are treated explicitly. The diffusion terms are discretised using a second order central difference scheme, while a second order flux-delimited Barton scheme is used for the convective terms. The projected velocity field is corrected to satisfy the continuity equation (equation 5.1). The equations in both the projection step and the correction step are solved using a block ICCG matrix solver, which is parallelised with OpenMP.

After the calculation of the velocity field, the positions of the particles, m, are updated by solving the Newtonian equations of motion:

$$V_m \rho_m \frac{d\mathbf{w}_m}{dt} = \rho_f \left(\oint_{\Gamma_m} -(\boldsymbol{\tau} \cdot \mathbf{n}) dS + \iiint_{\Omega_m} -\nabla p dV \right) \tag{5.5}$$

$$I_m \frac{d\boldsymbol{\omega}_m}{dt} = \rho_f \oint_{\Gamma_m} (\mathbf{r}_{i,j,k} - \mathbf{r}_m) \times -(\boldsymbol{\tau} \cdot \mathbf{n}) dS \tag{5.6}$$

$$I_m = \frac{1}{10} V_m \rho_i d_m^2 \tag{5.7}$$

The velocity derivatives required in the evaluation of the stress tensor and the pressure gradient can be obtained directly from the second order fit used to apply the no-slip boundary condition. The used viscosity in the equation is the macroscopic viscosity of the grid cell in which the surface segment of the particle is situated. When the derivative of the velocity is calculated at the edge of a grid cell, e.g. the derivative of the x-component of the velocity in the y-direction, the average macroscopic viscosity of both neighboring cells is used. Although the verification and validation tests in chapter 3 show that the differences between the volume integral method and the surface integral method are small, the surface integral is not able to accurately calculate the drag of a particle in dense particle arrays. Therefore, the volume integral method has been applied in this chapter.

When the new position of the particles is known, the position of the bubbles can be updated. Because of the one-field approximation, the velocity of the marker points is interpolated from the surrounding Eulerian grid cells using a piecewise cubic spline. Each of the marker points is displaced separately with fourth order Runga-Kutta time stepping. Due to the separate advection of each marker point, the bubble not only changes its position, but also its shape. Nevertheless, the separate advection also changes the distance between the marker points, which leads to a decrease in quality of the surface mesh. The quality is improved by a remeshing procedure consisting of four elementary operations: edge splitting, edge collapsing, edge swapping and smoothing (Roghair, 2012).

Moreover, the separate advection of the marker points and the remeshing procedure cause small volume changes of the bubble. Due to the large number of time steps involved in a single simulation, a small volume change per time step can become significant over the total simulation time. Therefore, a smoothing procedure described by Kuprat et al. (2001) is implemented, which locally restores small volume losses. However, volume losses due to the separate advection of the marker points are not corrected yet. This is compensated by distributing the lost volume over all the interface cells. This procedure might cause unphysical overlap between the bubbles and particles. Therefore, marker points that are close to another bubble, particle or wall are excluded from this operation.

5.3   Simulation set-up

As an initial condition, spherical bubbles and particles are placed randomly in a periodic cubic domain. The randomization is performed using a Monte-Carlo method. In this method, the bubbles and particles are first placed in a structured manner in the domain. Subsequently, each of the dispersed elements (bubbles/particles) is slightly moved 200 times. The procedure is repeated until no overlap between the elements is found. The result is the initial condition of the simulation; examples are shown for three different cases in figure 5.1.

Because periodic boundary conditions are used, it is important to determine the minimum number of bubbles and particles that do not generate artifacts due to the finite box size. When the number of bubbles or particles are too low, the interactions between par-
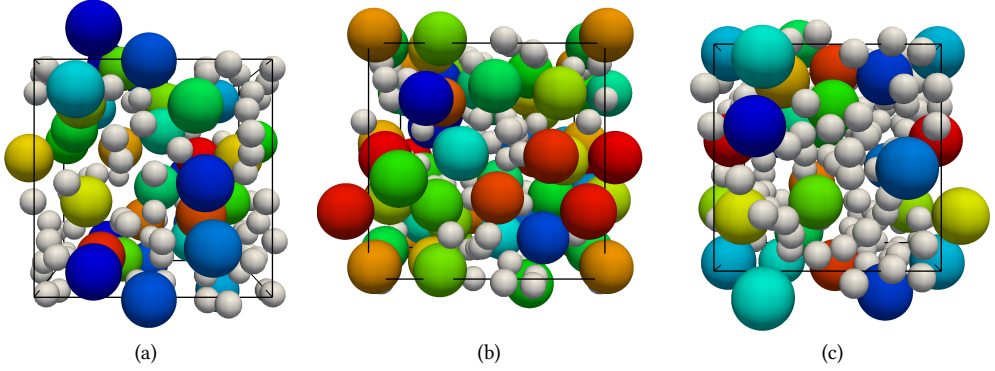
Figure 5.1: The initial randomized position for three different systems. Figure a shows a simulation with a void fraction of 15% and a solids fraction of 5% , figure b shows the simulation with void fraction of 25% and a solids fraction of 5% and figure c shows the simulation with a void fraction of 15% and a solids fraction of 10%.

Table 5.1: The simulation settings for the base case of the bubble slurry swarms.

| Property	Value	Unit
Void fraction, α	0.30	
Solid volume fraction, ϕ	0.05	
Computational grid	171	
Grid size	$1.0 \cdot 10^{-4}$	m
Time step	$1.0 \cdot 10^{-5}$	s
Bubble diameter	$2.0 \cdot 10^{-3}$	m
Particle diameter	$1.0 \cdot 10^{-3}$	m
Liquid density	$1.0 \cdot 10^{3}$	kg/m^3
Liquid viscosity	$1.0 \cdot 10^{-3}$	Pas
Gas density	100.0	kg/m^3
Gas viscosity	$1.8 \cdot 10^{-5}$	Pas
Solids density	$2.0 \cdot 10^{3}$	kg/m^3
Surface tension	0.073	N/m
Normal restitution coefficient	1.00	
Tangential restitution coefficient	1.00	
Friction coefficient coefficient	0.00	
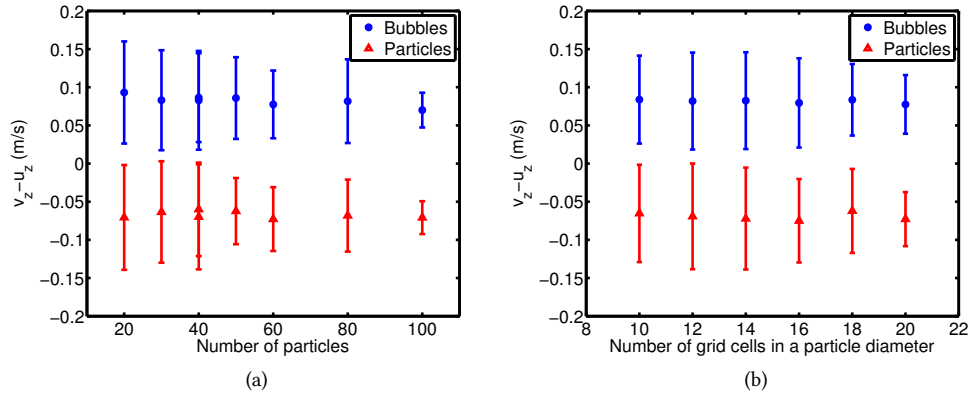
Figure 5.2: Time-averaged relative velocities of the bubbles and the particles as a function of the simulation box size expressed as the number of particles in the simulation box (a) and as a function of the simulation resolution expressed in number of grid cells across the particle diameter (b). All simulations are performed with a void fraction of 30% and a solids volume fraction of 5%. The simulations in figure a use 20 grid cells in a particle diameter, while the simulations in figure b use 60 particles in the simulation. The bars indicate the standard deviations in the velocities.

ticles, bubbles and bubbles and particles are not accurately captured. Roghair et al. (2011) and Bunner and Tryggvason (2002) determined that the minimum amount of bubbles in a bubble swarm is 12. To determine the minimal number of particles in a simulation, a base case simulation was started with 20-100 particles in the simulation (see table 5.1). Figure 5.2.a shows that there is no effect of the number of particles on the slip velocity of both the particles and the bubbles when the number of particles is larger than 40. To ensure that all the interactions are captured accurately, the minimum number of bubbles and particles is respectively set to 16 and 60.

Besides the number of bubbles and particles in a simulation, also the grid resolution should be chosen in such a way that grid independent results are obtained. Dijkhuizen et al. (2010a) determined that the minimum number of grid cells across a bubble diameter is 20. For the particles, the minimum number of grid cells in the diameter is unknown. Therefore, the number of grid cells in a particle diameter was varied between 10 and 20 for the base case of table 5.1. The results in figure 5.2.b show that there is almost no effect of the grid resolution. Therefore, the minimum number of grid cells in a particle is set to 10.

To determine the effect of the void fraction and the solids volume fraction on the bubble drag force 27 different simulations were carried out. The simulations are grouped in four different cases, which are listed in table 5.2. All simulations are started with a time step of $1.0 \cdot 10^{-5}$ s for 1 s. To remove any start-up effects, the first 0.2 s is not taken into account

Table 5.2: The simulation settings for the four different cases studied to determine the effect of solids volume fraction and the void fraction.

Case	α	ϕ	$-\log(\text{Mo})$	Eo	t_{avg}
1	0.20	0.02...0.14	10.6	0.48	0.8
2	0.40	0.02...0.14	10.6	0.48	0.25...0.8
3	0.15...0.45	0.05	10.6	0.48	0.55...0.8
4	0.15...0.45	0.10	10.6	0.48	0.8

for the results.

5.4 The drag coefficient of the bubbles

The effect of the particles on the bubble drag force, is quantified by varying the solids volume fraction and the void fraction. Subsequently, the drag coefficient of the bubbles was determined. To calculate the drag coefficient, a macroscopic force balance on the bubbles is considered. At a pseudo steady state, the time-averaged drag will exactly balance the gravitational force and the hydrostatic pressure, as shown in equation 5.8.

$$- < \mathbf{F}_D >=< \mathbf{F}_G > + < \mathbf{F}_P > \tag{5.8}$$

Using the same definitions for the drag force, the gravitational force and the hydrostatic pressure as done in many Euler-Lagrangian models, the drag coefficient can be determined.

$$\frac{1}{8}C_D\rho_l\pi d_b^2|\mathbf{v}_b - \mathbf{u}|(\mathbf{v} - \mathbf{u}) = V_b\rho_g\mathbf{g} + \nabla p V_b \tag{5.9}$$

$$\frac{1}{8}C_D\rho_l\pi d_b^2|\mathbf{v}_b - \mathbf{u}|(\mathbf{v}_b - \mathbf{u}) = V_b\mathbf{g}(\rho_g - (\alpha\rho_g + \phi\rho_s + (1 - \alpha - \phi)\rho_l)) \tag{5.10}$$

To obtain a relative drag coefficient which is in direct correspondence to the terminal rise velocity of a single bubble with the same size and the average velocity of the bubbles in the simulation, the drag coefficient obtained from the simulations is normalized by dividing it by the drag coefficient of a single bubble rising in an infinite liquid obtained by Tomiyama (1998), equation 5.11.

$$C_{D,\infty} = \frac{4d_b(\rho_l - \rho_g)\mathbf{g}_z}{3\rho_l\mathbf{v}_{z,b}^2} = max\left\langle min\left[\frac{16}{\text{Re}}\left(1 + 0.15\text{Re}^{0.687}\right), \frac{48}{\text{Re}}\right], \frac{8}{3}\frac{\text{Eo}}{\text{Eo} + 4}\right\rangle \tag{5.11}$$
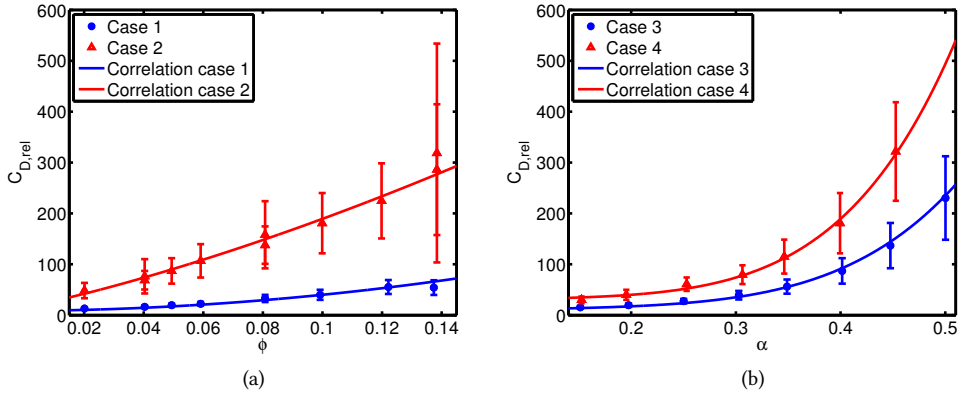
(a)   (b)

Figure 5.3: The effect of the solids volume fraction, figure a, and the effect of the void fraction, figure b, on the normalized drag coefficient of the bubbles. The drag is normalized using equation 5.12. The lines in the figures represent the fit of equation 5.14.

Because the hydrostatic pressure is different in the case of a single rising bubble, the calculated bubble rise velocity has to be corrected with the void fraction and the solids volume fraction, equation 5.12:

$$C_{D,rel} = \frac{C_D}{C_{D,\infty} \left(1 - \alpha - \phi \frac{\rho_l - \rho_s}{\rho_l - \rho_g} \right)} = \frac{< \mathbf{v}_{b,\infty} >^2}{(< \mathbf{v}_b > - < \mathbf{u} >)^2} \tag{5.12}$$

Note that in the absence of particles ($\phi = 0$) or in case of neutrally buoyant particles ($\rho_l - \rho_s = 0$) equation 5.12 reduces to an equation of the same form as derived by Roghair et al. (2011).

The relative drag coefficients resulting from the simulations are shown in figure 5.3. The bars in the figures show the standard deviation of the drag coefficient of the bubbles. Both figures show that there is a combined dependency of the void fraction and the solids volume fraction. Furthermore, the results in case 2 show the effect of different initial settings. The simulations with a particle fraction of 8% both have a long averaging time, but the resulting relative drag coefficient differ approximately 12%, which is well within the largely overlapping standard deviations. The standard deviations of the drag coefficient found in this work are larger than those obtained for gas-liquid bubble swarms, which is due to the interactions with the particles.

The data presented in figure 5.3 were used to derive a correlation for the bubble drag coefficient. The form of the correlation was chosen such that it gives the right behavior in
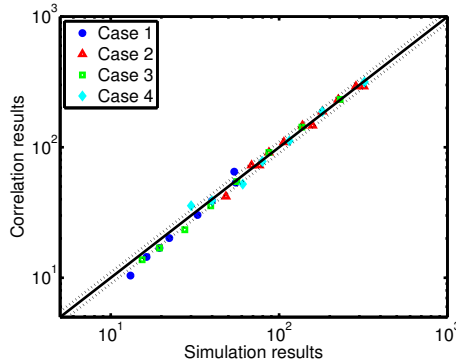
Figure 5.4: A parity plot containing the drag coefficient of the particles obtained from the simulations and the correlation given by equation 5.14. The dashed lines indicate an error of 10%.

the limit that there are no particles. This limit was already described by Roghair et al. (2011), who derived the following drag relation for bubble swarms without particles:

$$C_{D,rel} = 1 + \frac{18}{\text{Eo}}\alpha \tag{5.13}$$

Furthermore, it is expected that the drag coefficient of a single bubble ($\alpha = 0$) is higher in a liquid containing particles. Using these constraints and the simulated results, a fit for the relative drag coefficient was obtained:

$$C_{D,rel} = 1 + \frac{18}{\text{Eo}}\alpha + 1.8 \cdot 10^5 \alpha^5 \phi^{1.1} + 2.7 \cdot 10^3 \phi^2 \tag{5.14}$$

The correlation accurately captures the trends in the drag coefficient with respect to the void fraction and the solids volume fraction, as shown by the lines in figure 5.3. The results of the simulation and the correlation are also compared in the parity plot in figure 5.4. The parity plot shows that most of the correlation results are within 10% of the fit. On average, the differences between the correlation and the simulation results is 7.6%, which is less than the spread in results obtained by using different initial conditions. The maximal difference between the correlation and the simulation is 20%. The largest errors are found for low solids volume fractions and low void fractions.

5.5 The drag coefficient of the particles

To determine the effect of the void fraction and the solids volume fraction on the terminal velocity of the particles, the drag coefficient on the particles is determined in a similar
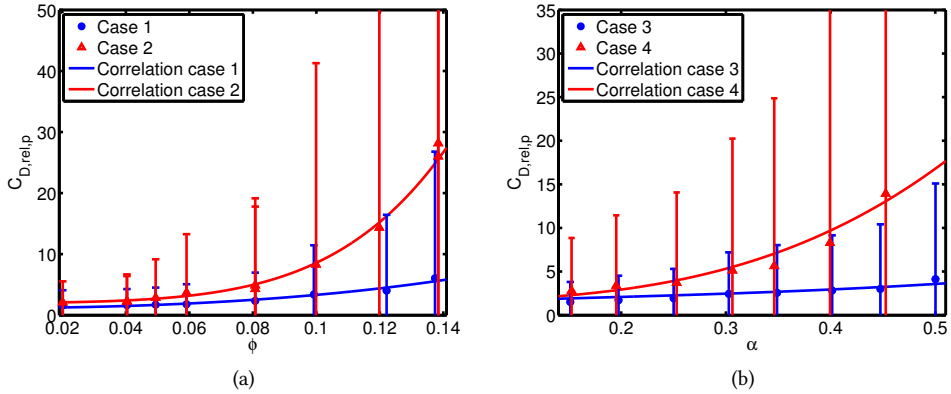
Figure 5.5: The effect of the solids volume fraction (a), and the effect of the void fraction (b) on the normalized drag coefficient of the particles. The drag is normalized using equation 5.16. The lines in the figures represent the fit of equation 5.17.

manner as for the bubbles. Note that in this case however, the particle drag coefficient is normalized with the drag coefficient of a single falling particle in an infinite fluid, given by Schiller and Nauman (Clift et al., 1978):

$$C_{D,\infty,p} = \frac{4d_p(\rho_l - \rho_p)\mathbf{g}_z}{3\rho_l \mathbf{v}_{z,p}^2} = \frac{24}{\mathrm{Re}_p}\left(1 + 0.15\mathrm{Re}_p^{0.687}\right) \tag{5.15}$$

The resulting relative drag coefficient is given by:

$$C_{D,rel,p} = \frac{C_D}{C_{D,\infty,p}\left(1 - \phi - \alpha\frac{\rho_g - \rho_l}{\rho_s - \rho_l}\right)} = \frac{<\mathbf{v}_{p,\infty}>^2}{(<\mathbf{v}_p> - <\mathbf{u}>)^2} \tag{5.16}$$

Figure 5.5 shows the obtained relative drag coefficients of the particles. Both figures also show the standard deviation in the drag force. The figure clearly shows that the drag force on the particles occasionally changes direction. This is because the combination of one bubble and one particle is buoyant with respect to the liquid, which occasionally leads to mutual rise of a bubble and a particle. The difference between different initial settings is slightly less (8%) than the difference obtained for the drag force of the bubbles.

Using the obtained drag coefficients, a correlation is fitted to determine the effect of the void fraction and the solids volume fraction on the drag coefficient. The fit should meet two criteria. First of all, when the void fraction and the volume solids fraction approach zero, the relative drag coefficient of the particle should be equal to 1. Furthermore, it is expected that the drag coefficient of a single particle in a bubble swarm or in a particle swarm have a
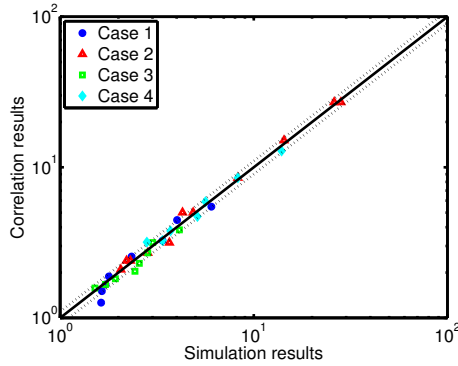
Figure 5.6: A parity plot containing the drag coefficient of the particles obtained from the simulations and the correlation given by equation 5.17. The dashed lines indicate an error of 10%.

relatively higher drag than a single particle in an infinite liquid. The obtained fit is shown in equation 5.17.

$$C_{D,rel,p} = 1 + 10\alpha^{2.5} + 200\phi^2 + 1.41 \cdot 10^7 \phi^{4.5} \alpha^5 \tag{5.17}$$

The lines in figure 5.5 show that the fit captures the trends in the drag coefficient accurately. To examine the performance of the fit, a parity plot is given in figure 5.6. The average absolute difference between the simulation and the correlation results is 7.1% with a maximum of 22.5%.

5.6 Bubble clustering

Both correlations, equation 5.14 and 5.17, indicate an increase of the drag coefficient with increasing solids volume fraction and void fraction. Figure 5.7 shows two uncorrelated snap shots of a simulation with a void fraction of 25% and a solids volume fraction of 5%. In the bottom right of figure 5.7.a, some particles are clustering on top of the bubbles effectively hindering the rise of the bubbles. At the same time the velocity of the particles is decreased or even reversed in direction. Due to buoyancy forces and the surface tension of the bubbles, the particles will eventually roll down the side of the bubble.

Although the snapshot in figure 5.7.a shows almost no clustering of the particles and the bubbles, the snapshot in figure 5.7.d shows a clear horizontal clustering of the bubbles. Some of the bubbles are moving out of the structure, which ensures a dynamic system. The obtained clustering of the bubbles is similar to the clustering effect observed in the bubble swarms simulated by Roghair et al. (2013b). Although the clustering of the bubbles obstructs

(a)   (b)   (c)

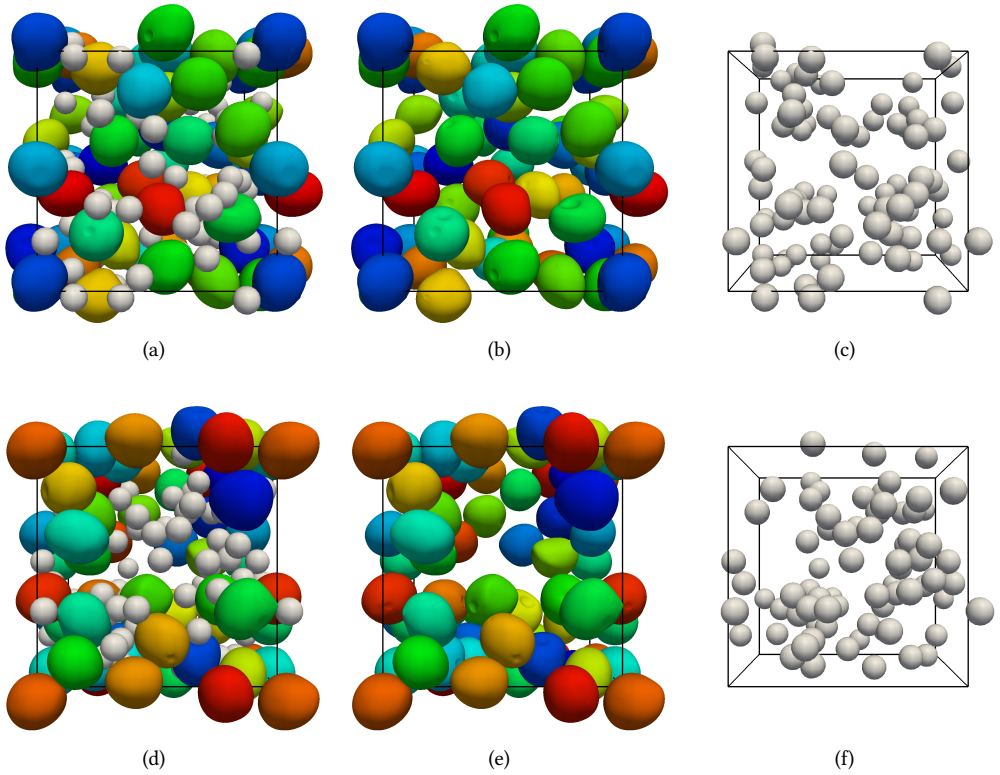(d)   (e)   (f)

Figure 5.7: The two snap shots of a simulation with a void fraction of 25% and a solids volume fraction of fraction 5%. Figure a and d show both the particles and the bubbles, while the middle and the right figures only show the bubble configuration and the particle configuration.

the movement of the particles, the particles are also falling between the horizontal clusters without any hindrance of the bubbles.

Both snapshots show that particles have two different modes of movement: particle movement obstructed by the bubbles and (almost) free movement. The appearance of these two different modes also explains the large standard deviation in the obtained drag coefficient of the particles. To obtain a more accurate formulation of the drag coefficient of the particles, the drag coefficient should be determined separately for both modes of movement.

5.7 Conclusions

In this chapter, the combined FT second order implicit IB method was used to simulate a dense bubble/particle swarm. Using a particle diameter of 1 mm and a bubble diameter of 2 mm, the effect of the void fraction and the solids volume fraction on the drag coefficient of the bubbles and the particles was determined.

To mimic a sufficiently large bubble/particle swarm, the minimum required number of bubbles and particles was found to be 16 and 60, respectively. Furthermore, grid independence of the drag coefficient was obtained if the minimum number of grid cells inside a bubble diameter and a particle diameter are set to respectively 20 and 10. Using these settings four different cases were simulated.

For both the particles and bubbles, a combined effect of the void fraction and the solids volume fraction was found on the drag coefficient. Using the simulation results, a drag correlation for both the bubbles and the particles was developed, which provides an accurate description for a void fraction between 15% and 50% and a solids volume fraction between 2% and 14%.

The currently used combined FT-IB method has problems with the calculation of the torque on the particles, as shown in chapter 3. Due to the error in the calculation of the torque, the particles acquire an unphysical rotation, which results in a higher surface velocity of the particle. The implementation of the torque in the second order implicit IB method should be improved, to ensure the accuracy of the method.

To broaden the range of applicability of the obtained correlations, the simulation range should be extended. In the current data set, a constant particle diameter and bubble diameter have been used. It is expected that the size of the particles and the bubbles and the ratio of the two will influence the drag coefficient. We note that the FT-IB method has difficulties with simulating a combination of bubbles with a relatively low surface tension and particles with a high inertia. It is expected that in such cases a particle will fall through a bubble, leading to the formation of a doughnut shaped bubble or even the break-up of the bubble. For these cases a break-up model would need to be incorporated. Another option is to combine the currently used FT model with the Volume of Fluid model, which prevents unphysical merging of the bubbles while break-up is incorporated in the model (Torres and Brackbill, 2000; Walker et al., 2013).

CUTTING BUBBLES WITH A SINGLE WIRE

6.1 Introduction

In dense bubbly flows, encountered in bubble column reactors, pronounced coalescence of bubbles prevails resulting in a decrease of the specific gas-liquid (g-l) interfacial area. By introducing micro-structuring in the column in the form of a wire mesh, the coalesced bubbles will be cut into smaller bubbles leading to an increased specific g-l interfacial area. The wire mesh will not only cut the bubbles, but also enhance the interface dynamics thereby enhancing the local mass transfer rate exactly at the desired position, i.e. near the catalytic surface of the wire mesh (Höller et al., 2001; Prasser et al., 2001; Ito et al., 2011).

In principle Computational Fluid Dynamics can be used to quantitatively describe the complex fluid-structure interaction in wire mesh bubble column contactors in terms of closures.

In this chapter, the interaction between a single bubble and the simplest form of a wire mesh will be studied. Because of the anticipated complex topological changes in the interface, i.e. bubble cutting, the Volume of Fluid (VoF) method is used. VoF can handle break-up of bubbles, and moreover, the method inherently conserves the bubble volume. The VoF method is coupled with the second order Immersed Boundary (IB) method of Deen et al. (2012) to describe the fluid-wire interaction. We choose this method, because it does not require calibration through the specification of an effective wire diameter and in comparison with other IB methods accurate results can be obtained at relatively low resolution.

Previous studies on bubble splitting mainly focused on the break-up of bubbles due to interplay with turbulence Liao and Lucas (2009). Only very few studies were carried out to

study the interaction of bubbles with stationary wires. Segers (2015) experimentally found that the wire diameter does not influence the bubble cutting, while the bubble cutting is enhanced with increasing bubble sizes and decreasing viscosity.

Although both the VoF method and the IB method have already been validated for two phase flows in chapter 2, 3 and 4, the combined VoF-IB model has to be validated using a number of well-defined experiments. Furthermore, the effect of the Eötvös number (Eo), the Morton number (Mo), the bubble rise velocity and the diameter of the wire will be determined. The chapter will start with an explanation of the used numerical method. Subsequently the combined VoF-IB method will be validated and the validated model will be used to determine the effect of the above mentioned parameters.

6.2 Numerical method

The simulations are performed using a combination of the VoF method of van Sint Annaland et al. (2005) and the second order implicit IB method of Deen et al. (2012), detailed in chapter 2 and 3 respectively. This chapter contains only a brief discussion of both models, focusing on the combination of the methods. In the combined VoF-IB method, the continuity equation, equation 6.1, and the Navier-Stokes equations, equation 6.2 are solved assuming incompressible flow.

$$\nabla \cdot \mathbf{u} = 0 \tag{6.1}$$

$$\rho \frac{\partial \mathbf{u}}{\partial t} = -\nabla p - \rho \nabla \cdot (\mathbf{u}\mathbf{u}) - \nabla \cdot \boldsymbol{\tau} + \rho \mathbf{g} + \mathbf{F}_\sigma \tag{6.2}$$

Because the velocity across the gas-liquid interface is continuous, the Navier-Stokes equations are solved using a one-field approximation. The surface tension due to the gas-liquid interface is introduced through an extra force density, $\mathbf{F}_\sigma$, that only acts in the vicinity of the interface. This force density is calculated with either the height function method or the tensile force method.

For simulations with Eo < 10, the force density is calculated with the height function method. This method is based on the Continuum Surface Force (CSF) method of Brackbill et al. (1992), which uses equation 6.3 to calculate the force density.

$$\mathbf{F}_\sigma = \sigma \kappa \mathbf{n} \tag{6.3}$$

The difference with the CSF method is in the calculation of the curvature, κ. The curvature is calculated from the spatial change of the surface height, h. The surface height is obtained from the summation of the phase fraction in the direction of the largest component of the

surface normal vector, which is evaluated using a 7x3x3 stencil around each interface cell. From the local change of the height, the curvature of the interface cell can be calculated with equation 6.4 (Gerrits, 2001; Cummins et al., 2005; Francois et al., 2006).

$$\kappa = \frac{\partial}{\partial x}\left(\frac{\frac{\partial h}{\partial x}}{\sqrt{1 + (\frac{\partial h}{\partial x})^2 + (\frac{\partial h}{\partial y})^2}}\right) + \frac{\partial}{\partial y}\left(\frac{\frac{\partial h}{\partial y}}{\sqrt{1 + (\frac{\partial h}{\partial x})^2 + (\frac{\partial h}{\partial y})^2}}\right) \tag{6.4}$$

Because a force density is needed in the calculation of the Navier-Stokes equation, the calculated force per unit surface area is multiplied by the area of the interface and divided by the volume of the cell.

According to the results presented in chapter 2, the tensile force method should be used for cases where Eo $\geq$ 1. In this method, the force density, $\mathbf{F}_\sigma$, is calculated by summing the tensile forces, that all neighboring interface segments exert on a certain central interface segment, using the reconstructed PLIC (Piecewise Linear Interface Calculation) description of the interface segments.

$$\mathbf{F}_{\sigma,m} = \frac{1}{2}\sigma \sum_{i=1}^{n}(\mathbf{t}_{i,m} \times \mathbf{n}_i) \tag{6.5}$$

Where m is the central interface segment, i is the index of the neighboring interface elements and n is the number of edges that depends on the PLIC reconstruction case of interface element m. Because there is no inherent connectivity between the interface segments in the VoF model, a neighboring cell may not contain any gas while one of the edges of element m might be located in the cell face between these two cells. In those cases, the tensile force exerted by such a neighboring cell is set to zero.

In the VoF model, the evaluation of the pressure gradient and the force density typically introduces an unbalance, which can be alleviated by the introduction of the so called pressure jump correction (Renardy and Renardy, 2002; Francois et al., 2006; Dijkhuizen et al., 2010b), which is given by:

$$[p] = \frac{\sum_i \mathbf{F}_{\sigma,i} \cdot \mathbf{n}_i}{\sum_i A_i} \tag{6.6}$$

The implementation of the no-slip boundary condition on the surface of the wire is performed at the level of the discretised Navier-Stokes equations, where each velocity component, ψ_c, can be related to its neighboring velocity components, ψ_{nb}, according to equation 6.7.

$$a_c\psi_c + \sum_{nb} a_{nb}\psi_{nb} = b_c \tag{6.7}$$

When a neighboring cell is located inside the wire, the coefficients of the associated velocity component are adjusted using a second order polynomial fit. By combining this fit with equation 6.7, the velocity component inside the wire can be eliminated whereas the coefficients of the two adjoining cells are adjusted using the wire velocity and the dimensionless distance to the surface. Because singularities are encountered when the surface of the wire is very close to the central cell, the method switches to a first order 1D fit when the dimensionless distance from the central grid cell is less than 0.0001.

The Navier-Stokes equations (equation 6.2) and the continuity equation (equation 6.1) are solved on a staggered grid using the (two-step) projection-correction method. In this method, first a tentative velocity field is computed from the Navier-Stokes equations excluding the pressure term. In the first step, all terms in the Navier-Stokes equations are treated explicitly, except for the diffusion term, which is treated implicitly with the exception of the mixed derivatives which are treated explicitly. The diffusion term is discretised using a second order central difference scheme, while the convective term is discretised using a flux-delimited Barton scheme. The resulting velocity field is corrected to satisfy the continuity equation. Both the implicit part of the diffusion equation and the pressure Poisson equation are solved using a block ICCG solver, which is parallelised using OpenMP.

The obtained velocity field is used to advect the phase fractions. Because in the VoF model only the phase fraction is known, the gas-liquid interface is reconstructed using the PLIC algorithm to enable an accurate surface representation of the bubble. The reconstructed interfaces are advected using the 3D geometrical advection of Youngs (1982), solving equation 6.8.

$$\frac{DF}{Dt} = \frac{\partial F}{\partial t} + \mathbf{u} \cdot \nabla F = 0 \qquad (6.8)$$

When the new phase fractions in all cells are known, the new macroscopic density and viscosity are calculated, using normal and harmonic averaging, respectively, where the phase fraction in the grid cell is used as a weighting factor.

6.3   Validation of the model

6.3.1   Experimental set-up

To validate the VoF-IB model, the interaction between a wire and a single bubble was studied experimentally in a square glass column of 0.2 m diameter and 1.2 m height. The studied bubble size is 7.26 mm, giving a ratio of the bubble diameter to the column diameter of 0.04. For these small ratios, confinement effects can be neglected (Clift et al., 1978). At a height of 14 cm, a single wire with a diameter of 3 mm is positioned horizontally in the column.

To control the bubble size, the bubbles are created in a spoon-shaped cap at the bottom of the column. The cap is a cylinder with a diameter of 10 mm that is moveable in the

Table 6.1: The average liquid properties of the water-glycerol mixture used in the experiments.

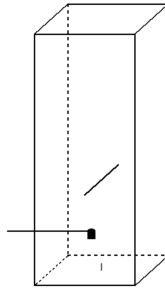| Property	Value	Unit
ρ_l	$1.25 \cdot 10^3$	kg/m^3
μ_l	1.13	$Pa \cdot s$
σ	$6.50 \cdot 10^{-2}$	N/m

Figure 6.1: A schematic overview of the set-up. The images are taken in the direction of the view.

horizontal direction (figure 6.1). The bubbles are created by injection of 0.2 mL of air, using a 0.5 mL syringe. To ensure the generation and rise of a single bubble in a quiescent liquid, a settling time of at least half an hour was taken into account before an individual experiment was performed.

The column is filled with a mixture of deminiralised water and glycerol, which was stirred using a continuous air flow for three days. To determine average properties of the resulting liquid at room temperature, six separate measurements were performed during the experiments, using a Brookfield DV-E viscometer for measuring the viscosity and K20 EasyDyne digital of Krüsse with the Wilhelmy plate method for measuring the surface tension. The average properties of the liquid mixture are given in table 6.1.

During the experiments, the bubble velocity, the bubble trajectory and the bubble volume are tracked using a high speed camera (Imager Pro HS CMOS camera with a resolution of 1280×1024 pixels). The recordings are performed with a frequency of 100 Hz and back lighting, which is only switched on during the imaging to reduce any heating of the liquid while illuminating the column. To diffuse the light, the back of the column is covered with a white plastic sheet. In total 18 experiments were performed to determine the bubble wire interactions.
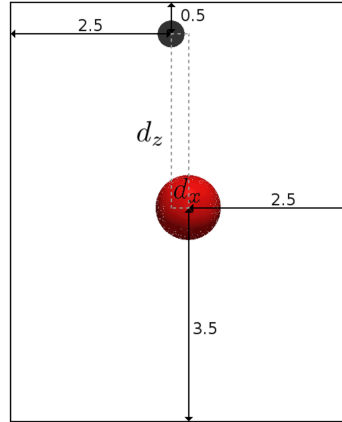
Figure 6.2: Initial positions of the bubble and the wire in the computational domain. The numbers indicate the distances between the bubble center of mass and the domain boundaries, normalized by the equivalent bubble diameter.

6.3.2   Numerical set-up

To enable a detailed comparison of the VoF-IB simulations and the experiments, 23 simulations were performed using the same liquid and gas properties and bubble and wire diameters, the details of which are listed in table 6.2. Because of the relatively high Eo, the tensile force method was used. The number of grid cells inside a bubble is 36, which ensures grid independent results for the bubbles as shown in chapter 2. Similarly, the results in chapter 3 show that 12 grid cells is sufficient to accurately determine the wire drag force and thus to enforce the no-slip condition. Therefore, the grid dependency studies where not repeated.

The boundary conditions for all the domain boundaries are set to free slip. Furthermore, window shifting is applied on the total phase fraction, to prevent bubbles to move out of the domain. As a result of that, the center of mass of the total phase fraction will remain very close to its original position in the domain, whereas the wire appears to be moving through the simulation domain (Deen et al., 2004). To ensure that the bubble rise is not affected by the size of the computational domain, the bubbles are positioned at least 2.5 bubble diameters from the domain boundaries, as illustrated in figure 6.2. The vertical distance between the bubble and the wire, d_z, is set to at least 3.5 bubble diameters to ensure the bubbles will reach their terminal rise velocity before interacting with the wire. For the different simulations, the horizontal difference between the center of mass of the bubble and the wire, d_x, was changed from 0 to 2 cm.

Table 6.2: Simulation settings and physical properties.

Property	Value	Unit
Domain size (nx,ny,nz)	$(180, 180...190, 235)$	grid cells
Grid size (Δx, Δy & Δz)	$2.00 \cdot 10^{-4}$	m
Time step	$1.0 \cdot 10^{-5}$	s
R_b	$3.63 \cdot 10^{-3}$	m
R_w	$1.50 \cdot 10^{-3}$	m
ρ_l	$1.25 \cdot 10^{3}$	kg/m^3
μ_l	1.13	Pa $\cdot$ s
ρ_g	1.20	kg/m^3
μ_g	$1.0 \cdot 10^{-5}$	Pa $\cdot$ s
σ	$6.5 \cdot 10^{-2}$	N/m
ρ_s	$2.0 \cdot 10^{3}$	kg/m^3

6.3.3 Bubble cutting and shape

The objective of this section is to validate whether the details of the cutting of bubbles is faithfully captured by the computational model. In both the experiments and the simulations, the effect of the obliqueness of the bubble wire interaction on the bubble cutting was studied. Bubble cutting was only found for bubbles that experience a straight impact. When the bubble starts slightly off center, the high liquid viscosity will ensure that the bubble passes the wire without being cut.

Figure 6.3 shows several snapshots of a straight bubble-wire interaction. The deformation of the bubble in the experiments and numerical simulations is very similar. For a straight impact, it was expected that the daughter bubbles would obtain approximately the same volume. However, both the experiments and the numerical simulations reveal an asymmetrical cutting. This asymmetry is introduced by a small asymmetry in the flow field when the bubble is close to the wire mesh. This results in a slightly smaller part of the bubble on one side of the wire, as shown in figure 6.3.c for the experiments and in figure 6.3.i for the simulations. The smaller part of the bubble will have a slightly higher pressure than the larger part of the bubble. Consequently, a partial depletion of the smaller bubble will occur, which increases with an increasing volume difference as shown for both the experiments and the simulation in figure 6.3.c to 6.3.e and figure 6.3.i to 6.3.k, respectively. The relatively high liquid viscosity leads to a relatively long contact time, and as a consequence there is a substantial difference between the bubble volumes on either side of the wire. Comparing the relative size of the bigger daughter bubble with respect to the mother bubble, the simulations give $d_1/d_0 = 0.903$, which matches well with the experimentally obtained results, where $d_1/d_0 = 0.944$, considering the experimental error of 2%.

To characterize the obliqueness of the bubble wire interaction, an impact parameter is
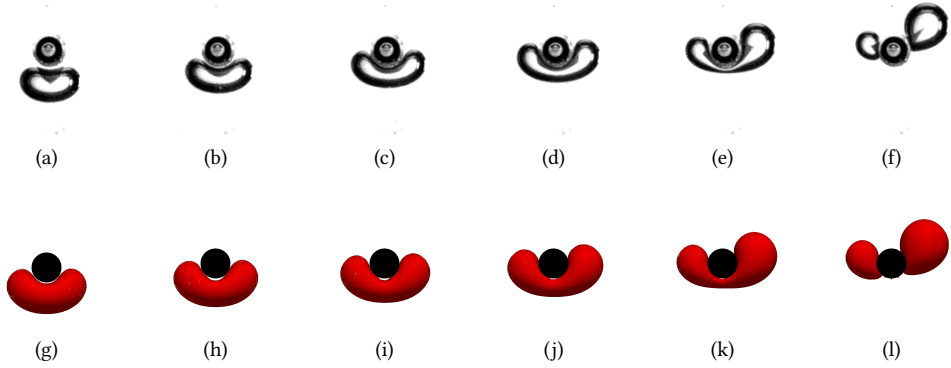
Figure 6.3: Snapshots of the straight impact of a bubble with a single wire. The upper row shows the experimental results while the lower row shows the simulation results. The time intervals between the snapshots is the same for the experimental results and the simulation results.

used, similar to what is customary for droplet-droplet interactions. It is defined as the ratio of the horizontal difference between the bubble and the wire, and the sum of the bubble and wire radii:

$$b = \frac{d_x}{R_b + R_w} \tag{6.9}$$

Figure 6.4 shows the bubble and wire interaction for a slightly oblique interaction, $b = 0.0146$. This figure shows that both in the experiments and the simulations no cutting was found. When the bubble interacts with the wire, it is curling around the wire similar to the result for a straight bubble-wire interaction. Because in this case the smaller part of the bubble, on the left side of the wire, is much smaller than the bigger part, the pressure in the smaller part will be higher. This results in a quick depletion of the smaller bubble, which leads to the passage of the entire bubble on the right side of the wire.

For both the straight and oblique impacts, satellite bubbles are formed. In the experiments, these bubbles can only be observed on the right side of the wire, which is due to the small angle of the camera. However, it is expected that these bubbles are actually formed on either side of the wire. Both the experimental results and the simulation results do not resolve those bubbles and the details of the associated deformation. The details of these satellite bubbles could be resolved in the simulations when adaptive mesh refinement is used.
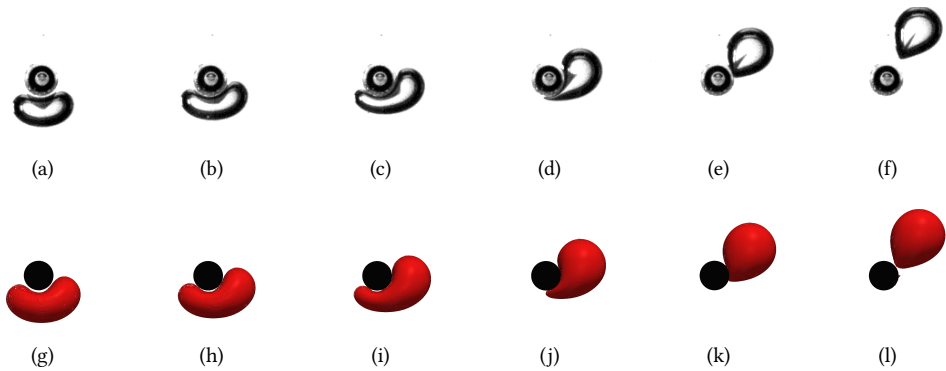
Figure 6.4: Snapshots of the oblique impact of a bubble with a single wire, $b = 0.0146$. The upper row shows the experimental results while the lower row shows the simulation results. The time intervals between the snapshots is the same for the experimental results and the simulation results.

6.3.4 Bubble trajectory

Apart from the bubble shape and size, the trajectory of the bubbles can also be evaluated as shown in figure 6.5. The figure shows that the numerical results, the lines, match well with the experimental results, the symbols, for both straight and oblique interactions.

Figure 6.5.a shows that for a straight impact the bubble does not change its trajectory until the center of mass is very close to the wire, at about 4 mm distance. Furthermore, in the simulations the bubble is cut when the center of mass of the mother bubble passed the top of the wire, whereas in the experiments the cutting takes place slightly earlier. This difference might be caused by the difficulties in experimentally recognizing the details around the wire, because a part of the wire is out of focus. Furthermore, the small angle in the pictures might also lead to difficulties in the determination of the exact moment of cutting.

When the approach of the bubble towards the wire is oblique, the bubble is deflected earlier, as shown in figure 6.5.b, 6.5.c and 6.5.d. Because these bubbles are deflected earlier, the bubbles will also move in a wider circle around the wire. This will result in an increase of the horizontal distance between the wire and the bubble after the wire interaction, which is also observed in both experiments and simulations.

6.3.5 Bubble rise velocity

Besides the bubble size, shape and trajectory, the effect of the bubble wire interaction on the bubble rise velocity can be determined. Figure 6.6 shows the bubble rise velocity of the bubble, normalized by the steady rise velocity. The normalization was done, because there is an expected small difference between the single bubble rise velocity as found in chapter 2.

(a) $b = 0.0000$

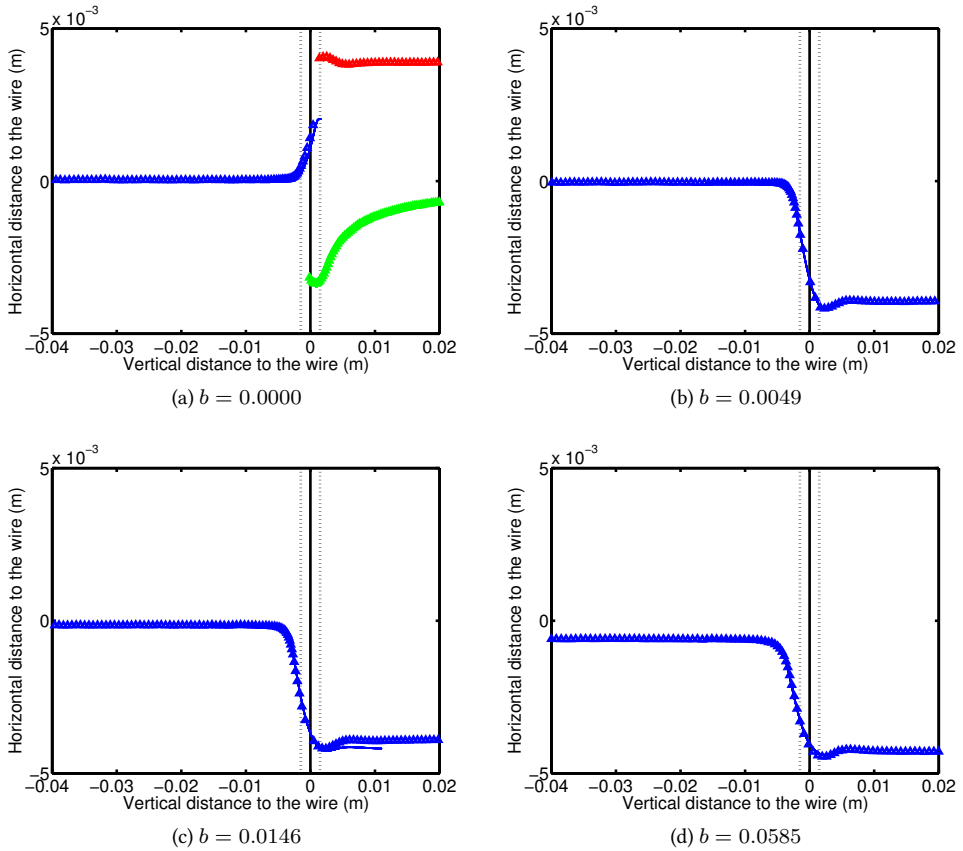(b) $b = 0.0049$

(c) $b = 0.0146$

(d) $b = 0.0585$

Figure 6.5: Comparison of the bubble trajectories for a straight impact and three different oblique impacts. The symbols in the figures are the experimental results, while the simulations are represented by the colored lines. The blue, red and green lines and symbols respectively represent the mother bubble, the large daughter bubble and the small daughter bubble. The black line represents the center of mass of the wire and the dotted black lines represent the bottom and the top of the wire.

(a) $b = 0.0000$

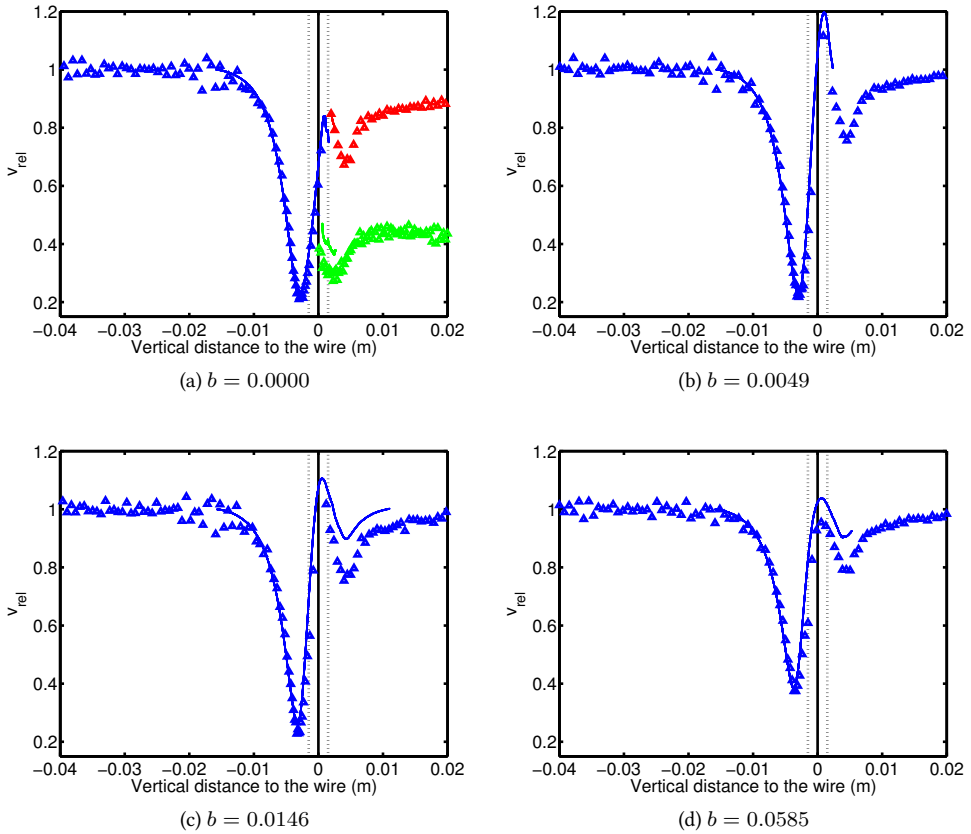(b) $b = 0.0049$

(c) $b = 0.0146$

(d) $b = 0.0585$

Figure 6.6: Bubble rise velocity for a straight impact and three different oblique impacts. The symbols in the figures are the experimental results, while the simulations are represented by the colored lines. The blue, red and green coloring of the lines and symbols represent the mother bubble, the large daughter bubble and the small daughter bubble. The black line represents the center of mass of the wire and the dotted black lines represent the wire radius.

The relative velocity is calculated by using the average steady rise velocity of the bubble before it starts interacting with the wire.

Figure 6.6.a shows that the combined VoF-IB method is able to accurately capture the velocity of the mother bubble and the large daughter bubble. The velocity of the smaller bubble is slightly overestimated by the model. It is noted that the spatial resolution is relatively low for the small bubble, i.e. only 23 numerical grid cells. Furthermore, in the experiments bubble recognition is difficult near the wire, and the image resolution for the small bubble is relatively low.

Figure 6.6.b-d shows the effect on the relative velocity for three different oblique interactions. The figures show a fairly good comparison between experimental and numerical results. Although the combined VoF-IB method overestimates the bubble rise velocity when the bubble is passing the wire, the velocity decrease prior to the impact is captured very accurately. Furthermore, the bubble rise velocity obtained numerically is following the same trend as the trends obtained in the experiments. The differences might be caused by ignoring wettability in the simulations.

In both experiments and simulations, the deceleration before the wire is decreasing with an increasing impact parameter. As a result of that, the acceleration of the bubble when the bubble is passing the wire is also decreased. Moreover, it can be seen that all passing bubbles recover their steady rise velocity.

6.4 Parameter study

6.4.1 Numerical Set-up

To determine the effect of the different physical parameters of the interaction of a single bubble with a single wire, similar settings are used as in the validation simulations that were presented in the previous section. The physical properties used in the parameter study are shown in table 6.3. The table shows two groups of simulation settings one at $\log(\text{Mo}) = 1$ and one at $\log(\text{Mo}) = -3$. In total, 60 extra simulations are performed.

The simulations use at least 15 grid cells in the diameter of the wire and 30 grid cells in the diameter of the bubble. These are both sufficient to ensure there is no grid dependency according to the results in chapter 2 and 3. The exact number of grid cells changes slightly among the different simulations.

6.4.2 Bubble cutting and shape

When the bubble approaches the wire in a straight manner, there are two possible outcomes of the bubble-wire interaction: the bubble is cut by the wire or the bubble gets stuck underneath the wire. In the current simulations, the viscosity of the liquid is much smaller than in the validation simulations. As a result, all the bubbles that get cut break up into two equally sized bubbles. Furthermore, tiny satellite bubbles are created at the bottom of the wire.

Table 6.3: Simulation settings and physical properties.

| Property	$\log \mathrm{Mo} = 1$	$\log \mathrm{Mo} = -3$	Unit
Domain size (nx,ny,nz)	$(180, 180...195, 235...240)$	$(180, 180...195, 235...240)$	grid cells
Grid size (Δx, Δy & Δz)	$9.67 \cdot 10^{-5}...2.16 \cdot 10^{-4}$	$5.42 \cdot 10^{-5}...2.16 \cdot 10^{-4}$	m
Time step	$1.0 \cdot 10^{-5}$	$1.0 \cdot 10^{-5}$	s
$\mathbf{g}_z$	-10	-10	m/s^2
d_b	$3.48 \cdot 10^{-3}...7.78 \cdot 10^{-3}$	$1.95 \cdot 10^{-3}...7.78 \cdot 10^{-3}$	m
d_w	$1.45 \cdot 10^{-3}...5.50 \cdot 10^{-3}$	$8.13 \cdot 10^{-4}...5.50 \cdot 10^{-3}$	m
ρ_l	$1.00 \cdot 10^3$	$1.00 \cdot 10^3$	kg/m^3
μ_l	$4.08 \cdot 10^{-1}$	$8.10 \cdot 10^{-2}$	Pa$\cdot$s
ρ_g	1.00	1.00	kg/m^3
μ_g	$2.0 \cdot 10^{-5}$	$2.0 \cdot 10^{-5}$	Pa$\cdot$s
σ	$3.02 \cdot 10^{-2}$	$7.56 \cdot 10^{-2}$	N/m
ρ_s	$2.0 \cdot 10^3$	$2.0 \cdot 10^3$	kg/m^3
Surface tension model	Tensile force method	Height function method	
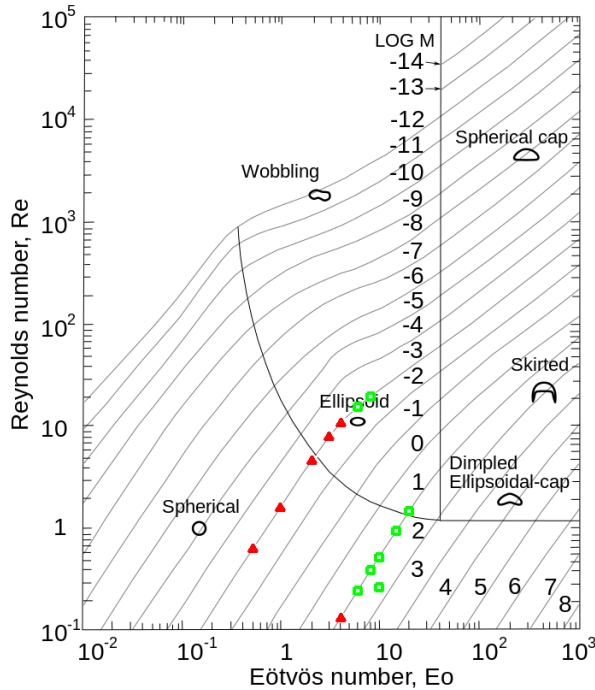
Figure 6.7: The effect of the Eo, Mo and Re numbers on the bubble cutting due to the inter-action with a single wire. The green squares represent bubbles that are cut while the red triangles represent bubbles that get stuck underneath the wire.

When the bubble gets stuck underneath the wire, the bubble moves towards the wire in the same way as when it gets cut. However, it does not deform sufficiently to actually get cut. The bubble then stabilizes into an ellipsoidal shape underneath the wire. After some time, the bubble obtains a small horizontal velocity, probably because of spurious currents. This will eventually push the bubble to one side such that it passes the wire. During its passage, the bubble is really close to the wire, which leads to the formation of some very small satellite bubbles.

Firstly, the effect of Eo was determined. Figure 6.7 shows that bubbles are only cut when Eo>4. Furthermore, the figure shows that Re and Mo do not influence the bubble cutting. All these simulations are performed with a bubble diameter that is 2.4 times the wire diameter.

To ensure that the bubble rise velocity does not influence the results, the bubble rise velocity upon impact was varied by decreasing the initial distance to the wire, d_z. In this way, the bubble rise velocity was varied between $0.70 - 1.0Re_\infty$. This did not change the cutting behavior of the bubbles, which can be caused by the small range in which the velocity was changed.

Finally, the relative size of the wire diameter was changed between $1.0-2.6d_b$. Although it is expected that the wire diameter will change the cutting behavior of the bubble, no effects are found for the simulated cases. It is expected that the bubble cutting is influenced for thinner wires ($d_b \gg 2.6d_w$) or thicker wires ($d_b < d_w$). To enable a more accurate analysis, the effect of Eo and the diameter of the wire on the bubble rise velocity will be determined in the next section.

6.4.3 Bubble rise velocity

Figure 6.8.a and b show the effect of Eo on the bubble rise velocity as it approaches the wire. Figure 6.8.a shows that the minimal rise velocity is obtained at the same distance from the wire. Furthermore, figure 6.8.b shows that the bubbles that are not cut (Eo ≤ 4) reach a zero velocity below the wire. Therefore, a correlation can probably be obtained for the bubble cutting based on the velocity of the bubbles, i.e. by adding an extra force to Newton's second law in the Euler-Lagrange models.

The effect of the wire diameter on the bubble rise velocity is shown in figure 6.8.c and d. The data reveal that the position where the bubble reaches the minimum rise velocity depends on the diameter of the wire. In addition, the obtained resistance of the wire depends on the diameter of the wire. Therefore, the diameter will eventually also influence the wire cutting. However, the range in which the wire diameter is varied in this work is not sufficient to draw definite conclusions.

6.5 Conclusion

In this chapter, our combined VoF-IB model was validated for the case of interaction of a single rising bubble with the simplest form of a wire mesh, i.e. a single static horizontal wire. Although the bubble rise velocity is slightly overestimated near the wire by our model, the bubble size, the bubble shape, the trajectory and the bubble rise velocity agree very well with the experimental observations.

Besides the validation of the VoF-IB model, the effect of the bubble size, the physical properties, the bubble velocity and the wire diameter was also studied. From the results, it can be concluded that the main influences on the bubble cutting can be captured with Eo and the relative wire diameter.

Nonetheless, there are several small differences between the experimental and numerical results, which can be decreased by improving both the experimental and the numerical methods. First of all, a glycerol-water mixture is used to create a liquid phase with a relatively high Morton number. However, the mixture has a high solubility for contaminants, which will lead to a more rigid bubble surface. This rigidity will influence the possibility to cut and may influence the dynamics of the liquid film between the bubble and the wire. To minimize the effect of contaminants experiments were performed in a short time frame. As a result only a limited number of experiments could be performed.
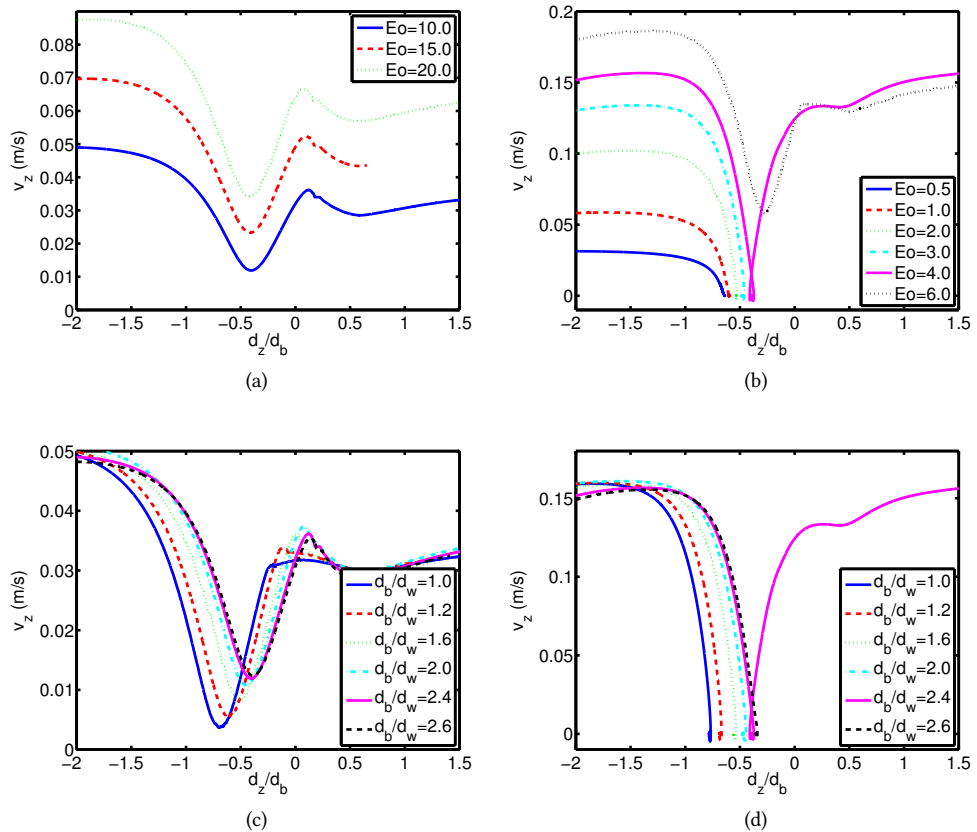
Figure 6.8: Velocity profiles of a bubble interacting with a single wire at different normalized distances between the bubble and the wire, d_z/d_b. Figure a and b show the effect of Eo for a constant value of the relative diameter of wire, $d_b/d_w = 2.4$, at respectively $\log(\text{Mo}) = 1$ and $\log(\text{Mo}) = -3$. Figure c and d show the effect of the relative thickness of the wire, for a bubble of Eo $= 10$ at $\log(\text{Mo}) = 1$ and Eo $= 4$ at $\log(\text{Mo}) = -3$, respectively.

Furthermore, the alignment of the camera with respect to the wire was not exactly straight. In this chapter, a correction was made to remove this error. However, the small imperfection will also partly block the view around the wire, resulting in uncertainties with respect to the measured bubble size and velocity near the wire. Moreover, the automation of the gas injection or a more accurate syringe will decrease the error in the injected gas volume. Finally, the accuracy of the experimental results could be raised by improving the bubble recognition, focusing on the coupling between the separate images and the recognition of the bubbles.

Because the experiments reveal that there is a small liquid layer around the wire, the computations do not include the wettability of the single wire. However, the simulations show some three-phase contacts when the bubbles are passing the wire. For this reason, the inclusion of the wettability might influence the bubble cutting and the subsequent bubble rise velocity after departure from the wire. The wettability can be included using a model for the contact angle and contact line propagation at the wire surface.

Although the simulations initially possess a very good resolution, the unequal cutting of the bubbles and the formation of satellite bubbles leads to a relatively low resolution for resolving the details of the smaller bubbles properly. To overcome this resolution problem, adaptive mesh refinement could be implemented, which ensures that all details of all bubbles are calculated accurately without a sharp increase in the computational time.

While some conclusions can already be drawn from the currently performed parameter study, the ranges in Eo, Mo and relative wire diameters are to small to derive quantitative closures for the Euler-Lagrangian models. Furthermore, the current ranges are not within the industrial relevant portion of the Grace diagram. In addition, the results obtained by Segers (2015) and the validation results showed that the relative horizontal position with respect to the wire influences the bubble cutting too. All these aspects should be taken into account in future work.

Cutting bubbles with a wire mesh

7.1 Introduction

Along the height of bubble columns, the specific gas-liquid interfacial area is typically reduced due to coalescence. To increase the specific interfacial area, a wire mesh can be introduced in the column to cut the large bubbles. Besides cutting the bubbles, the interaction between the wire mesh and the bubbles will also enhance the interface dynamics resulting in a higher surface renewal rate and consequently to higher mass transfer coefficients. The enhancement of surface renewal rate occurs at the desired position in case the wire mesh is coated with a catalyst (Höller et al., 2001; Prasser et al., 2001; Ito et al., 2011). Höller et al. (2001) showed that by implementing a similar approach a 10 times higher gas-liquid mass transfer coefficient was obtained in comparison to a bubble column without internals. However, the exact mechanism of break-up and the hydrodynamic interaction with the wire mesh is still unknown.

To design an optimal micro-structured bubble column, Computational Fluid Dynamics can be used. In the Euler-Euler and Euler-Lagrangian models, closures are needed to determine the interactions between the wire mesh and the bubbles (Jain et al., 2013). The closure proposed by Jain et al. (2013) is a basic geometrical closure for the bubble cutting. In this work, Direct Numerical Simulation (DNS) will be used to study the bubble wire mesh interaction.

In chapter 6, the combined Volume of Fluid Immersed Boundary (VoF-IB) method was validated by studying the interaction of a bubble with the simplest wire mesh, a single wire. Also the effects of the Eötvös number (Eo), the Morton number (Mo), the bubble velocity

and the diameter of the wire on the bubble cutting was determined. It was concluded that bubbles were only cut when Eo > 4.

In this chapter the interactions with a square wire mesh will be studied using the same VoF-IB method. In this chapter first the applied numerical method and the simulation set-up will be discussed. Subsequently, the interactions between a single bubble and a wire mesh will be studied for two limiting cases: i) a bubble hitting the center of an opening in the wire mesh, and ii) a bubble hitting the intersection of two wires in the mesh.

7.2   Numerical method

To study the interactions with a square wire mesh, a DNS model has been developed combining the VoF model of van Sint Annaland et al. (2005) and the IB method of Deen et al. (2012). In this chapter, only the main characteristics of the model are explained, detailed descriptions can be found respectively in chapters 2 and 3.

In the combined VoF-IB method the continuity equation, 7.1, and the Navier-Stokes equations, 7.2 are solved using a finite difference method assuming a one-field approach:

$$\nabla \cdot \mathbf{u} = 0 \tag{7.1}$$

$$\rho \frac{\partial \mathbf{u}}{\partial t} = -\nabla p - \rho \nabla \cdot (\mathbf{u}\mathbf{u}) - \nabla \cdot \boldsymbol{\tau} + \rho \mathbf{g} + \mathbf{F}_\sigma \tag{7.2}$$

Surface tension is accounted for through the force density $\mathbf{F}_\sigma$ included in the Navier-Stokes equations.

In the VoF model, different surface tension models can be used. According to chapter 2, the tensile force method is preferred for simulating bubbles with a relative high Eo and Mo, which will be used in this chapter. In the tensile force model, a force density is calculated for each cell containing an interface segment by summing the tensile forces, that are exerted by the neighboring interface segments on the reference element. The tensile forces are calculated using the edges of the interface segment resulting from the PLIC (Piecewise Linear Interface Calculation) interface representation:

$$\mathbf{F}_{\sigma,m} = \frac{1}{2}\sigma \sum_{i=1}^{n} (\mathbf{t}_{i,m} \times \mathbf{n}_i) \tag{7.3}$$

In this equation, m is the reference interface segment, i is the index of the neighboring interface elements and n is the number of edges that depends on the PLIC reconstruction case of interface element m. Because there is no inherent connectivity in the VoF model, a neighboring interface element might not contain an interface segment. For those cells, the exerted tensile stress is assumed to be zero.

Due to the mismatch in the discrete representation of the pressure gradient and the force density $\mathbf{F}_\sigma$, spurious currents will arise. To decrease this mismatch, the calculation of the surface tension and the pressure are coupled via an extra force density, or also called the "pressure jump correction", which is given in equation 7.4 (Renardy and Renardy, 2002; Francois et al., 2006; Dijkhuizen et al., 2010b).

$$\mathbf{F}_{\Delta p,m} = A_m \frac{\sum_i \mathbf{F}_{\sigma,i} \cdot \mathbf{n}_i}{\sum_i A_i} \tag{7.4}$$

The implementation of the no-slip boundary condition at the wire mesh is applied at the level of the discretised Navier-Stokes equations. At this level, a certain velocity component, ψ_c, can be expressed as a function of the velocity components in the neighboring cells, ψ_{nb}, according to equation 7.5.

$$a_c \psi_c + \sum_{nb} a_{nb} \psi_{nb} = b_c \tag{7.5}$$

When one of the neighboring cells is located inside the wire mesh, a second order accurate (1D) polynomial is fitted to represent the local velocity profile in terms of the velocity of the particle surface and the two velocities just outside the wire mesh. Using this polynomial fit, the velocity of the cell inside the wire mesh is eliminated from equation 7.5. Moreover, the coefficients of the other cells involved in the polynomial fit are changed according to the fit.

To solve equations 7.1 and 7.2, a projection-correction scheme is used. In this scheme, first a tentative velocity field is calculated. All terms in the momentum equations are solved explicitly except for the diffusion term, which is evaluated semi-implicitly. The implicit part of the diffusion term is chosen such that the velocity components can be solved separately whereas the mixed derivatives are evaluated explicitly. The diffusion term is discretised using a second order central difference scheme, while a flux-delimited Barton scheme is used for the convective term. Subsequently, the resulting velocity field is corrected to meet the continuity equation. Both the tentative velocity field and the pressure correction equation are solved using a block ICCG solver, which has been parallelised using OpenMP.

After the calculation of the velocity field, the new phase fraction in each cell can be determined. The gas-liquid interface is reconstructed using the PLIC algorithm and subsequently used to advect the liquid fraction according to the 3D geometrical advection scheme of Youngs (1982) using equation 7.6:

$$\frac{DF}{Dt} = \frac{\partial F}{\partial t} + \mathbf{u} \cdot \nabla F = 0 \tag{7.6}$$

When the new phase fraction is known, the new macroscopic density and viscosity can

Table 7.1: Simulation settings and physical properties.

Property	Value	Unit
Domain size (nx,ny,nz)	$(168...182, 168...182, 200)$	grid cells
Grid size (Δx, Δy & Δz)	$1.75 \cdot 10^{-4}$	m
Time step	$1.0 \cdot 10^{-5}$	s
d_b	$5.50 \cdot 10^{-3}$	m
d_w	$1.75 \cdot 10^{-3}$	m
d_b/s	$0.9 - 2.2$	
ρ_l	$1.00 \cdot 10^3$	kg/m^3
μ_l	$4.07 \cdot 10^{-1}$	Pa $\cdot$ s
ρ_g	1.00	kg/m^3
μ_g	$2.00 \cdot 10^{-5}$	Pa $\cdot$ s
σ	$3.02 \cdot 10^{-2}$	N/m
ρ_s	$2.00 \cdot 10^3$	kg/m^3

be calculated respectively using normal and harmonic averaging according to the phase fraction.

7.3   Simulation set-up

In this chapter, the interaction between a single rising bubble and a wire mesh is studied. The wire mesh was created by a combination of single wires with an axial orientation both in the x and y-direction. At the crossings the single wires overlap. A minimum domain size is required to prevent effects of the domain boundaries for the bubble rise. For a single bubble rising in an infinite liquid the domain width should at least be five times the bubble diameter. Besides, the domain boundary should either be at the middle of the wire or at the middle of the opening due to geometrical reasons. Taking both these criteria into account the total size of the simulation domain was determined.

Initially, a spherical bubble is placed at least 3.5 bubble diameters from the bottom of the domain, while the bubble was centered in the x- and y-direction, as shown in figure 7.1. The wire mesh is placed 0.6 bubble diameters from the top. In the first half of the simulations, the opening of the wire mesh was placed exactly above the bubble, while in the other half the center of the bubble was aligned with the crossing of the wire mesh.

All simulations are performed using free-slip boundary conditions enforced on all boundaries. Finally, the window shifting concept is applied, which will ensure that the average center of mass of the gas phase remains in its original position, while the wire mesh appears to be moving down through the domain (Deen et al., 2004).

Ten grid cells were used across the diameter of the wires, because the verification simulations in chapter 3 showed that this is sufficient to accurately model the drag force of a
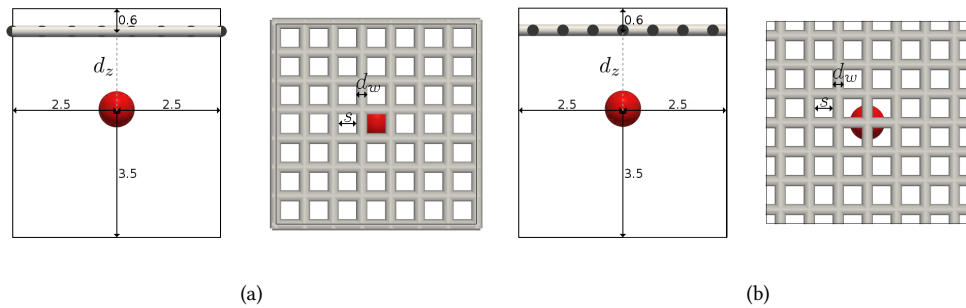
Figure 7.1: Initial positions of the bubble and the wires in the computational domain: a side view and a top view. The numbers indicate the distances between the bubble center of mass and the domain boundaries, normalized by the equivalent bubble diameter. Figure a shows the alignment of a bubble with the opening of the wire mesh, while figure b shows the alignment with the crossing of the wire mesh.

particle and thus the no-slip boundary condition. On the other hand, a minimum resolution is required for resolving the dynamics of the bubble. Previously, it was found that a minimum resolution of 20 grid cells across the bubble diameter is required. As we expect bubbles to be cut into smaller pieces the resolution of the initial bubble was increased to 31 grid cells across the bubble diameter.

In total 36 simulations are performed to determine the effect of Eo and the opening of the wire mesh, s. The physical properties and the other simulation settings are given in table 7.1. All simulations were conducted with a time step of $1.0 \cdot 10^{-5}$ s for a simulation time of 1s.

7.4 Interaction of a bubble with the center of a wire mesh opening

First of all, the interaction of a single bubble with the opening of a wire mesh was determined. According to the first approximation of Jain et al. (2013), the simulations with the three smallest openings ($d_b/s \geq 1.6$) should result in the cutting of the bubble into smaller bubbles. The bubbles in the other simulations, $d_b/s < 1.6$, would not be cut.

Figure 7.2 shows the different outcomes of the bubble wire mesh interactions obtained from these simulations. The figure shows that there is no cutting of the bubbles when the bubble is aligned with the opening. Large bubbles are just wobbling through the wire mesh. Due to their relatively high Eo, these bubbles are able to adequately deform and squeeze themselves through the wire mesh. This implies that a phenomenological model for bubble cutting on basis of solely geometrical considerations is not correct.
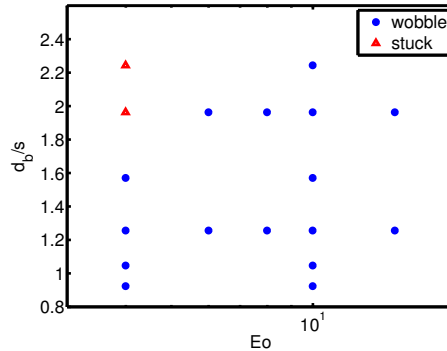
Figure 7.2: The effect of Eo and the opening in the wire mesh on the bubble wire interaction, when the bubble is aligned with the mesh opening in the horizontal direction.

Figure 7.3 shows the snapshots of a large bubble wobbling through the opening. When the ellipsoidal bubble is close to the wire mesh, the central portion of the bubble will move into the opening of the wire mesh as shown in figure 7.3.a and b. Because of the relatively high pressure at the part of the bubble underneath the wire mesh, these parts will be depleted. To pass the wire mesh, the bubble is strongly deformed as shown in figure 7.3.c. When the bubble leaves the wire mesh, figure 7.3.d and 7.3.e, the bubble is highly deformed, e.g. the bubble is elongated in the vertical direction while the horizontal size is similar to the pitch of the wire mesh. The effect of the bubble mesh on the bubble shape, is still visible when the bubble is well above the wire mesh, as shown in figure 7.3.f. Similar to the interaction with a single wire, which was shown in chapter 6, the interaction with the wire mesh will produce some satellite bubbles, as shown in figure 7.3.d-f. Because of the limited resolution the dynamics and size of these satellite bubbles cannot be properly resolved.

Unlike the large bubbles, the small bubbles (Eo $\leq$ 4) get stuck underneath the wire mesh. These smaller bubbles have a lower capability to deform. The mechanism of this formation of gas pockets below the mesh is shown in figure 7.4. The initial stage of the interaction of the wire mesh is identical to the one for the bubble with higher Eo (figure 7.4.a-d). However when the bubble starts moving through the mesh, the bubble cannot sufficiently deform to move through the mesh. The bubble starts to slow down and finally stops underneath the mesh, as shown in figure 7.4.e and f.

Besides the changes in shape and the interaction with the wire mesh, there are also effects of Eo and the mesh opening on the rise velocity of the bubbles, which are shown in figure 7.5. In all cases the velocity first drops as the bubble approaches the wire mesh, subsequently the bubble is accelerated as it squeezes through the mesh and finally retains its original steady rise velocity. Figure 7.5.a shows that, as expected, the bubble rise velocity is larger for larger values of Eo. Furthermore, all the bubbles have a minimal velocity at
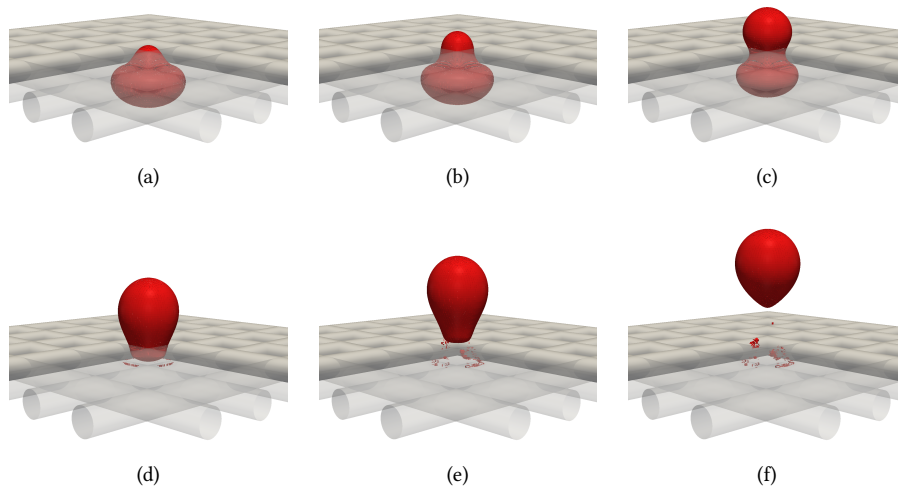
Figure 7.3: Snapshots of a bubble squeezing through a wire mesh after an inline approach to the center of the mesh opening (Eo = 10, $d_b/s = 2.0$).
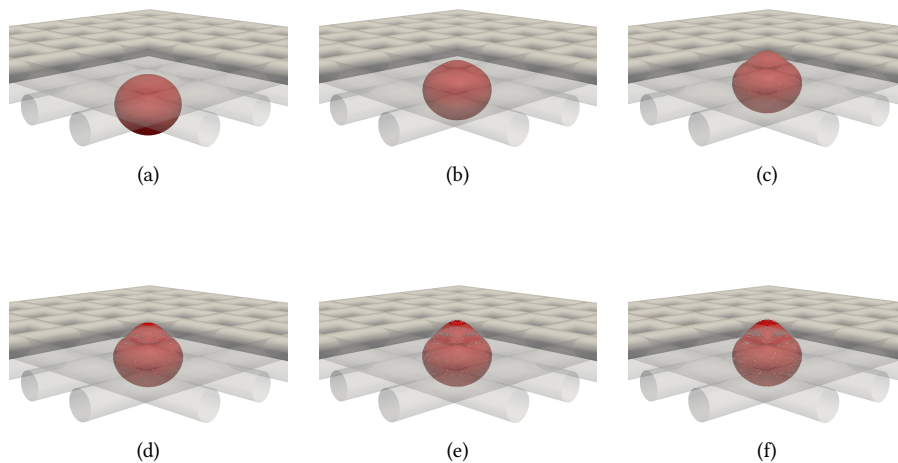

Figure 7.4: Snapshots of a bubble getting stuck underneath a wire mesh after an inline approach to the center of the mesh opening (Eo = 4, $d_b/s = 2.0$).
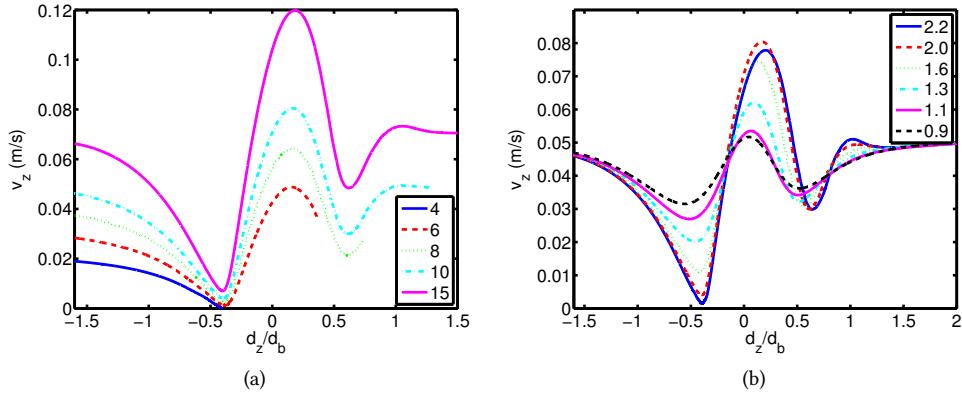
Figure 7.5: Velocity profiles of a bubble interacting with a wire mesh at different normalized distances between the bubble and the wire, d_z/d_b. (a): effect of Eo for a constant value of the mesh opening, $d_b/s = 2$. (b): effect of the mesh opening for a constant value of Eo $= 10$.

about 0.4 bubble diameters before the wire, which is similar to the results for a single wire as shown in chapter 6. When the bubble rise velocity is decreased to zero it simply gets stuck underneath the mesh. It can also be observed that the relative decrease in the bubble rise velocity depends on the bubble size.

Figure 7.5.b shows the effect of the wire mesh opening on the bubble rise velocity. As expected, with a larger opening the decrease in bubble rise velocity is less, i.e. the bubbles squeeze through more easily. The figure suggests that for mesh openings smaller than $0.45d_b$ the bubble will get stuck, even at high values of Eo $= 10$.

7.5   Straight interaction with a crossing of the wire mesh

Because the bubbles are not cut when they are aligned with the opening of the wire mesh, 18 simulations were done where the bubble is aligned with the crossing of two wires in the mesh. Figure 7.6 shows the effect of Eo and the opening of the wire mesh on the cutting of the bubbles. The figure shows that only large bubbles (Eo $= 15$) are cut by the wire mesh. All smaller bubbles are trapped underneath the wire mesh. In single wire simulations, a similar behavior was observed, as shown in chapter 6. However, the bubble size at which the bubbles get stuck is much smaller as was the case for single wires (Eo ≤ 4 instead of Eo ≤ 10). This can probably be explained by the larger drag exerted on the bubble by the wire mesh compared to the drag exerted by a single wire. Furthermore, the open area for
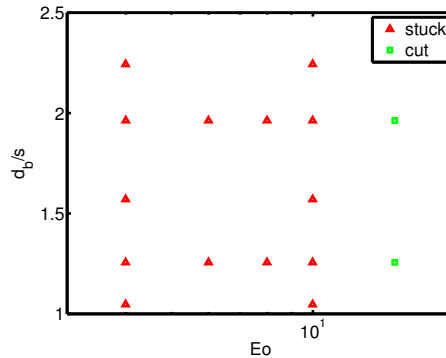
Figure 7.6: The effect of Eo and the mesh opening on the bubble mesh interaction, for the case that the bubble is aligned with the crossing of two wires.

the bubble to move through is finite for a wire mesh, whereas it is semi-infinite for a wire.

Comparing the results in figure 7.2 and 7.6, it is concluded that the behavior of the bubbles changes drastically when changing the alignment of the interaction. Hence, the interactions are not only influenced by the properties of the bubbles and the wire mesh, as stated before, but also on the positioning of the bubble with respect to the wire mesh.

The mechanism for a large bubble that gets stuck underneath the mesh is shown in figure 7.7. The bubble behavior is similar to the case where the bubble is aligned with the wire mesh opening. The bubble tries to move through the openings of the wire mesh, but is unable to reach the required curvature to facilitate bubble cutting due to the action of surface tension. Therefore, the bubble slows down and gets stuck underneath the wire mesh.

Figure 7.8 shows the cutting of bubble by the wire mesh. The bubble is cut because the rise velocity of the bubble is larger than zero when the bubble is very close to the wire mesh. Furthermore, the high value of Eo leads to a highly deformable gas-liquid interface enabling the bubble to curl around the wire mesh. The combination of these properties leads to the formation of four bubbles on all the sides of the wire crossing as shown in figure 7.8.d-f.

7.6   Conclusions

In this chapter, the combined VoF-IB method was successfully applied to simulate the interactions between bubbles and wire meshes. When the bubbles are aligned with the opening of the wire mesh, cutting of the bubbles is not observed in our simulations, while cutting was expected for the interactions with the meshes with the smallest openings. When Eo > 4, the bubbles are highly deformable and squeeze themselves through the opening of the wire mesh. When the bubble is smaller and/or the opening in the wire mesh is small the bubble gets stuck underneath the mesh. When the bubble is aligned with the crossing in a wire
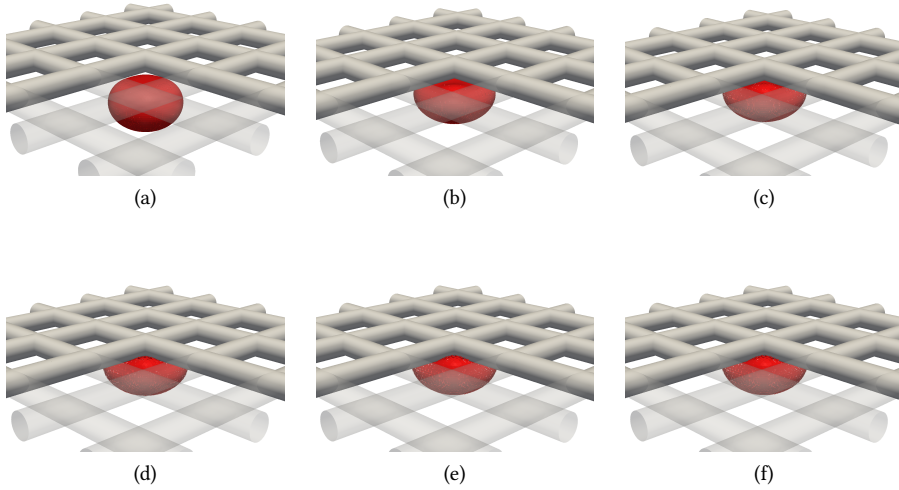
Figure 7.7: Snapshots of a bubble getting stuck underneath a wire mesh after an inline approach to the crossing of two wires (Eo $= 10$, $d_b/s = 1.3$).
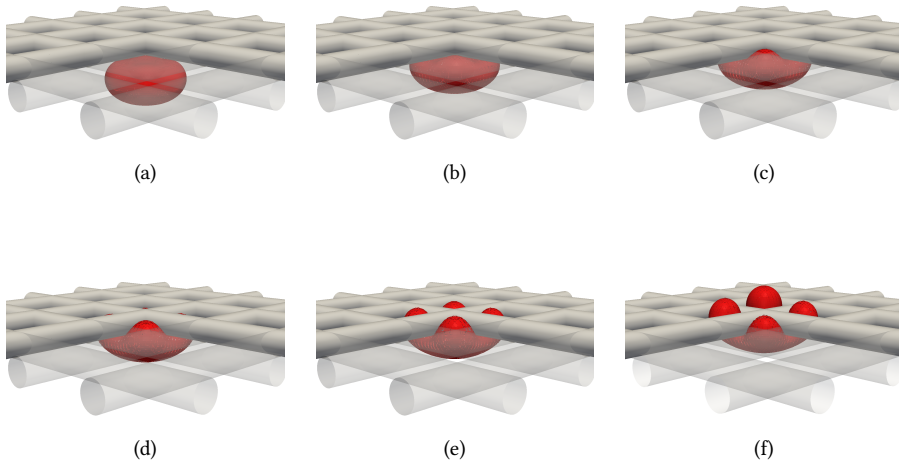

Figure 7.8: Snapshots of a bubble getting cut after an inline approach to the crossing of two wires (Eo $= 10$, $d_b/s = 1.3$).

mesh, almost all bubbles get stuck underneath the mesh except for the bubble with Eo = 15 which gets cut by the mesh.

Although the simulations confirm all the experimentally observed mechanisms for the interaction between a bubble and a wire mesh, the set of simulations does not yet allow for the derivation of an improved closure for the bubble cutting. To improve the preliminary geometrical bubble cutting closure of Jain et al. (2013), the effect of the relative position of the bubble with respect to the wire mesh and different Morton number should be determined. Furthermore, the diameter of the wires will also influence the efficiency of the bubble cutting. Therefore, the currently obtained data set should be extended to quantify the combined effects of these parameters. Finally, the set of mesh openings could be extended to even smaller openings to prove that larger bubbles will no longer squeeze themselves through at very small mesh openings.

Besides, the simulations are performed with only 31 grid cells across the bubble diameter. When a bubble is split into four bubbles, the resolution of the resulting bubbles is about 20 grid cells, which will lead to inaccuracies due to the low resolution. In addition, satellite bubbles are obtained in several simulations. To overcome these problems, adaptive mesh refinement should be implemented, which ensures that all details of all bubbles are calculated accurately preventing a sharp increase in the computational time.

Furthermore, all simulations show partially dewetting of the surface of the wire mesh. The simulations do not include this three-phase contact around the wire mesh. This three phase contact can be represented using a model for the contact angle propagation of the three-phase contact line.

Although the simulations show the experimentally observed mechanism and the simulation method has been validated for the interaction with a single wire (chapter 6), a direct comparison between the experimental system with more complex wires and the simulation method is still missing. To ensure the simulations have predictive capabilities, the interactions between bubbles and (more complex) meshes should also be validated.

CHAPTER

8

EPILOGUE

In the previous chapters, Direct Numerical Simulations (DNS) were used to study three-phase gas-liquid-solid flows. In chapter 5, the swarm effects in dispersed gas-liquid-solid flows was quantified in terms of the solids and bubble volume fractions. The results of this study were condensed in a correlation for the effective drag acting on the bubbles and the particles.

Chapter 6 and 7 describe the effect of a wire mesh on the bubble cutting. First of all, the three-phase interaction with the wire mesh was validated. Three different types of interaction were observed: i) a bubble can be cut by the wire mesh, ii) a bubble can get stuck underneath the wire mesh and iii) a bubble can squeeze through the opening of the wire mesh. The type of interaction depends on the Eötvös number (Eo), the wire diameter and the opening in the wire mesh. This implies that a simple phenomenological model for bubble cutting solely on basis of geometrical considerations will not be able to accurately capture the bubble-wire mesh interactions.

In this chapter some preliminary results and recommendations for future work are presented. First some recommendations are made for the DNS. Subsequently, some preliminary results will be discussed with respect to bubble cutting in a micro-structured bubble column, along with recommendations for future work.

8.1 Direct Numerical Simulation

Although the DNS results show a good comparison with experimental results in chapter 2, 3, 4 and 6, both the two-phase and three-phase DNS models can be further improved. First of all, when the Volume of Fluid (VoF) model is used, bubbles will automatically merge when

the interfaces of two bubbles are within a grid cell. Therefore, the VoF model in its current form is not suited to assess whether coalescence occurs or not. In addition, the used Front Tracking (FT) model cannot be used to study the coalescence or break-up of bubbles either unless it is extended with a subgrid model. These features can be solved by combining the VoF and FT model to obtain a model that prevents unphysical merging of the bubbles while break-up is incorporated, like is done in the work of Torres and Brackbill (2000) and Walker et al. (2013).

In addition, the spatial resolution in bubble-wire mesh interactions is not always sufficient to resolve all details of the bubbles in the combined VoF Immersed Boundary (IB) method. In spite of the high resolution at the beginning of the simulations, the formation of satellite bubbles and the unequal cutting of bubbles leads to a relatively low resolution available for describing these small bubbles. To solve this resolution problem, adaptive mesh refinement could be implemented to ensure that all details around small bubbles are resolved accurately without a prohibitive increase in computational time.

Even though the use of the second order implicit IB method is advised over the modified Uhlmann method, the method is not able to simulate freely moving particles at high particle Reynolds number (Re > 100), due to the appearance of unphysical rotation related to approximations in the calculation of the torque. This problem is caused by a small but critical error in the calculation of the surface area of the particles. Currently the surface area is calculated using the tangent plane. Although there is no analytical solution for the surface area of a sphere, an improvement in the numerical approximation of the surface area will already reduce this error drastically. This can for instance be done by subdividing cells containing an interface into many subcells and calculating the area using a separate tangent plane for each of the subcells.

Finally, all three-phase simulations in this work are performed without a subgrid model to account for the wettability of the solid objects, despite the fact that three-phase contacts were observed in all three-phase simulations. To improve the VoF-IB and FT-IB methods, a model for the contact angle and contact line propagation should be included.

8.2   The hydrodynamics of dispersed gas-liquid-solid flows

In chapter 5, only the effect of the void fraction and the solids volume fraction on the drag force were quantified. Preliminary results show that the bubble diameter also influences the drag coefficient of both the bubbles and the particles. The results for three-phase flow containing 3 mm bubbles and 1 mm particles show the same trends in the drag coefficient with respect to the void fraction as the results presented in chapter 5.

In addition, the preliminary results show that larger bubbles lead to lower drag coefficients for both the bubbles and the particles. Because only a small range of bubble diameters was simulated, this effect could not be introduced in the drag closures. In future work, the

combined effect of the void fraction, the solids volume fraction and the bubble diameter should be addressed.

In a bubble slurry column, the catalyst is dispersed as very fine particles ($d_b/d_p \approx 10 - 100$), while in the simulations relatively large particles were used ($d_b/d_p = 2$). To capture the effect of the catalyst particles in a real bubble slurry column, the diameter of the particles should be substantially decreased. The relative diameter of the particle will most likely influence the drag force acting on both the particles and the bubbles. Clearly, this puts challenges on the allowable number of computational grid cells, which can probably only be solved by applying adaptive grid refinement around the particles. Finally, the effect of different physical properties should be assessed.

8.3   Micro-structured bubble column

In chapter 6, the interaction of a bubble with the simplest form of a wire mesh, a single wire, was validated. To ensure that the VoF-IB model is able to accurately describe the interactions with more complex meshes, these interactions with more complex meshes should also be validated. Figure 8.1 shows some preliminary experimental results that can be used to carry out this validation. The experimental results are similar to the case shown in figure 8.2, except that the Morton number, Mo, is slightly lower in the experiment. Similar to the simulation, the bubble squeezes through the opening of the wire mesh. Furthermore, it can be observed that the deformation of the bubble is similar. This is a clear indication that the VoF-IB method is, at least in a qualitative sense, able to accurately describe the interaction. Nonetheless, to enable a quantitative validation of the model, the simulations need to be performed with the same experimental settings. Moreover, different horizontal orientations with respect to the wire mesh should be used for the validation.

In chapter 6 and 7 it was shown that the bubble cutting is mainly influenced by Eo, the wire diameter and the opening in the wire mesh. However, there was insufficient data to derive a fully predictive correlation for the bubble cutting over a wide range of conditions. The velocity graphs in both chapters show that bubble cutting only occurs upon straight impact as long as the bubble is not decelerated to zero velocity. Therefore, it is expected that the bubble cutting can be described on basis of the bubble rise velocity. Preliminary results show that the wire mesh exerts a force on the bubble that depends on the distance to the wire mesh, the bubble diameter, the approach velocity, the diameter of wires and the opening of the wire mesh. The exerted force has a maximum for all the simulations at a distance of $(0.5d_w + 0.2d_b)$. In addition, this force increases with increasing wire diameter and decreasing opening in the wire mesh. In order to derive a correlation, the simulated range should be extended by varying the wire diameter, Eo, Mo and the position of the bubble with respect to the wire mesh.

When the bubble-wire mesh interaction is validated and a correlation is obtained for single bubbles, the current study should be extended to cases with multiple bubbles. It is expected that the interaction with other bubbles will lead to preferred paths through the
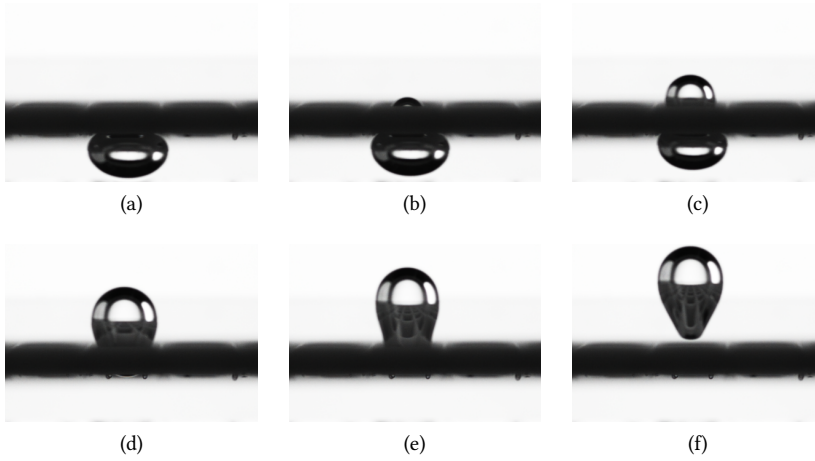
Figure 8.1: Preliminary results on a bubble squeezing through a wire mesh after an inline approach to the center of the mesh opening (Eo $=$ 10, log(Mo) $=$ 0.44, $d_b/s =$ 1.8, $d_b/d_w =$ 2.5). Note that the wire mesh is blurred in the images, because large parts of it are out of focus.
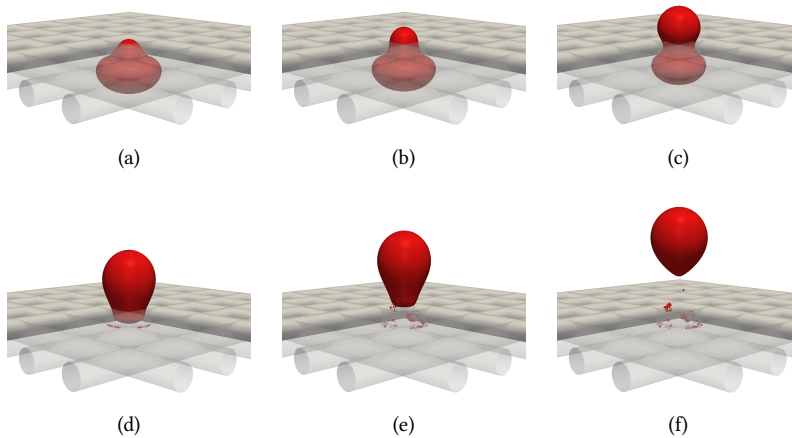

Figure 8.2: Snapshots of a bubble squeezing through a wire mesh after an inline approach to the center of the mesh opening (Eo $=$ 10, log(Mo) $=$ 1.0, $d_b/s =$ 2.0, $d_b/d_w =$ 2.4). This figure was reproduced from figure 7.3.

mesh, which will decrease the efficiency of the bubble cutting if the path is moving through the opening of the wire mesh. However, the bubble interactions will also lead to an increase in the approach velocity of the bubbles and therefore better cutting. In addition, the bubbles that get stuck beneath the wire mesh might pass the wire mesh due to interactions with other bubbles.

References

Afkhami, S., Bussmann, M., 2009. Height functions for applying contact angles to 3D VoF simulations. International Journal for Numerical Methods in Fluids 61 (8), 827–847.

Albadawi, A., Donoghue, D. B., Robinson, A. J., Murray, D. B., Delauré, Y. M. C., 2013. On the analysis of bubble growth and detachment at low Capillary and Bond numbers using Volume of Fluid and Level Set methods. Chemical Engineering Science 90, 77–91.

Albert, C., Raach, H., Bothe, D., 2012. Influence of surface tension models on the hydrodynamics of wavy laminar falling films in Volume of Fluid-simulations. International Journal of Multiphase Flow 43, 66–71.

Apelt, C. J., 1958. The steady flow of a viscous fluid past a circular cylinder at Reynolds numbers 40 and 44. Aeronautical Research Council Reports & Memoranda.

Aulisa, E., Manservisi, S., Scardovelli, R., Zaleski, S., 2003. A geometrical area-preserving Volume-of-Fluid advection method. Journal of Computational Physics 192 (1), 355–364.

Beetstra, R., van der Hoef, M. A., Kuipers, J. A. M., 2007. Drag force of intermediate Reynolds number flow past mono- and bidisperse arrays of spheres. AIChE Journal 53 (2), 489–501.

Bird, R. B., Stewart, W. E., Lightfoot, E. N., 2007. Transport Phenomena, 2nd Edition. John Wiley & Sons, Inc.

Brackbill, J. U., Kothe, D. B., Zemach, C., 1992. A continuum method for modeling surface tension. Journal of Computational Physics 100 (2), 335–354.

Bunner, B., Tryggvason, G., 2002. Dynamics of homogeneous bubbly flows part 1. rise velocity and microstructure of the bubbles. Journal of Fluid Mechanics 466, 17–52.

Chang, Y. C., Hou, T. Y., Merriman, B., Osher, S., 1996. A Level Set formulation of eulerian interface capturing methods for incompressible fluid flows. Journal of Computational Physics 124 (2), 449–464.

Chesshire, G., Henshaw, W. D., 1990. Composite overlapping meshes for the solution of partial differential equations. Journal of Computational Physics 90 (1), 1–64.

Clift, R., Grace, J. R., Weber, M. E., 1978. Bubbles, drops and particles. Academic Press, New York.

Cummins, S. J., Francois, M. M., Kothe, D. B., 2005. Estimating curvature from volume fractions. Computers & Structures 83 (6-7), 425–434.

Deen, N. G., Kriebitzsch, S. H. L., van der Hoef, M. A., Kuipers, J. A. M., 2012. Direct Numerical Simulation of flow and heat transfer in dense fluid-particle systems. Chemical Engineering Science 81, 329–344.

Deen, N. G., Kuipers, J. A. M., 2013. Direct Numerical Simulation of fluid flow and mass transfer in dense fluid-particle systems. Industrial and Engineering Chemistry Research 52 (33), 11266–11274.

Deen, N. G., Kuipers, J. A. M., 2014. Direct Numerical Simulation (DNS) of mass, momentum and heat transfer in dense fluid-particle systems. Current Opinion in Chemical Engineering 5, 84–89.

Deen, N. G., Peters, E. A. J. F., Padding, J. T., Kuipers, J. A. M., 2014. Review of Direct Numerical Simulation of fluid-particle mass, momentum and heat transfer in dense gas-solid flows. Chemical Engineering Science 116, 710–724.

Deen, N. G., van Sint Annaland, M., Kuipers, J. A. M., 2004. Multi-scale modeling of dispersed gas-liquid two-phase flow. Chemical Engineering Science 59 (8-9), 1853–1861.

Deen, N. G., van Sint Annaland, M., Kuipers, J. A. M., 2009. Direct Numerical Simulation of complex multi-fluid flows using a combined Front Tracking and Immersed Boundary method. Chemical Engineering Science 64 (9), 2186–2201.

Dijkhuizen, W., Roghair, I., van Sint Annaland, M., Kuipers, J. A. M., 2010a. DNS of gas bubbles behaviour using an improved 3D Front Tracking model–drag force on isolated bubbles and comparison with experiments. Chemical Engineering Science 65 (4), 1415–1426.

Dijkhuizen, W., Roghair, I., van Sint Annaland, M., Kuipers, J. A. M., 2010b. DNS of gas bubbles behaviour using an improved 3D Front Tracking model–model development. Chemical Engineering Science 65 (4), 1427–1437.

Feng, Z.-G., Michaelides, E. E., 2005. Proteus: A direct forcing method in the simulations of particulate flows. Journal of Computational Physics 202 (1), 20–51.

Francois, M. M., Cummins, S. J., Dendy, E. D., Kothe, D. B., Sicilian, J. M., Williams, M. W., 2006. A balanced-force algorithm for continuous and sharp interfacial surface tension models within a volume tracking framework. Journal of Computational Physics 213 (1), 141–173.

Ge, Y., Fan, L.-S., 2006. 3-D Direct Numerical Simulation of gas-liquid and gas-liquid-solid flow systems using the Level-Set and Immersed-Boundary methods. Advances in Chemical Engineering 31, 1–63.

Gerlach, D., Tomar, G., Biswas, G., Durst, F., 2006. Comparison of Volume-of-Fluid methods for surface tension-dominant two-phase flows. International Journal of Heat and Mass Transfer 49 (3-4), 740–754.

Gerrits, J., 2001. Dynamics of liquid-filled spacecraft. Ph.D. thesis, University of Groningen.

Glowinski, R., Pan, T. W., Hesla, T. I., Joseph, D. D., Périaux, J., 2001. A fictitious domain approach to the Direct Numerical Simulation of incompressible viscous flow past moving rigid bodies: Application to particulate flow. Journal of Computational Physics 169 (2), 363–426.

Grace, J. R., 1973. Shapes and velocities of bubbles rising in infinite liquids. Transactions of the Institution of Chemical Engineers 51, 116–120.

Grace, J. R., Wairegi, T., Nguyen, T. H., 1976. Shapes and velocities of single drops and bubbles moving freely through immiscible liquids. Transactions of the Institution of Chemical Engineers 54, 167–173.

Harper, J. F., 1997. Bubbles rising in line: Why is the first approximation so bad? Journal of Fluid Mechanics 351, 289–300.

Hasimoto, H., 1959. On the periodic fundamental solutions of the Stokes equations and their application to viscous flow past a cubic array of spheres. Journal of Fluid Mechanics 5 (2), 317–328.

Henshaw, W. D., Schwendeman, D. W., 2003. An adaptive numerical scheme for high-speed reactive flow on overlapping grids. Journal of Computational Physics 191 (2), 420–447.

Höller, V., Radevik, K. S., Kiwi-Minsker, L., Renken, A., 2001. Bubble columns staged with structured fibrous catalytic layers: Residence time distribution and mass transfer. Industrial and Engineering Chemistry Research 40 (6), 1575–1579.

Hoomans, B. P. B., Kuipers, J. A. M., Briels, W. J., van Swaaij, W. P. M., 1996. Discrete Particle simulation of bubble and slug formation in a two-dimensional gas-fluidised bed: A hard-sphere approach. Chemical Engineering Science 51 (1), 99–118.

Hooshyar, N., van Ommen, J. R., Hamersma, P. J., Sundaresan, S., Mudde, R. F., 2013. Dynamics of single rising bubbles in neutrally buoyant liquid-solid suspensions. Physical Review Letters 110 (24), 244501.

Hu, H. H., 1996. Direct simulation of flows of solid-liquid mixtures. International Journal of Multiphase Flow 22 (2), 335–352.

Hu, H. H., Joseph, D. D., Crochet, M. J., 1992. Direct simulation of fluid particle motions. Theoretical and Computational Fluid Dynamics 3 (5), 285–306.

Hua, J., Lou, J., 2006. Simulation of single bubble rising in liquid using Front Tracking method. WIT Transactions on Engineering Sciences 52, 79–88.

Ito, D., Prasser, H.-M., Kikura, H., Aritomi, M., 2011. Uncertainty and intrusiveness of three-layer wire-mesh sensor. Flow Measurement and Instrumentation 22 (4), 249–256.

Jafari, A., Shirani, E., Ashgriz, N., 2007. An improved three-dimensional model for interface pressure calculations in free-surface flows. International Journal of Computational Fluid Dynamics 21 (2), 87–97.

Jain, D., Deen, N. G., Kuipers, J. A. M., Antonyuk, S., Heinrich, S., 2012. Direct Numerical Simulation of particle impact on thin liquid films using a combined Volume of Fluid and Immersed Boundary method. Chemical Engineering Science 69 (1), 530–540.

Jain, D., Lau, Y. M., Kuipers, J. A. M., Deen, N. G., 2013. Discrete Bubble Modeling for a micro-structured bubble column. Chemical Engineering Science 100, 496–505.

Kajishima, T., Takiguchi, S., 2002. Interaction between particle clusters and particle-induced turbulence. International Journal of Heat and Fluid Flow 23 (5), 639–646.

Kantarci, N., Borak, F., Ulgen, K. O., 2005. Bubble column reactors. Process Biochemistry 40 (7), 2263–2283.

Kawaguti, M., 1953. Numerical solution of the Navier-Stokes equations for the flow around a circular cylinder at Reynolds number 40. Journal of the Physical Society of Japan 8 (6), 747–757.

Kempe, T., Fröhlich, J., 2012. An improved Immersed Boundary method with Direct Forcing for the simulation of particle laden flows. Journal of Computational Physics 231 (9), 3663–3684.

Kitagawa, A., Sugiyama, K., Murai, Y., 2004. Experimental detection of bubble-bubble interactions in a wall-sliding bubble swarm. International Journal of Multiphase Flow 30 (10), 1213–1234.

Kuprat, A., Khamayseh, A., George, D., Larkey, L., 2001. Volume conserving smoothing for piecewise linear curves, surfaces, and triple lines. Journal of Computational Physics 172, 99–118.

Kurtoglu, I. O., Lin, C.-L., 2006. Lattice Boltzmann study of bubble dynamics. Numerical Heat Transfer, Part B: Fundamentals 50 (4), 333–351.

Kwakkel, M., Breugem, W.-P., Boersma, B. J., 2012. An efficient multiple marker front-capturing method for two-phase flows. Computers & Fluids 63, 47–56.

Ladd, A. J. C., 7 1994. Numerical simulations of particulate suspensions via a discretized Boltzmann equation. part 2. numerical results. Journal of Fluid Mechanics 271, 311–339.

Lafaurie, B., Nardone, C., Scardovelli, R., Zaleski, S., Zanetti, G., 1994. Modelling merging and fragmentation in multiphase flows with SURFER. Journal of Computational Physics 113 (1), 134–147.

Lamb, H., 1932. Hydrodynamics, sixth Edition. Cambridge University Press, London.

Li, Y., Yang, G. Q., Zhang, J. P., Fan, L.-S., 2001. Numerical studies of bubble formation dynamics in gas-liquid-solid fluidization at high pressures. Powder Technology 116 (2-3), 246–260.

Liao, Y., Lucas, D., 2009. A literature review of theoretical models for drop and bubble breakup in turbulent dispersions. Chemical Engineering Science 64, 3389–3406.

Lin, S.-Y., Chin, Y.-H., Wu, C.-M., Li, J.-F., Chen, Y.-C., 2012. A pressure correction-Volume of Fluid method for simulation of two-phase flows. International Journal for Numerical Methods in Fluids 68 (2), 181–195.

Meier, M., Yadigaroglu, G., Smith, B. L., 2002. A novel technique for including surface tension in PLIC-VOF methods. European Journal of Mechanics - B/Fluids 21 (1), 61–73.

Mittal, R., Iaccarino, G., 2005. Immersed Boundary methods. Annual Review of Fluid Mechanics 37, 239–261.

Mordant, N., Pinton, J.-F., 2000. Velocity measurement of a settling sphere. European Physical Journal B 18 (2), 343–352.

Nagrath, S., Jansen, K. E., Lahey Jr., R. T., 2005. Computation of incompressible bubble dynamics with a stabilized finite element Level Set method. Computer Methods in Applied Mechanics and Engineering 194 (42-44), 4565–4587.

Nishioka, M., Sato, H., 1974. Measurements of velocity distributions in the wake of a circular cylinder at low Reynolds numbers. Journal of Fluid Mechanics 65 (1), 97–112.

Peskin, C. S., 1977. Numerical analysis of blood flow in the heart. Journal of Computational Physics 25 (3), 220–252.

Peskin, C. S., 2002. The Immersed Boundary method. Acta Numerica 11, 479–517.

Pilliod Jr., J. E., Puckett, E. G., 2004. Second-order accurate Volume-of-Fluid algorithms for tracking material interfaces. Journal of Computational Physics 199 (2), 465–502.

Popinet, S., 2009. An accurate adaptive solver for surface-tension-driven interfacial flows. Journal of Computational Physics 228 (16), 5838–5866.

Prasser, H.-M., Scholz, D., Zippe, C., 2001. Bubble size measurement using wire-mesh sensors. Flow Measurement and Instrumentation 12 (4), 299–312.

Raessi, M., Mostaghimi, J., Bussmann, M., 2010. A Volume-of-Fluid interfacial flow solver with advected normals. Computers & Fluids 39 (8), 1401–1410.

Ramírez-Muñoz, J., Salinas-Rodríguez, E., Soria, A., Gama-Goicochea, A., 2011. Hydrodynamic interaction on large-Reynolds-number aligned bubbles: Drag effects. Nuclear Engineering and Design 241 (7), 2371–2377.

Renardy, Y., Renardy, M., 2002. PROST: A parabolic reconstruction of surface tension for the Volume-of-Fluid method. Journal of Computational Physics 183 (2), 400–421.

Rider, W. J., Kothe, D. B., 1998. Reconstructing volume tracking. Journal of Computational Physics 141, 112.

Roghair, I., 2012. Direct Numerical Simulations of hydrodynamics and mass transfer in dense bubbly flows. Ph.D. thesis, Eindhoven, University of Technology.

Roghair, I., Baltussen, M. W., van Sint Annaland, M., Kuipers, J. A. M., 2013a. Direct Numerical Simulations of the drag force of bi-disperse bubble swarms. Chemical Engineering Science 95, 48–53.

Roghair, I., Lau, Y. M., Deen, N. G., Slagter, H. M., Baltussen, M. W., van Sint Annaland, M., Kuipers, J. A. M., 2011. On the drag force of bubbles in bubble swarms at intermediate and high reynolds numbers. Chemical Engineering Science 66, 3204–3211.

Roghair, I., van Sint Annaland, M., Kuipers, J. A. M., 2013b. Drag force and clustering in bubble swarms. AIChE Journal 59 (5), 1791–1800.

Rubinow, S. I., Keller, J. B., 11 1961. The transverse force on a spinning sphere moving in a viscous fluid. Journal of Fluid Mechanics 11, 447–459.

Ruzicka, M. C., 2000. On bubbles rising in line. International Journal of Multiphase Flow 26 (7), 1141–1181.

Scardovelli, R., Zaleski, S., 1999. Direct Numerical Simulation of free-surface and interfacial flow. Annual Review of Fluid Mechanics 31, 567.

Segers, Q. I. E., 2015. Cutting bubbles using wire mesh structures, Direct Numerical Simulations. Ph.D. thesis, Eindhoven, University of Technology.

Segers, Q. I. E., Kuipers, J. A. M., Deen, N. G., 2013. Immersed Boundary method applied to single phase flow past crossing cylinders. Chemical Engineering Science 100, 33–38.

Shin, S., Juric, D., 2002. Modeling three-dimensional multiphase flow using a level contour reconstruction method for Front Tracking without connectivity. Journal of Computational Physics 180, 427–470.

Son, G., 2003. Efficient implementation of a coupled Level-Set and Volume-of-Fluid method for three-dimensional incompressible two-phase flows. Numerical Heat Transfer, Part B: Fundamentals 43 (6), 549–565.

Takami, H., Keller, H. B., 1969. A methodology for highly accurate results of Direct Numerical Simulations: Drag force in dense gas-solid flows at intermediate Reynolds number. Physics of Fluids Supplement II 12, 51–56.

Tang, Y., Kriebitzsch, S. H. L., Peters, E. A. J. F., van der Hoef, M. A., Kuipers, J. A. M., 2014. A methodology for highly accurate results of Direct Numerical Simulations: Drag force in dense gas-solid flows at intermediate Reynolds number. International Journal of Multiphase Flow 62, 73–86.

Tang, Y., Peters, E. A. J. F., Kuipers, J. A. M., Kriebitzsch, S. H. L., van der Hoef, M. A., 2015. A new drag correlation from fully resolved simulations of flow past monodisperse static arrays of spheres. AIChE Journal 61 (2), 688–698.

ten Cate, A., Nieuwstad, C. H., Derksen, J. J., van den Akker, H. E. A., 2002. Particle imaging velocimetry experiments and Lattice-Botlzmann simulations on a single sphere settling under gravity. Physics of Fluids 14 (11), 4012–4025.

Tomiyama, A., 1998. Struggle with computational bubble dynamics. In: Third International Conference on Multiphase Flow. pp. 369–405.

Torres, D. J., Brackbill, J. U., 2000. The Point-Set method: Front-Tracking without connectivity. Journal of Computational Physics 165 (2), 620–644.

Tritton, D. J., 1959. Experiments on the flow past a circular cylinder at low Reynolds numbers. Journal of Fluid Mechanics 6, 547–567.

Tryggvason, G., Bunner, B., Esmaeeli, A., Juric, D., Al-Rawahi, N., Tauber, W., Han, J., Nas, S., Jan, Y. J., 2001. A Front-Tracking method for the computations of multiphase flow. Journal of Computational Physics 169 (2), 708–759.

Uhlmann, M., 2005. An Immersed Boundary method with Direct Forcing for the simulation of particulate flows. Journal of Computational Physics 209, 448–476.

Unverdi, S. O., Tryggvason, G., 1992. A Front-Tracking method for viscous, incompressible, multi-fluid flows. Journal of Computational Physics 100 (1), 25–37.

van Sint Annaland, M., Deen, N. G., Kuipers, J. A. M., 2003. Multi-level modeling of dispersed gas-liquid two-phase flows. Heat and mass transfer. Springer, Berlin (edited by M. Sommerfeld and D. Mewes).

van Sint Annaland, M., Deen, N. G., Kuipers, J. A. M., 2005. Numerical simulation of gas bubbles behaviour using a three-dimensional Volume of Fluid method. Chemical Engineering Science 60 (11), 2999–3011.

van Sint Annaland, M., Dijkhuizen, W., Deen, N. G., Kuipers, J. A. M., 2006. Numerical simulation of behavior of gas bubbles using a 3-D Front-Tracking method. AIChE Journal 52, 99–110.

Walker, E., Nikitopoulos, D., Tromeur-Dervout, D., 2013. Parallel solution methods for poisson-like equations in two-phase flows. Computers & Fluid 80, 152–157.

Wang, T., Wang, J., Jin, Y., 2007. Slurry reactors for gas-to-liquid processes: A review. Industrial and Engineering Chemistry Research 46 (18), 5824–5847.

White, F. M., 1974. Viscous Fluid Flow. McGraw-Hill, Inc.

Yang, G. Q., Du, B., Fan, L.-S., 2007. Bubble formation and dynamics in gas-liquid-solid fluidization. a review. Chemical Engineering Science 62 (1-2), 2–27.

Youngs, D. L., 1982. Numerical Methods for Fluid Dynamics. Academic Press, New York (edited by K.W. Morton and M.J. Bianes), Ch. Time-dependent multi-material flow with large fluid distortion, pp. 273–285.

Yu, Z., Fan, L.-S., 2008. Direct simulation of the buoyant rise of bubbles in infinite liquid using Level Set method. Canadian Journal of Chemical Engineering 86 (3), 267–275.

Yu, Z., Yang, H., Fan, L.-S., 2011. Numerical simulation of bubble interactions using an adaptive Lattice Boltzmann method. Chemical Engineering Science 66 (14), 3441–3451.

Yuan, H., Prosperetti, A., 1994. On the in-line motion of two spherical bubbles in a viscous fluid. Journal of Fluid Mechanics 278, 325–349.

Zhang, Z., Prosperetti, A., 2005. A second-order method for three-dimensional particle simulation. Journal of Computational Physics 210 (1), 292–324.

Zick, A. A., Homsy, G. M., 1982. Stokes flow through periodic arrays of spheres. Journal of Fluid Mechanics 115, 13–26.

Journal papers

I. Roghair, Y. M. Lau, N. G. Deen, H. M. Slagter, M. W. Baltussen, M. Van Sint Annaland, and J. A. M. Kuipers. On the drag force of bubbles in bubble swarms at intermediate and high reynolds numbers. *Chemical Engineering Science*, 66(14):3204–3211, 2011. doi:10.1016/j.ces.2011.02.030.

I. Roghair, M. W. Baltussen, M. Van Sint Annaland, and J. A. M. Kuipers. Direct numerical simulations of the drag force of bi-disperse bubble swarms. *Chemical Engineering Science*, 95:48–53, 2013. doi:10.1016/j.ces.2013.03.027.

M. W. Baltussen, L. J. H. Seelen, J. A. M. Kuipers, and N. G. Deen. Direct numerical simulations of gas-liquid-solid three phase flows. *Chemical Engineering Science*, 100:293–299, 2013. doi:10.1016/j.ces.2013.02.052.

M. W. Baltussen, J. A. M. Kuipers, and N. G. Deen. A critical comparison of surface tension models for the volume of fluid method. *Chemical Engineering Science*, 109:65–74, 2014. doi:10.1016/j.ces.2013.12.045.

M. W. Baltussen, Q. I. E. Segers, J. A. M. Kuipers, and N. G. Deen. Cutting bubbles with a single wire. *Chemical Engineering Science (submitted for review)*, 2015a.

M. W. Baltussen, J. A. M. Kuipers, and N. G. Deen. Cutting bubbles with a wire mesh. *Chemical Engineering Science (submitted for review)*, 2015b.

M. W. Baltussen, J. A. M. Kuipers, and N. G. Deen. A critical comparison between immersed boundary methods. *(In preparation)*, 2015c.

M. W. Baltussen, J. A. M. Kuipers, and N. G. Deen. Direct numerical simulations of the drag force in gas-liquid-solid three phase flows. *(In preparation)*, 2015d.

Conference Proceedings

M. W. Baltussen, J. A. M. Kuipers, and N. G. Deen. Direct numerical simulation of the coalescence of bubbles. In *Proceedings of the 22nd International Symposium on Chemical Reaction and Engineering, Maastricht, The Netherlands*, 2012.

M. W. Baltussen, L.J.H. Seelen, J. A. M. Kuipers, and N. G. Deen. Direct numerical simulation of bubble slurry columns. In *Proceedings of the 9th European Conference of Chemical Engineering, The Hague, The Netherlands*, 2013a.

M. W. Baltussen, L.J.H. Seelen, J. A. M. Kuipers, and N. G. Deen. Direct numerical simulation of gas-liquid-solid three phase flows. In *Proceedings of the 11th International Conference on Gas-Liquid & Gas-Liquid-Solid Reactor Engineering, Seoul, South Korea*, 2013b.

M. W. Baltussen, J. A. M. Kuipers, and N. G. Deen. A critical comparison of surface tension models for volume of fluid method. In *Proceedings of the 10th International Conference on Computational Fluid Dynamics in the Oil & Gas, Metallutgical and Process Industries, Trondheim, Norway*, 2014.

M. W. Baltussen, J. A. M. Kuipers, and N. G. Deen. Cutting bubbles using direct numerical simulation. In *Proceedings of the 12th International Conference on Gas-Liquid & Gas-Liquid-Solid Reactor Engineering, New York, United States of America*, 2015.

Dankwoord

Na vier jaar en een boekje vol met resultaten, ben ik nu misschien wel bij het moeilijkste stuk van mijn promotie aangekomen. Ondanks dat alleen mijn naam op de voorkant van dit proefschrift staat, zijn er veel meer mensen die mij hebben geholpen om dit mooie resultaat neer te zetten. Daarom wil ik nu nog een paar pagina's besteden om al deze mensen te bedanken.

Als eerste wil ik Hans en Niels heel erg bedanken. Hans, dankzij onze lange discussies over de implementatie van de verschillende onderdelen van de methodes, die ontstonden door mijn eigenwijsheid, heb je mij ontzettend geholpen. Daarnaast zijn jouw vakkennis en je kennis over de verschillende methoden een bron van inspiratie voor mij geweest. Niels, als ik weer eens vast zat met coderen of als ik even niet meer wist hoe ik verder moest, dan kon ik altijd een afspraak met je maken om het probleem samen op te lossen. Al was het maken van de afspraak soms al het begin van de oplossing.

Maar ik denk dat ik van jullie beiden misschien nog wel het meeste heb geleerd over mijzelf. Natuurlijk wist ik al wel dat ik perfectionistisch ben, maar nu kan ik soms ook wat pragmatischer naar mijn werk kijken. Ik ben jullie echt dankbaar dat ik met en misschien zelfs door jullie heb mogen leren om nee te zeggen. Al blijf ik nog steeds wel een beetje te vaak ja zeggen.

Vanwege de discussies met Hans en Niels, hadden we soms wat hulp nodig om uiteindelijk een oordeel te vellen over wie er gelijk had. Johan, ik wil je bedanken voor de vele afleidingen die je met me hebt gedaan voor de tweede orde Immersed Boundary methode, want ik vraag me af of ik anders ooit had geloofd dat de versimpelingen in de methode voor constante viscositeit gerechtvaardigd waren. Frank bedankt dat je deur altijd openstond als mijn deeltjes weer rare gedragingen vertoonden.

Ivo, naast dat ik bij jou altijd terecht kon om even over mijn belletjes problemen te kletsen, mocht ik ook gewoon altijd even mijn verhaal houden. Dank je wel voor alle hulp de afgelopen jaren. Martin ten eerste natuurlijk bedankt voor de tijd die je hebt vrijgemaakt om mij in meer detail het oppervlaktespanningsmodel van het Front Tracking model uit te leggen. Ook heb ik altijd met veel plezier met jou en Mariët of Ramon Fysisch Transport Verschijnselen gegeven.

Tijdens mijn project heb ik meerdere studenten begeleidt. Remy, Luuk, Kaoutar, Derek en Martin: allemaal heel erg bedankt voor jullie bijdragen die jullie hebben geleverd aan

mijn werk.

Luuk en Kay heel erg bedankt dat jullie mijn paranimfen willen zijn. Luuk, ik denk dat ik je niet genoeg kan bedanken voor alle discussies die we tijdens en na je afstuderen hebben gehad. Ook wil ik je bedanken voor alle keren dat je me geduldig hebt geholpen met de codes en het paralleliseren. Kay, super bedankt dat je iedere keer wilde luisteren naar mijn problemen in de code, waarop jij meestal de simpelste oplossingen had.

I would like to thank all (previous) SMR members for all the serious discussions and the fun. Because of all the conferences, borrels, SMR outings, the Germany trip and dinners, I felt at ease in the SMR group. Thank you all for the nice working atmosphere. Deepak, Krusnha and Quint, I really enjoyed our discussions on modelling and bubble cutting as project partners. I will never forget our trips to GLS. A special thanks to Ildefonso, Jelle, Kai, Langhui, Lizzy, Marian, Mariët, Martin, Mohammed, Partick, Paul, Ramon, Sebastian, Tom, Vincenzo, Yali and Yuk Man for your technical and less technical discussions.

Although there are not that many experimental results in this thesis, I think I bothered all the technicians with small changes on my set-up. Joost, Joris, Lee and Thijs thanks for all your technical support and muscular strength to lift the set-up. Daarnaast wil ik Ada, Judith en José bedanken voor alle administratieve zaken die jullie altijd voor mij hebben geregeld. Ook wil ik jullie bedanken dat ik eigenlijk altijd even kon binnenlopen om mijn verhaal kwijt te kunnen, of het nu over werk ging of niet.

Ten slotte wil ik graag alle mensen buiten SMR nog even bedanken voor al hun morele steun. Giske, Henk en Martijn, ik kan me zo indenken dat jullie mijn geklets over belletjes na mijn afstuderen vast al zat waren. Daarom misschien nog wel meer bedankt voor alle gezellige etentjes om even mijn zinnen te verzetten en alle berichtjes als het even tegen zat.

Dames 4 van Hajraa super bedankt voor de gezellige jaren die soms wat minder succesvol waren. Daisy, Marleen, Rianne en Tom, ik wil jullie speciaal bedanken voor al jullie steun het afgelopen jaar. Vivian, jou wil ik even in het bijzonder bedanken. Niet alleen was je er voor mij het afgelopen jaar, maar je hebt ook je best gedaan op mijn voorkant. Super bedankt!

Koos en Mark, ik denk dat jullie degenen zijn die mijn entree binnen de Eindhovense Reddingsbrigade zo gemakkelijk hebben gemaakt. Ik hoop dat we nog jaren samen naar Rosmalen kunnen gaan om samen met de jeugdleden deel te nemen aan de EHAD wedstrijden. Mark bedankt dat je er voor mij was als ik even mijn verhaal kwijt moest voordat we beiden les gingen geven. Koos bedankt voor alle keren dat we samen hebben gezeten voor onze opleiding tot instructeur. Daarnaast wil ik alle jeugdleden en kaderleden van de Eindhovense Reddingsbrigade bedanken voor de leuke tijd.

Ellen en Pieter, ik wil jullie bedanken voor al jullie steun en jullie luisterende oor. Ik hoop dat ik de wandelingen niet te saai heb gemaakt met mijn geklets over studenten en belletjes.

Als laatste wil ik mijn familie bedanken voor al hun steun. Sasja, ik denk dat er niemand zoveel heeft toegevoegd in mijn proefschrift terwijl er zo weinig van is overgebleven.

Lisanne, Erik, papa en mama, super bedankt dat ik altijd bij jullie terecht kan voor wijze (zusjes) raad en dat jullie iedere keer weer luisteren naar mijn verhalen over belletjes en deeltjes. Opa en oma, ik denk dat het voor jullie het moeilijkste is om te begrijpen wat ik heb gedaan, maar ik weet ook zeker dat jullie toch jullie best doen om het te begrijpen. Opa, ik wil je bedanken voor alle uren die we samen hebben geknutseld, gesoldeerd en alle wijze raad. Ik denk dat deze uurtjes met z'n tweeën uiteindelijk wel hebben geleid tot dit mooie proefschrift.

Ik heb het gevoel dat ik nog heel veel mensen ben vergeten. Via deze laatste woorden wil ik graag iedereen nogmaals heel erg bedanken voor alle hulp en alle steun.

Bedankt allemaal!

Maike Baltussen
Eindhoven, 2015.

CURRICULUM VITAE

Maike Baltussen werd geboren op 7 september 1987 te 's-Hertogenbosch. Ze groeide op in Rosmalen en Monster, waar ze respectivelijk de bassisscholen den Krommenhoek en Sint Aloysius bezocht. Vervolgens behaalde ze haar VWO diploma aan de Dalton te Den Haag.

Maike startte in 2005 met de bachelor opleiding Chemische Technologie aan de Universiteit Twente. Waarna ze haar opleiding voorzette aan dezelfde universiteit met twee masters in Chemical Engineering en Nanotechnology. In het kader van deze masters heeft ze een stage opdracht voltooid aan de Kyoto Universiteit.

In 2010 studeerde ze af voor de master Chemical Engineering by de vakgroep Fundamentals of Chemical Reaction Engineering aan de Universiteit Twente op een numerieke studie van monodisperse en bidisperse bellenzwermen. Waarna in 2011 ook de opleiding Nanotechnologie werd afgerond met numeriek afstudeeronderzoek naar de colloïdale stabiliteit van oxidatieve nanofilms bij de vakgroep Inorganic Material Science aan de Universiteit Twente.

Na haar opleiding is ze gestart als promovendus bij de vakgroep Multi-Scale Modelling of Multiphase Flows aan de Technische Universiteit Eindhoven. Onder de supervisie van prof.dr.ir. J.A.M. Kuipers and dr.ir N.G. Deen heeft ze onderzoek gedaan naar de opbreking en samenvoeging van bellen door de interactie van bellen met gaasstructuren, waarvan de resultaten zijn beschreven in dit proefschrift.